Time-Frequency localisation of defects using broadband pulsed arrays

Samuel Joseph Hill

THE UNIVERSITY OF
WARWICK

A thesis submitted for the degree of

Doctor of Philosophy in Physics

University of Warwick, Department of Physics

March 2014

Contents

List of Figures

List of Tables

Acknowledgements

Firstly, I would like to thank my supervisor, Professor Steve Dixon, for giving me the opportunity to work on such a great project, and for giving me the support and guidance I needed so that I could finish the PhD. I would also like to thank the rest of my colleagues in the Warwick Ultrasound group. Thanks go to Phil Petcher and Kevin McAughey for all your help and the regular water trips. Francisco Hernandez-Valle is not only the nicest guy in the world, but his help with electronics and coffee time discussions have been invaluable. Thanks also to Charley Fan for teaching me plenty of EMAT hints, and for not (seriously) injuring me at badminton. Hashimi Rosli, Tobias Eriksson and Michael Laws all get honourable mention for sharing regular coffee breaks with me and making me laugh at various stages of my PhD. Thanks to everyone else I have failed to name - there are just too many people to mention! And yes, Andy, I have finished my thesis now.

I also want to express my deepest gratitude to both my parents for all their support and encouragement - I wouldn't be where I am without you, Mum and Dad. Thanks also to my sister, Rebecca, and the rest of the family for attempting to keep me sane. Eternal thanks goes to Elodie Duché for all of her love, support and help; without it, there is no way I would have been able to finish.

Lastly, I would like to acknowledge the funding provided by the Research Centre of Nondestructive Evaluation (RCNDE) which made this work possible.

Declaration

I declare that the work presented in this thesis is my own except where stated otherwise, and was carried out entirely at the University of Warwick during the period between October 2010 and March 2014, under the supervision of Prof. Steve Dixon. The research reported here has not been submitted, either wholly or in part, in this or any other academic institution, for admission to a higher degree. Parts of this work, and other work not reported in this thesis, have appeared in other forms, listed here.

Peer-reviewed journal articles:

- S. J. Hill and S. Dixon, "Localisation of defects with time and frequency measurements using pulsed arrays", *NDT & E International*, vol. 67, pp. 24 - 30, October 2014.
- S. J. Hill and S. Dixon, "Frequency dependent directivity of periodic permanent magnet electromagnetic acoustic transducers", *NDT & E International*, vol. 62, pp. 137 - 143, March 2014.
- S. Dixon, S. J. Hill, Y. Fan and G. Rowlands, "The wave-field from an array of periodic emitters driven simultaneously by a broadband pulse", *Journal of the Acoustical Society of America*, vol. 133, no. 6, pp. 3692 - 3699, June 2013.

Conference proceedings:

- S. J. Hill and S. Dixon, "Using a Pulsed Array to determine the position of a defect", in *AIP Conference Proceedings*, vol. 1581, Baltimore (Maryland),

USA: AIP, 2014, pp 80 - 87.

- S. B. Palmer, S. J. Hill, G. Rowlands and S. Dixon, "An ultrasonic wavefront with propagation direction dependent frequency", in *Proc. SPIE, Nondestructive Characterization for Composite Materials, Aerospace Engineering, Civil Infrastructure, and Homeland Security,* vol. 8694, San Diego (CA), USA: SPIE, 2013, pp. 86941S.

- S. J. Hill and S. Dixon, "Pulsed arrays: a new method of flaw detection by generation a frequency dependent angle of propagation," in *AIP Conference Proceedings*, vol. 1430, Burlington (Vermont), USA: AIP, 2012, pp. 913 - 920.

- S. J. Hill and S. Dixon, "Wavefronts with angular dependent frequencies from pulsed arrays," in *Proceedings of the National Seminar & Exhibition on Non-Destructive Evaluation*, Chennai, India: ISNT, 2011, pp. 21 - 24.

Presentations at national and international conferences:

- S. J. Hill and S. Dixon, "Using pulsed array frequency measurements to locate defects", presented at the *52th Annual British Conference on Non-Destructive Testing (NDT 2013)*, Telford, UK, Sept. 2013. Talk.

- S. J. Hill and S. Dixon, "Using a Pulsed Array to determine the position of a defect", presented at the *Annual Review of Progress in Quantitative Nondestructive Evaluation (QNDE 2013)*, Baltimore (Maryland), USA, July 2013. Talk.

- S. J. Hill and S. Dixon, "Using a Pulsed Array to determine the position of a defect", presented at the *51th Annual British Conference on Non-Destructive Testing (NDT 2012)*, Daventry, UK, Sept. 2012. Talk.

- S. J. Hill and S. Dixon, "Wavefronts with angular dependent frequencies from pulsed arrays", presented at the *Indian National Seminar & Exhibition on Non-Destructive Testing (NDE2011)*, Chennai, India, Dec. 2011. Talk.

- S. J. Hill and S. Dixon, "Using pulsed array frequency measurements to locate defects", presented at the *50th Annual British Conference on Non-Destructive Testing (NDT 2011)*, Telford, UK, Sept. 2011. Talk.

- S. J. Hill and S. Dixon, "Pulsed arrays: a new method of flaw detection by generation a frequency dependent angle of propagation", presented at the *38th Annual Review of Progress in Quantitative Nondestructive Evaluation (QNDE 2011)*, Burlington (Vermont), USA, July 2011. Talk.

Abstract

The spatial periodicity of an array of emitters with an alternating polarity structure is utilised to generate a wavefront with a range of interesting properties. This wavefront is generated by simultaneously exciting the elements with a pulse with carefully selected broadband characteristics. The creation of these waves leads to a broadband interference effect that causes the wavefront to cover a large range of solid angles. More interestingly, however, is the continuous variation of the frequency of the wavefront as a function of angle.

Whilst this pulsed array system demonstrates many interesting phenomena, it can also be applied to practical scenarios within the field of non-destructive testing. As the generated wavefront propagates through the sample, it will be scattered by discontinuities that may be present in the sample. This scattered wave will have a unique time of flight and frequency, and this information can be used to locate the position of defects. Due to the frequency variation of the wavefront, the angular position of the defect can be calculated from the frequency of the scattered wave. The radial position of the scatterer can be estimated using the time of flight of the wave.

This approach has some advantages over the phased array techniques, which are currently utilised within the field of ultrasonic inspection. Whilst phased array techniques are versatile and can control the generated ultrasonic beam, they require complicated electronics and beam-forming algorithms to achieve this. This requirement is avoided with the pulsed array, as all of the array elements are activated simultaneously. Also, as the time-frequency characteristics of the scattered wave maps directly to the polar co-ordinates, only a single measurement is needed to locate a defect. This is in contrast to other ultrasonic methods that only utilise the time of flight information of the scattered wave, and hence multiple measurements are needed to localise a defect.

Abbreviations

AC	Alternating Current
DC	Direct Current
DFT	Discrete Fourier Transform
EMAT	ElectroMagnetic Acoustic Transducer
FEA	Finite Element Analysis
FEM	Finite Element Method
FFT	Fast Fourier Transform
FT	Fourier Transform
IDFT	Inverse Discrete Fourier Transform
IFFT	Inverse Fast Fourier Transform
IFT	Inverse Fourier Transform
PPM	Periodic Permanent Magnet
NDE	Non-Destructive Examination
NDT	Non-Destructive Testing
SAW	Surface Acoustic Wave
SH	Shear Horizontal
SNR	Signal-to-Noise Ratio
SV	Shear Vertical

Chapter 1

Introduction

1.1 Research Motivation

The aim of this thesis is to investigate a novel method of utilising an array of ultrasonic sources, whereby they are pulsed simultaneously with an excitation signal which has carefully controlled frequency characteristics. It was found that the wavefront generated by this method has an interesting feature of having a variation in the frequency of the wavefront as a function of propagation angle. Numerous modelling approaches are undertaken in order to explain the physical principles that lead to the creation of such a wavefront, and which allow for its characteristics to be ascertained. For instance, it was found that the wavefront is fundamentally an interference effect, being generated due to the interaction between the waves from the individual elements of the array. From these models, and supported by experimental measurements, a quantitative relationship between the angle of propagation and the frequency of the wavefront was found.

As the frequency variation is smooth and continuous over a large range of angles, this pulsed array method can be used as a form of ultrasonic inspection, and can locate a discontinuity that scatters a wave. This can be achieved, by investigating the time of flight and frequency of the wave, with a single measurement. The time of

flight value indicates the radial distance of the defect, whilst the peak frequency of the wave can be related to the angular position of the defect. This is in contrast to traditional ultrasonic measurements, which only use the time of flight information of a scattered wave and can subsequently only locate the scatterer upon an ellipse. This pulsed approach also has the advantage of having a simplified mode of operation; the simultaneous activation of the elements within the array eliminates the requirement for complicated and expensive electronics and software to control the firing of the array elements. Conversely, due to the increased number of elements that are being used in arrays, the complexity of operation of phased arrays is increasing [1–3]. The ideas in this thesis present a totally unique way of using an array of emitters to ultrasonically inspect a sample for defects, whilst reducing the complexity of the system.

1.2 Non-Destructive Testing

Non-destructive testing, or NDT, describes a broad range of techniques that can be used to assess the state of a structure without causing any damage to it [4–6]. In an industrial context, as NDT does not permanently alter the condition of a component, this can lead to the extension of its useful life without the risk of failure of the component whilst in service. Whilst in this thesis, NDT will generally be used to refer the detection, localisation and sizing of a defect or flaw, the term can be applied to a much wider context. For example, methods of measuring the thickness [7, 8] or material composition of a sample [9, 10] can all be classified as non-destructive testing. There is a range of complimentary techniques that be used in NDT, with each method having their unique benefits and limitations. In order to give an overview of the field, some of the more established techniques are described in the following sections.

1.2.1 Visual Methods

Visual inspection is probably the oldest and most widely applied form of NDT, mainly as a consequence of simplicity of implementing the inspection [4, 11]. Direct visual inspection can be used to check for large and obvious surface abnormalities, although even these can be obscured if the sample surface is not appropriately prepared [4]. The resolution and sensitivity of such an inspection is limited by the eye, although optical aids, such as microscopes, can be used to improve these [6]. Other visual aids, such as borescope or endoscopes, can be used to inspect internal or inaccessible surfaces [6]. This can be particularly useful for the inspection of turbine blades, power plants or other machinery, which allows for imaging of a system without the need to remove any external cladding [6].

Despite the use of visual aids, the success of using visual methods of inspection greatly depends upon the operator. Even with thorough and specific training, it is difficult to get repeatable results between inspectors. Also, unless the results are properly recorded, fatigue can lead to variable results and the chance that important indications are missed. However, visual inspection can be very useful as a pre-screening method; being used to inform a more specialist inspection, either in terms of method or location to concentrate the inspection efforts [4].

1.2.2 Magnetic Flux Leakage Method

Another method that is sensitive to surface, or near-surface, defects is the magnetic flux leakage method. The method involves magnetising a ferromagnetic sample, with either a permanent magnet, electromagnet or electrical current. In a perfectly homogeneous sample, the magnetic field will be uniform along the sample. However, non-magnetic flaws, such as cracks or inclusions, will lead to perturbations in the magnetic field, as shown in figure 1.1.

A magnetic sensor, such as an inductive coil, Hall effect probe or GMR sensor, can detect these disturbances in the magnetic field and hence the flaw that is causing

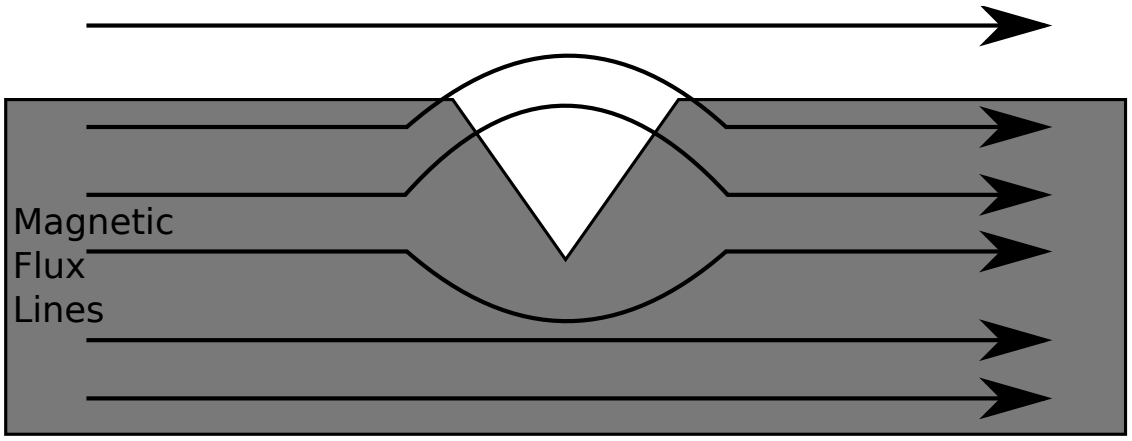

Figure 1.1: A non-magnetic inhomogeneity will perturb the magnetic field. Therefore, the presence of a near-surface flaw can be found by measuring the magnetic field close to the sample.

it [12]. In some instances, the shape of the signal can be used to characterise the defect, in terms of its size, shape and orientation [13–16]. With magnetic flux leakage techniques, no direct contact with the sample is required, and there can be automated for high speed inspection. However, the method is, of course, limited to use on ferromagnetic and magnetically permeable materials, and can only detect near-surface irregularities [4, 16]. In addition, narrow cracks that are orientated along the direction of the magnetic field do not significantly perturb the magnetic field, and are hence difficult to detect [5].

1.2.3 Eddy Current Testing

Eddy current testing is another surface, or near-surface, measurement approach that can be used on any electrically conducting sample. In conventional eddy current testing, a wire carrying an alternating electric current is held near to the test sample, which generates an alternating magnetic field [16]. This varying magnetic field induces eddy currents within the skin depth of the material, which, in turn, produce their own magnetic field that opposes the incident magnetic field. The presence of this secondary magnetic field is observed through changes in the impedance in either the original coil, or a second detector coil [11]. Defects in the material surface will

act to alter the phase and amplitude of the measured impedance, thereby providing a measure of their position and size.

Whilst being able to detect small defects on the surface of an electrical sample, eddy current testing is only able to inspect the sample to a limited distance from the surface, which is termed the electromagnetic skin depth. Whilst the skin depth is discussed in more detail in Section 2.2.1, it is important to remember that the skin depth is inversely proportional to the frequency of the eddy current [17]. Hence, for a chosen, single frequency eddy current test, the depth of inspection is fixed. This also means that, whilst the surface size of the flaw can be accurately found, no depth sizing can be performed. However, instead of using a continuous single frequency signal for eddy current testing, a pulsed approach can be used [18]. The pulsed approach allows for an inspection with a range of frequencies to be performed simultaneously, meaning the high surface resolution is retained, whilst the low frequency components of the signal will penetrate further into the sample, allowing for defects to be detected at greater distances from the surface [18].

As the measured impedance of the coil will also be dependent upon surface condition of the sample and the lift-off distance, care must be taken to uncouple changes these parameters from changes in impedance caused by the presence of flaws or defects. Also, whilst high resolution scanning can be achieved using eddy current testing, it would be very time consuming to achieve this with a single coil. Hence, arrays of eddy current elements can be used to achieve greater coverage thus allowing larger areas to be scanned in one sweep, which will increase the range of inspection [19].

1.2.4 Thermography

Whilst there is a number of variants of thermal testing, the underlying feature is that they measure the diffusion of heat through a sample. This sample can either be passively or actively heated, and the resultant heat distribution is studied using

an infra-red imaging system. In a popular system, called flash thermography, the sample surface is flooded with heat from a flash bulb, and the rate at which heat flows into the body of the sample is inspected using an infra-red camera [20]. Any subsurface defects or delaminations will show up as hot spots where the heat flow into the body is impeded by the presence of a defect, and the time taken for the hot spot to appear can indicate the depth of the defect [4, 20, 21].

Whilst this is generally considered a non-contact method, it may sometimes be necessary to apply a dark coating to samples so that the heat is absorbed, rather than reflected away [22]. As this method is measuring variations in thermal resistance, it may be difficult to detect closed defects as they provide little impedance to the heat flow [23]. Due to the thermal relaxation times, thermography measurements can take a long time, when compared to eddy current measurements; however, to balance this out, a single thermographic measurement can cover a large area of the surface.

1.2.5 Radiography and Tomography

Radiography is an effective method of non-destructively detecting flaws throughout the volume of sample. The method utilises penetrating radiation to form a transmission image of the radiation intensity after it has passed through a sample. As the radiation is attenuated differently as it passes through individual materials, the intensity distribution can be used to infer the presence and location of defects and flaws [4]. Several forms of radiography exist; electromagnetic radiography, which use either X-rays or gamma rays, is the most common form, with neutron radiography also existing. Whilst the physics of X-rays and gamma rays are very similar, the methods of generation differ greatly. X-rays are generated by accelerating high-energy electrons into a metallic target, which is usually tungsten embedded in copper [16], whilst gamma rays are created from the nuclear decay of unstable isotopes.

As well as producing a simple, 2D 'shadow' image, three dimensional imaging is also possible through the application of computerised tomography (CT), which takes a large number of radiographic scans with the sample rotated relative to the scan axis [11, 24]. X-Ray CT is considered as the 'gold standard' is many areas of NDT, due to the superior resolution that can be achieved using X-Ray CT systems [24]. In addition to the improved resolution, it is also possible to obtain a full three dimensional volumetric image of the sample. However, such CT systems are expensive and exacerbate the safety concerns associated with radiography due to the large number of scans that are required to formulate a tomographic image. Whilst radiography can be used to inspect a wide range of material thickness, from thin metallic foils to samples in the meter-size range, the method relies on having access to both sides of the sample, which may not be practical in some situations [16]. In order to have sufficient contrast between a defective region and the background medium, the flaw must be orientated parallel with the interrogating beam. Furthermore, all forms of radiography can be expensive and have safety concerns, due to the expense of obtaining and maintaining these sources of radiation, and the health effects they may have on the NDT operators.

1.2.6 Ultrasonics

Ultrasonic inspection utilises the propagation of mechanical vibrations with a frequency above 20 kHz in order to probe a material. By measuring the time of flight or attenuation of ultrasonic waves, information about the material can be determined. For example, the presence, position, size, and shape of a flaw can be ascertained, as well as other information such as the material density, composition and geometry [25, 26]. Depending upon the types of ultrasonic waves used, the inspection can be focused on the surface of a material, or through its bulk. As this thesis is concerned with an ultrasonic approach to NDT, a more complete description, along with some advanced ultrasonic methods, is given in Chapter 2.

Any material that is capable of supporting ultrasonic waves can be inspected in this way. This is in contrast with other NDT methods, such as eddy current testing, can only be used on specific samples. Also, unlike radiography, only a single side of the sample is required for an inspection. Indeed, using guided waves, inaccessible regions can be inspected by generating the waves in a more hospitable region and allowing a structure to guide the energy to the region of interest. Ultrasonic inspection can also be a non-contact method, if appropriate transducers are used, as discussed in Section 2.2.

1.3 Thesis Outline

Firstly, in Chapter 2, the research presented in this thesis is contextualised within the field of ultrasonic inspection and the associated research directions are considered. Relevant ultrasonic theory is presented in this chapter, showing how a wave can propagate in an elastic medium due to the internal restoring forces of the medium acting against any initial disturbance. The various polarisations of the ultrasonic waves are also discussed, with expressions for their different wave speeds derived in terms of material properties. Ultrasonic surface and guided waves, that are constrained by a particular sample geometry, are also examined. In particular, the characteristics and benefits of shear horizontal waves, which are used in this work, are explored. For ultrasonic testing to be viable, there must be reliable ways to generated and detect the disturbances using ultrasonic transducers. Particular attention is given to electromagnetic acoustic transducers (EMATs), as they were extensively used in this work. Finally, these ideas are brought together in order to show numerous methods of non-destructive testing, and how the propagating wave can be used to probe samples without causing damage. More advanced techniques, such as phased array techniques, can be used to improve the sensitivity and resolutions of measurements, although they have the effect of increasing the complexity

of the inspection.

Chapter 3 explores how the spatial periodicity of an ultrasonic array can result a frequency dependent directivity. This directivity applies when the elements of the array are excited simultaneously, removing the necessity for complicated and expensive phased array hardware. As a consequence of the frequency dependence of the directivity, the wavefront that is generated by such an array can be controlled and steered by simply varying the frequency of the generation signal. A frequency domain model is constructed, which can be used to calculate the directivity of arrays, including the width as well as the peak position of the beam, that are being driven by a particular input signal.

Chapter 4 introduces the main theme of the thesis; that of pulsed arrays. Pulsed arrays utilise the same spatial periodicity as frequency steered arrays, but over a broadband frequency range. The generated wavefront from these broadband pulsed arrays extends over a large solid angle, and has a variation in frequency with propagation direction. Semi-analytic Huygens techniques are used to model the wavefront generated by a pulsed array, in order to determine the underlying physical processes that create the wavefront. The periodic array acts in a similar fashion to a diffraction grating, with the wavefront created due to the interference of the waves from each of the elements that make up the array, with the frequency of the wavefront varying as expected from the diffraction grating equation.

This proposed model is further supported by finite element simulations, that are shown in Chapter 5. The finite element simulations aim to model the array, and the wavefield it produces, more completely. For example, finite element simulations can be used to model the effects of having elements of finite size, as well as simulate the interactions of the wavefront with discontinuities. The frequency variation predicted by the finite element model is consistent with the semi-analytic model described in Chapter 4.

The wavefront was experimentally realised using an ultrasonic EMAT array,

which is detailed in Chapter 6. Both the narrowband and broadband directivity of the array are measured, showing how the wavefront can be controlled even with simultaneous activation of all of the elements. The construction of the relevant ultrasonic transducers is described, as are the various modes of excitation and data processing that are required in order to utilise the arrays. The frequency variation of the pulsed array wavefront of the transducer measured here are in good agreement with both the analytic and FE model.

The pulsed array wavefront demonstrates many interesting physical phenomena, but it can also be applied for practical, NDT purposes. If a defect is present in a sample, it will scatter a particular portion of the generated wavefront. The frequency of this scattered wave will depend on the angular position of the defect relative to the centre of the array, whilst the time of flight measurements indicate the radial distance of the defect. This principle is tested in Chapter 7, with defects located with a single measurement, by utilising the combined time and frequency characteristics of the scattered waves. Finally, the conclusions and main findings that have arisen from this work are presented in Chapter 8, along with further suggested research directions that could build upon the research within this thesis.

Chapter 2

Ultrasonic Inspection

A popular branch of non-destructive testing relies on the use of a propagating ultrasonic wave to interrogate a sample. The propagation characteristics of an ultrasonic wave can elucidate many fundamental properties of the medium through which the wave is travelling. It is important to discuss the theoretical details of how ultrasound propagates, and how this propagation is related to the material properties, as well as how the waves interact with interfaces, and how they are scattered by defects. This is covered in section 2.1. In addition to discussing how ultrasound propagates, methods of generating and detecting these mechanical vibrations are described, along with the physical principles behind their operation, in section 2.2. The use of ultrasonic waves within non-destructive testing is contextualised in section 2.3. The section briefly discusses the basic principles of ultrasonic inspection, before considering more advanced techniques that arise from the use of ultrasonic arrays. These techniques, such as the ability to steer or focus an ultrasonic beam, originate from the capacity to control each element in the array independently.

2.1 Ultrasonic Wave Propagation

Ultrasound is defined as an acoustic oscillation that has a frequency that is above the level of human hearing, in excess of 20 kHz, and can exist in solid, liquid and gaseous

media. In elastic solids, which are considered here, there are a number of different wave modes that can be supported, each with different particle polarisations and velocities [27–29]. The oscillatory motion of the ultrasound is caused by an initial disturbance that causes the particles to leave their equilibrium position. The particle displacement away from this initial position gives rise to internal restoring forces, which attempt to return the particle to its equilibrium position [25, 26, 30, 31]. This oscillation acts to deform the medium, with the deformation causing the disturbance to be transmitted throughout the material, transferring both kinetic and potential energy as it propagates.

Due to the inertia of the medium, the disturbance propagates at a finite speed rather than acting on the whole medium simultaneously [28]. In order to continue propagating, the deformation must overcome the resistance offered to it by the internal structure of the material, in addition to the inherent inertia of the atoms. The amount of deformation and the inertia of the medium are fundamental properties that describe how the mechanical wave will propagate.

2.1.1 Behaviour of elastic materials

By understanding how the medium responds to an initial impulse, the propagation of the wave through the material can be fully explained. In the case of a solid that is still within the linear elastic regime [27, 29], the relationship between the deformation and internal restoration forces of the sample is given by the stress (σ) and strain (ϵ) within the material. Expressed in Cartesian co-ordinates, the stress and strain are given by:

$$\sigma_{ij} = \begin{pmatrix} \sigma_{xx} & \sigma_{xy} & \sigma_{xz} \\ \sigma_{yx} & \sigma_{yy} & \sigma_{yz} \\ \sigma_{zx} & \sigma_{zy} & \sigma_{zz} \end{pmatrix}, \tag{2.1}$$

$$\epsilon_{ij} = \begin{pmatrix} \epsilon_{xx} & \epsilon_{xy} & \epsilon_{xz} \\ \epsilon_{yx} & \epsilon_{yy} & \epsilon_{yz} \\ \epsilon_{zx} & \epsilon_{zy} & \epsilon_{zz} \end{pmatrix}. \tag{2.2}$$

Tensors for stress and strain are required due to the three dimensional nature of the problem. The stress component $\sigma_{xx} = \frac{F_x}{A_x}$ describes how a force, F_x, is applied in the $x-$direction, over an area A_x onto the yz plane. The strain tensor describes how the material reacts to a given applied force. In general, for a linearly elastic solid, the relationship between the stress and strain is [28, 29, 32]:

$$\sigma_{ij} = C_{ijkl}\epsilon_{kl}. \tag{2.3}$$

Here, Einstein notation is used to indicate a summation over repeated indices [33], with the subscript indices i, j, k, l representing any of the three spatial directions, x, y, z. C_{ijkl} is the fourth-order stiffness tensor that acts as the linear proportionality constant that is expected from Hooke's Law. Each component C_{ijkl} represents a property of the material [29]. While the Stiffness tensor can have 81 components, there is a maximum of 36 independent constants that are allowed [29]. Certain symmetry considerations and approximations can reduce this further to two independent variables [26, 28, 29]. If homogeneity and isotropy of the material are imposed, then the stiffness tensor becomes:

$$c_{ij} = \begin{pmatrix} c_{11} & c_{12} & c_{12} & 0 & 0 & 0 \\ c_{12} & c_{11} & c_{12} & 0 & 0 & 0 \\ c_{12} & c_{12} & c_{11} & 0 & 0 & 0 \\ 0 & 0 & 0 & c_{44} & 0 & 0 \\ 0 & 0 & 0 & 0 & c_{44} & 0 \\ 0 & 0 & 0 & 0 & 0 & c_{44} \end{pmatrix}, \tag{2.4}$$

where $c_{12} = \lambda$ and $c_{44} = \mu$ called the Lamé constants, and c_{11} can be expressed

as a linear combination of the Lamé constants:

$$c_{11} = \lambda + 2\mu. \tag{2.5}$$

These elastic moduli are dependent on the material micro-structure, such as grain size, and can vary with environmental factors such as temperature and applied load [25].

2.1.2 Waves in Elastic Media

By considering the equations of motion of the material, as well as Hooke's law given in equation 2.3, the polarisation and characteristic wave speeds can be found. For a small region of a material with density, ρ, Newton's second law becomes [26]:

$$\sigma_{ij,j} = \rho \ddot{u}_i, \tag{2.6}$$

where u_i represents the i^{th} component of the particle displacement, and $\ddot{u}_i$ is the second temporal derivative of this displacement. From the assumption of isotropy, equation 2.3 can be reduced to the following [26, 34]:

$$\begin{aligned} \sigma_{ij} &= \left(c_{11} - 2c_{44}\right) \delta_{ij} \epsilon_{k,k} + 2c_{44} \epsilon_{ij} \\ &= \left(c_{11} - 2c_{44}\right) \delta_{ij} \epsilon_{k,k} + c_{44} \left(u_{i,j} + u_{j,i}\right), \end{aligned} \tag{2.7}$$

where the equation is now expressed in terms of material constants c_{11} and c_{44}, and δ_{ij} is the Kronecker delta [33]. Now, by substituting equation 2.7 into equation 2.6, the equation of motion, the wave equation, for waves in a three dimensional isotropic medium is found to be:

$$\left(c_{11} - 2c_{44}\right) u_{j,ij} + c_{44} \left(u_{i,jj} + u_{j,ij}\right) = \rho \ddot{u}_i. \tag{2.8}$$

Using vector notation, applying the gradient $\left(\nabla = \left(\frac{\partial}{\partial x_i}, \frac{\partial}{\partial x_j}, \frac{\partial}{\partial x_k}\right)\right)$ and Laplacian

$\left(\nabla^2 = \left(\frac{\partial^2}{\partial x_i^2} + \frac{\partial^2}{\partial x_j^2} + \frac{\partial^2}{\partial x_k^2}\right)\right)$ operators, the expression can be simplified to give [25–29]:

$$(c_{11} - c_{44})\,\nabla\,(\nabla \cdot \mathbf{u}) + c_{44}\nabla^2\mathbf{u} = \rho\frac{\partial^2\mathbf{u}}{\partial t^2}. \tag{2.9}$$

Now, the displacement field is shown as a vector, with components $\mathbf{u} = (u_i, u_j, u_k)$. As the displacement is a vector field, it can be written as a sum of a gradient of a scalar potential, ϕ, and the curl of a vector potential, $\boldsymbol{\psi}$ [26, 27, 29]:

$$\mathbf{u} = \nabla\phi + \nabla \times \boldsymbol{\psi}. \tag{2.10}$$

Using this expression for the vector displacement field, the wave equation 2.9 can separated into two independent variables; a wholly scalar term and a wholly vector term:

$$\nabla\left(\rho\frac{\partial^2\phi}{\partial t^2} - c_{11}\nabla^2\phi\right) + \nabla \times \left(\rho\frac{\partial^2\boldsymbol{\psi}}{\partial t^2} - c_{44}\nabla^2\boldsymbol{\psi}\right) = 0. \tag{2.11}$$

For this condition to always be satisfied, both the scalar and vector part of the equation must be independently zero [27]:

$$\rho\frac{\partial^2\phi}{\partial t^2} = c_{11}\nabla^2\phi, \tag{2.12}$$

$$\rho\frac{\partial^2\boldsymbol{\psi}}{\partial t^2} = c_{44}\nabla^2\boldsymbol{\psi}. \tag{2.13}$$

2.1.2.1 Longitudinal and Shear Waves

From equations 2.12 and 2.13, it can be seen that two forms of wave can be supported in an isotropic bulk medium; longitudinal waves described by equation 2.12, and shear waves described by equation 2.13. From equation 2.10, it can be seen that

longitudinal waves have particle displacement polarised in the direction of propagation of the waves, whilst the particle displacement of shear waves is perpendicular to the propagation direction [27,34]. In a three-dimensional material, there are two possible orthogonal directions for the shear polarisation, which are typically defined as shear horizontal (SH) and shear vertical (SV). The phase velocities of these waves can be obtained from the independent wave equations, and are found to be:

$$v_L = \sqrt{\frac{c_{11}}{\rho}} = \sqrt{\frac{\lambda + 2\mu}{\rho}}, \tag{2.14}$$

$$v_s = \sqrt{\frac{c_{44}}{\rho}} = \sqrt{\frac{\mu}{\rho}}. \tag{2.15}$$

As the medium is isotropic, the two differently polarised shear waves propagate with the same velocity, although they will behave differently at interfaces [28,35].

2.1.2.2 Ultrasonic Waves at Interfaces

The ultrasonic wave will propagate undisturbed through a medium, unless the properties of the medium properties change. A material can be acoustically characterised by its acoustic impedance [11]:

$$z = \rho v. \tag{2.16}$$

The acoustic impedance can be used to determine how waves will behave at an interface between two media of differing acoustic impedances. At this interface, a number of things can happen, such as refraction, reflection and mode conversion [26–29,32]. For an acoustic wave travelling through a material of acoustic impedance, z_1, which is normally incident on a boundary with a material of acoustic impedance, z_2, then the pressure transmission, T_P, and reflection, R_P, are given by [26]:

$$T_P = \frac{2z_2}{z_1 + z_2}, \tag{2.17}$$

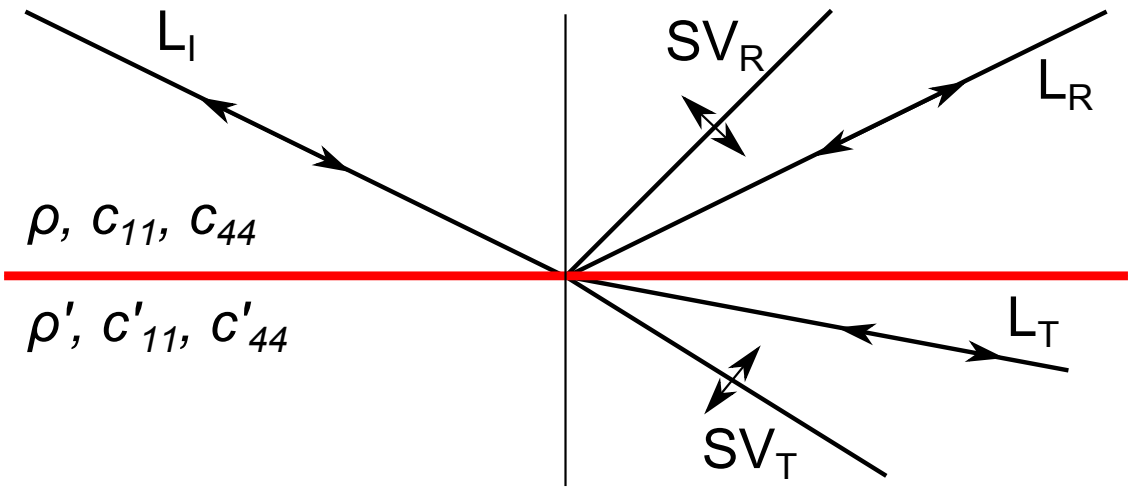

Figure 2.1: A longitudinal (L) wave at an interface between two media, undergoing reflection, refraction and mode conversion into shear vertical waves (SV).

$$R_P = \frac{z_2 - z_1}{z_1 + z_2}. \tag{2.18}$$

From these definitions, if the acoustic impedance of the second medium is less than the first, then $R_P < 0$ and the reflected wave will always be subject to a phase change of π radians. In the limit that $z_2 \ll z_1$, then the boundary is effectively free, and all of the ultrasonic energy is reflected [26, 32].

As well as the transmission and reflection of ultrasound at an interface, mode conversion - when one polarisation of wave converts, partially or wholly, into another polarisation - can also occur. In an infinite isotropic medium, the different wave modes are uncoupled, as shown in equations 2.12 and 2.13. However, at a boundary between two media, the waves can become coupled through the boundary conditions being satisfied [29]. Hence, instead of having a single transmitted and reflected mode, these waves can be split into two modes. For example, an incident longitudinal wave can partially mode convert into transmitted and reflected SV waves, as well as the expected longitudinal transmitted and reflected waves, as shown in figure 2.1. The partitioning of amplitude between longitudinal and SV waves varies as both a function of angles (both incident and reflection) and of Poisson's ratio, ν [25, 27, 34, 36].

As SH waves are polarised such that their displacement is orientated parallel to the material boundary, they cannot couple to the other wave modes. As a consequence, SH bulk waves do not mode convert at a boundary between two media. At a free boundary (a metal-air interface can be considered as such [25]), SH waves are reflected without a loss of amplitude [25, 28, 37, 38]. This makes SH waves particularly useful for ultrasonic inspection as there it is necessary only to consider SH waves, reducing the complexity of the obtained ultrasonic data [37].

2.1.2.3 Attenuation of Bulk Waves

Ultrasonic bulk waves do not propagate indefinitely, and the energy associated with the wave attenuates as it propagates. This attenuation can be characterised as belonging to one of two groups; either geometric attenuation or intrinsic attenuation [4]. Geometric attenuation arises as the energy geometrically spreads out from the source, thereby reducing the intensity of the wave [39]. Intrinsic attenuation is caused by scattering or absorption of the ultrasonic energy by the medium [25, 26]. It is important to know the level of attenuation in a material, as excessive attenuation will lead to reduced sensitivity and restricted penetration depth.

Estimations of geometric attenuation usually assume an omnidirectional source of acoustic energy, with the ultrasonic wave spreading out from a point. As this energy is travelling out equally in all directions, it is being spread over the surface of sphere with an increasingly expanding radius. Hence, the energy per unit area, and therefore measured signal intensity, follows the expected inverse square law, $I \propto 1/R^2$, where R is the propagation distance. A three-dimensional omnidirectional source clearly leads to the greatest geometric attenuation, but it can be much less in other cases. By using a similar argument to the omnidirectional source, the geometric attenuation associated with a line source or a wave constrained to two dimensions can be calculated. In this case, the ultrasonic energy is distributed evenly over the circumference of a circle, meaning that the signal intensity is proportional to $1/R$.

Also, for a steered ultrasonic beam, the geometric attenuation will be dominated by diffraction losses [11, 16, 25, 28].

Intrinsic attenuation occurs in non-ideal materials, arising through a range of mechanisms, such as scattering and absorption [11, 25, 29]. Scattering occurs from the small grains of material with random crystallographic orientation that form the macroscopically homogeneous material [16, 40]. These grains have subtly different acoustic impedances along the direction of propagation, meaning that ultrasound is weakly scattered at the grain boundaries. Due to the multitude of causes of attenuation, it is usually treated by a phenomenological approach, with all of the entities combined into a single attenuation coefficient, α. The fractional loss of energy, $\mathrm{d}E$, per unit path length, $\mathrm{d}x$, is assumed to be constant, which leads to [25]:

$$\frac{\mathrm{d}E}{E} = \frac{\mathrm{d}I}{I} = -2\alpha \mathrm{d}x, \tag{2.19}$$

where I represents the intensity, which is proportional to the energy E. If I_0 and A_0 are the initial intensity and amplitude at $x = 0$, then the intensity and amplitude become [25, 32]:

$$I\left(x\right) = I_0 e^{-2\alpha x}, \tag{2.20}$$

$$A\left(x\right) = A_0 e^{-\alpha x}. \tag{2.21}$$

This attenuation coefficient is generally frequency dependent, with higher frequency waves being more attenuated than lower frequency waves, due to the relative size of the wavelength in relation to the average grain size [26, 28, 41]. The frequency dependence not only leads to the reduction in the signal amplitude, but can result distortion of the wave pulse [16,29]. Whilst the exact relationship between frequency and attenuation may be difficult to formulate, the attenuation can be split into various regimes, which will depend on an average scatter size, D, relative to the

wavelength of the ultrasound, λ. For the work performed here, the wavelength will tend to be much larger than the average grain size, which tends to be of the order of 100 μm [26, 42, 43]. In this case, Rayleigh scattering is dominant, with the attenuation factor being strongly dependent on both the frequency and the average grain size [26, 35]. In the intermediate stochastic regime, where $\lambda \approx D$, the frequency dependence is less pronounced than in the Rayleigh regime. Finally, if the wavelength is much smaller than the typical grain size, the scattering is termed diffuse, and only depends on the size of the grain [41, 42, 44]. The approximate dependence on frequency and grain size is given in equation 2.22.

The effect of absorption can also be considered in the attenuation coefficient. Absorption is the conversion of the mechanical energy of the wave into heat, which can occur in numerous ways, including thermoelastic effects [26, 28]. Thermoelastic damping is caused by the thermal gradient that occurs between the parts of the medium that are in compression and those that are expanding [45]. Thermoelastic damping is only present for longitudinal waves, as shear waves do not produce changes in volume [29]. The attenuation coefficient can then be split into the following [26, 41, 42, 44]:

$$\begin{array}{rcl} \text{Absorption}: & & \alpha_a \propto \omega \\ \text{Rayleigh}: & \lambda \gg D & \alpha_R \propto D^3\omega^4 \\ \text{Stochastic}: & \lambda \approx D & \alpha_S \propto D\omega^2 \\ \text{Diffuse}: & \lambda \ll D & \alpha_d \propto {}^1\!/_D \end{array} . \tag{2.22}$$

Here, $\omega = 2\pi f$ represents the angular frequency of the wave, and f is the ordinary frequency. The constants of proportionality for these relations are material dependent and determine the level of attenuation in the media. Due to the broad distribution of grain sizes, attenuation may not be dominated by a single term in equation 2.22 and hence may not directly correspond to a power given in those equations [29, 41, 44]. The attenuation proportionality coefficients can be reduced

by heat-treating the sample or applying cold work, as this acts to remove the larger grains from the micro-structure [11, 16, 43].

2.1.3 Guided and Surface Acoustic Waves

The interaction of waves with the boundaries of the medium can affect the properties of the wave, and leads to a multitude of new modes of propagation. These new waves can be split into two broad groups; surface waves and guided waves. Surface acoustic waves (SAW) exist and propagate on the interface between two different media, whereas guided waves are constrained by two interfaces of a bounded medium [27]. These waves differ from bulk waves due to the imposition of boundary conditions at the interfaces, which affects their propagation behaviour.

Surface waves can exist in semi-infinite media with only a single surface, to which they are constrained. There are numerous possible surface wave modes that can exist, including head and creep waves [35], Rayleigh waves [27] and Stoneley waves [26]. All of these surface acoustic waves have an amplitude that decays exponentially with depth, d [26–28]:

$$A = A_0 e^{-d/2\lambda}. \tag{2.23}$$

This shows that the ultrasonic wave is constrained to the surface, with most of the energy contained within a depth approximately equal to the wavelength, λ [26, 46]. As most of the energy is restricted to the interface, these waves are very sensitive to surface conditions of the medium. Whilst it means that SAW are severely damped by surface roughness or impurities that have a similar scale to the ultrasonic wavelength [4], they can be deployed with great effect to the detection of surface-breaking defects. The most widely used surface wave in NDT is the Rayleigh wave, which has an elliptical particle displacement on a free surface [26–28]. Rayleigh waves have been used extensively in NDT to detect, as well as determine the size and

inclination of, surface-breaking defects, as well as size and determine the inclination of the defects to the sample surface [47–51]. Also, as the energy is confined to the surface, the geometric attenuation for a point source varies as $1/R$, meaning that Rayleigh waves can propagate further than bulk waves, making them useful for inspecting inaccessible regions [4].

Guided waves, rather than being constrained to a single interface, are contained within a finite structure. These waves have energy flow primarily along the length of the waveguide [36]. Consequently, the waves will follow the potentially complex curvatures of the waveguide, meaning that they can be used to direct the waves to more inaccessible or hostile regions [52, 53]. The propagation characteristics of guided waves are determined not only by material constants, but also by the geometry of the waveguide itself and the appropriate boundary conditions for the structure [27, 36]. For each particular problem, with its own geometry and boundary conditions, there will be a particular set of guided wave solutions. These sets of solutions correspond to an infinite number of guided modes that can be supported within a structure [27, 28]. The propagation of each member of the set of solutions can be obtained from the dispersion relations of the relevant ultrasonic mode, which describe how the wave velocities of the various guided wave modes are related to the frequency of the wave mode. Whilst there are a number of different guided waves, attention will be focused on SH waves, as these waves were used in this work.

2.1.3.1 Shear Horizontal Waves

SH waves exist as guided waves in a free plate, with the particle displacement polarised parallel to the surface of the waveguide [26, 27]. The exact geometry, shown in figure 2.2, can be used to derive the dispersion relation that describe the propagation of SH guided wave modes. The SH wave, with particle displacement polarised in the x_3 direction, is travelling along the x_1 direction of a plate of x_2-thickness $d = 2h$. As seen in section 2.1.2.2, SH waves were found to undergo total reflection at a

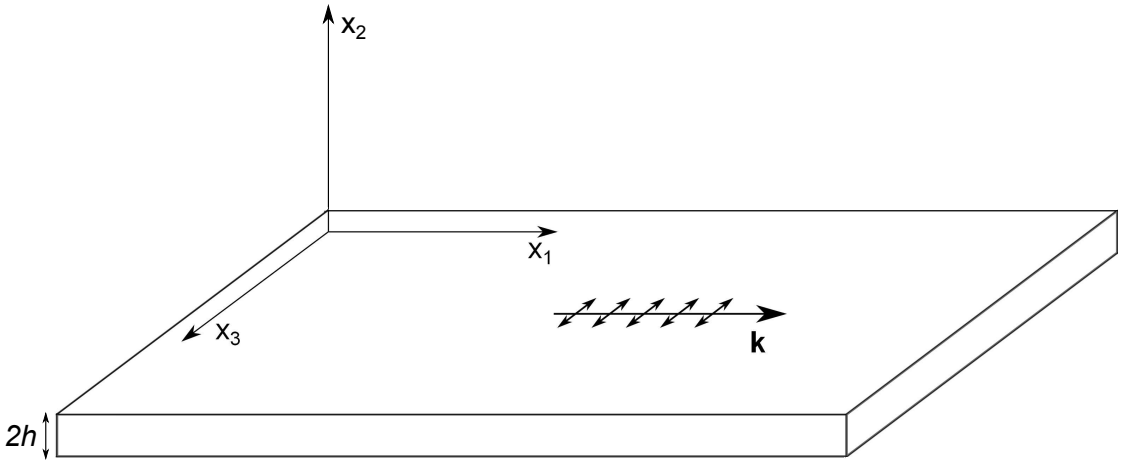

Figure 2.2: SH plate geometry, which indicates the propagation of the wave through the wavevector **k**, and the shear displacement by the arrows orientated along the x_3 axis.

free interface without a phase change [37, 54]. As the SH waves are bound between two parallel plates, the various incident and reflected waves can interfere with each other. It is the interference of these partial waves that leads to the propagation characteristics of SH guided waves [26–28, 36]. By applying partial wave analysis, the dispersion relation for SH waves is found to be [27, 28, 55]:

$$k^2 = \left(\frac{\omega}{v_s}\right)^2 - \left(\frac{n\pi}{d}\right)^2, \tag{2.24}$$

where $k = \frac{2\pi}{\lambda}$ represents the wavenumber, and n is an index representing the order of the mode. This dispersion relation can be used to determine characteristics of SH wave propagation, such as the phase speed, c_p, and group speed, c_g:

$$c_p = \frac{\omega}{k} = 2v_s \frac{fd}{\sqrt{4\left(fd\right)^2 - \left(nv_s\right)^2}}, \tag{2.25}$$

$$c_g = \frac{\mathrm{d}\omega}{\mathrm{d}k} = v_s \sqrt{1 - \left(\frac{nv_s}{2fd}\right)^2}. \tag{2.26}$$

For the fundamental SH_0 ($n = 0$) mode, both the phase and group speeds are equal to the bulk shear speed v_s for all frequencies. However, for all other modes, the propagation is dispersive, with the speed of propagation dependent upon frequency.

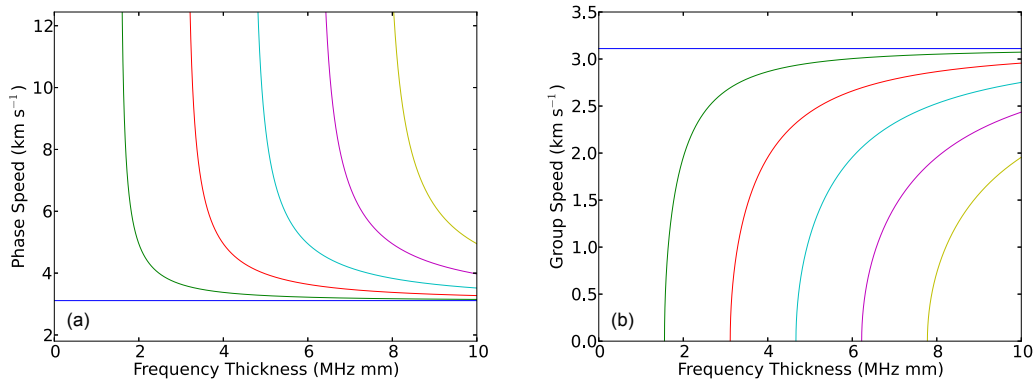

Figure 2.3: (a) Phase speed and (b) group speed of first six SH guided waves in aluminium ($v_s = 3111$ ms^{-1}).

The phase and group speeds are shown in figure 2.3. It can be seen that as well as being dispersive, the group speed of these higher modes reach zero at certain frequency-thicknesses, with the modes not existing below this value. These values are called the cut-off frequencies, and show the frequency thickness values at which the modes can exist; below the cut-off frequency, the mode becomes evanescent and exponentially dies away with distance [26, 27]. The cut-off frequency for the n^{th} mode, $C_n = (fd)_n$, is given by:

$$C_n = \frac{nv_s}{2}. \tag{2.27}$$

If a higher order mode arrives at an area of thinning of a plate, so that the frequency-thickness falls below a cut-off, then two phenomena can occur. The original wave can either be mode converted into a lower order mode or be reflected, depending on the abruptness of the change of thickness [55, 56]. The scattering of SH guided waves from steps, notches and cracks has also been extensively studied in the literature [57–59].

It can be seen from figure 2.3 that the SH modes are particularly dispersive close to their cut-off frequencies. Also, as the frequency increases and tends towards infinity, both the phase and group speeds converge to the bulk shear speed. This is because, as the frequency thickness increases, the thickness of the plate re-

lative to wavelength of the SH waves increases so that the waves propagate as if they were in an unbounded medium. As well as having different speed profiles, the modes also have unique displacement curves through the thickness of the plate, as shown in figure 2.4. The modes can be split into two groups; symmetric modes and anti-symmetric modes [27]. Symmetric modes, which have even mode numbers ($n = 0, 2, 4, \ldots$), have displacement distributions that are symmetric about the centre of the plate. Conversely, anti-symmetric modes ($n = 1, 3, 5, \ldots$) have a displacement node in the centre of the plate, and are obviously anti-symmetric [28]. The displacement in the x_3-direction is [27, 28, 60]:

$$u_3^s(x_1, x_2, t) = B_1 \cos\left(\frac{n\pi}{d} x_2\right) e^{i(kx_1 - \omega t)}, \tag{2.28}$$

$$u_3^a(x_1, x_2, t) = B_2 \sin\left(\frac{n\pi}{d} x_2\right) e^{i(kx_1 - \omega t)}. \tag{2.29}$$

Where u_3^s represents the displacement of the symmetric modes, and u_3^a represents the anti-symmetric displacement. Again, the fundamental SH_0 mode proves to be the simplest case, with the displacement distribution constant across the thickness of the plate. As the mode number increases, so the complexity of the displacement profile increases, as does the number of nodes in the profiles. Nodes represent an issue for the use of SH waves in practical applications, as the lack of displacement at these points means that plate can not be inspected at this point. Consequently, it is common for only the first two modes to be used for NDT.

SH waves have a number of properties that make them attractive for use in non-destructive testing. As has been seen, when SH waves are incident upon an interface, they do not mode convert into waves of other polarisation. The simplicity of the dispersion relations, when compared to Rayleigh-Lamb waves [27], also aids the analysis of the resultant data. Recent work has also demonstrated that SH guided waves can very easily propagate around curved sections of a sample, with

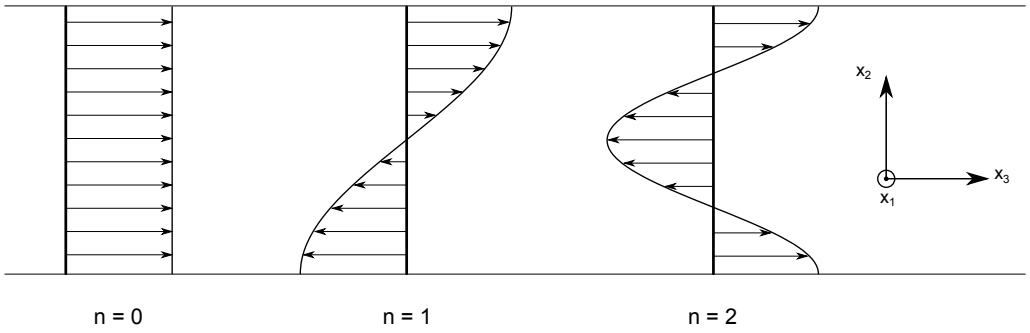

Figure 2.4: Maximum displacement distributions for the first three SH modes.

a very small reflection coefficient [61]. This property, coupled with the inherently low geometric attenuation of guided waves in the low frequency-thickness regime, means that they could be potentially use to detect defects over large distances, even if the path is complex and contains sharp bends. Finally, as SH wave are typically polarised parallel to the direction of an austenitic weld, they can pass through the weld with limited beam steering and attenuation [62–65]. As a consequence of these properties, SH waves have been utilised in a range of NDT scenarios. For instance, they have been used to inspect welds [62, 64, 66, 67], pipes [68, 69] and plates [57–59, 66] for defects, as well as thickness changes in samples [53, 55, 56]. As the speeds of higher order SH waves are dependent upon the thickness of the plate, they can be used to determine the thickness of plates, even without knowledge of the material properties [8].

2.2 Ultrasonic Transduction

There is a whole range of available methods of generating and receiving ultrasonic energy, with each method having unique advantages. A brief review of some of the most relevant techniques is given here. Particular attention is given to electromagnetic acoustic transducers (EMATs), as this is the main transducer used in this work. Transducers are generally split into two groups, contact and non-contact, depending on whether direct coupling with the sample is required. Piezoelectric

transducers, which require physical contact with the sample, are by far the most common transducer type. Their popularity is mainly a consequence of simplicity of implementation and the high efficiency levels that are possible to obtain with piezoelectric transducers. However, the requirement for contact with the surface through a couplant material makes the use of these transducers impractical for some purposes, for instance, working in a hostile environment [70], or if the transducer needs to be rapidly scanned along a sample. This has lead to the rise in usage of non-contact methods, such as EMATs, laser ultrasonics and air-coupled transducers, as they allow for scanning of a sample at speed or working with samples at elevated temperatures.

2.2.1 Electromagnetic Acoustic Transducers

EMATs are a form of non-contact transducers that consist of an electrically conducting coil and a strong magnet to provide a biasing magnetic field. The coil is pulsed with an alternating electrical current, which has an ultrasonic frequency, induces dynamic electromagnetic fields in the surface region of a conductive sample. There are three mechanisms through which EMATs can couple to a sample; the Lorentz force mechanism, the magnetisation force and the magnetostriction mechanism [71, 72]. The Lorentz mechanism occurs due to the interaction between the eddy currents induced in the sample and the static magnetic field, and exists in all conducting samples. The latter two mechanisms only occur in ferromagnetic samples. The magnetisation force acts between an oscillating, external magnetic field and the magnetisation of the material, whilst the magnetostriction is caused by the piezomagnetic effect [73]. Maxwell's equations are needed in order to describe the electromagnetic interactions between the EMAT and an electrically conductive

sample:

$$\nabla \cdot \mathbf{D} = \rho_f, \tag{2.30}$$

$$\nabla \cdot \mathbf{B} = 0, \tag{2.31}$$

$$\nabla \times \mathbf{E} = -\frac{\partial \mathbf{B}}{\partial t}, \tag{2.32}$$

$$\nabla \times \mathbf{H} = \mathbf{J_f} + \frac{\partial \mathbf{D}}{\partial t}, \tag{2.33}$$

where $\mathbf{E}$ represents the electric field vector, $\mathbf{B}$ is the magnetic field, $\mathbf{D}$ is the displacement vector, $\mathbf{H}$ is the magnetic field strength, $\mathbf{J_f}$ is the free current density and ρ_f is the free charge density. Also required are the constitutive relations, which relate the displacement and magnetic field strength vectors to the electric and magnetic fields:

$$\mathbf{D} = \epsilon \mathbf{E} \tag{2.34}$$

$$\mathbf{H} = \mu^{-1} \mathbf{B}. \tag{2.35}$$

Here, $\epsilon = \epsilon_r \epsilon_0$, which is the permittivity of the material and $\mu = \mu_r \mu_0$ is the permeability. If the coil is excited with an alternating current near to a conductive surface, then this time varying current induces a dynamic electromagnetic wave, which, in turn, induces an electric field within the sample, as can be seen from Faraday's law, equation 2.32. This electric field drives eddy currents within the sample. The magnetic field that is produced by these eddy, or image, currents acts to oppose the propagation of the electromagnetic wave, as explained by Lenz's law [74]. This opposition leads to the eddy currents only being induced within a certain depth from the surface of an electrically conducting sample. The depth of penetration is called the electromagnetic skin-depth, δ, and is given for a plane wave in a good conductor by [17]:

$$\delta = \sqrt{\frac{2}{\omega\mu\sigma}}. \tag{2.36}$$

The electromagnetic skin-depth is inversely proportional to the frequency of the electromagnetic wave, the permeability, μ, and conductivity, σ, of the sample. This leads to a plane wave solution for the electric field being [75]:

$$\mathbf{E} = \mathbf{E_0} e^{i\left(\omega t - \frac{z}{\delta}\right)} e^{-\frac{z}{\delta}}. \tag{2.37}$$

It is clear from this that the skin-depth represents the depth at which the electric field strength, $|\mathbf{E}|$, has fallen to $1/e$ of its surface value. It should also be remembered that, as well as a reduction in amplitude, the phase of electric field is linearly increasing. The current density can be calculated by utilising Ohm's law:

$$\mathbf{J} = \sigma\mathbf{E} = \mathbf{J_0} e^{i\left(\omega t - \frac{z}{\delta}\right)} e^{-\frac{z}{\delta}}. \tag{2.38}$$

This leads to most of the induced current density being restricted to the skin depth of the sample. For a frequency of 500 kHz, the skin depth in aluminium is 120 μm. This means, for ultrasonic frequencies, the skin depth is much smaller than the ultrasonic wavelength and it can be assumed that the electromagnetic fields only occur on material surfaces [71]. The total current induced in a column of unit area through the semi-infinite, conductive medium can be found by integrating the current density through the depth:

$$\begin{aligned} \mathbf{I} &= \int_0^\infty \mathbf{J}\, \mathrm{d}z \\ &= \mathbf{J_0} e^{i\omega t} \int_0^\infty e^{-(1+i)\frac{z}{\delta}}\, \mathrm{d}z \\ &= \mathbf{J_0} e^{i\omega t} \frac{\delta}{1+i} = \mathbf{I_k} e^{i\left(\omega t - \frac{\pi}{4}\right)}. \end{aligned} \tag{2.39}$$

This expression shows how the induced current can be treated as single image current, which has a phase lag of $\pi/4$ relative to the induced surface electric field described in equation 2.37. The force experienced by a particle with a charge, q, in the presence of an electric and magnetic field is called the Lorentz force [75]:

$$\mathbf{F} = q\left(\mathbf{E} + \mathbf{v} \times \mathbf{B}\right). \tag{2.40}$$

The magnetic field will not only contain the static magnetic field from the magnet, $\mathbf{B_0}$, but will also contain a contribution from the dynamic magnetic field produced by the generation current, $\mathbf{B_c}$. The static field is generally of higher amplitude than the dynamic magnetic field, although the amplitude of the dynamic field may be significant for high excitation currents, with the ultrasound generated by the dynamic magnetic field having twice the frequency [71]. In many cases, the amplitude of the dynamic field is high enough to generate ultrasonic waves without a permanent magnet providing a biasing magnetic field [76, 77]. In metallic samples, it is the free electrons that carry the current, and the equations of motion become:

$$m_e \frac{\mathrm{d}v_e}{\mathrm{d}t} = -e\left(\mathbf{E} + \mathbf{v_e} \times \mathbf{B}\right) - \frac{m\mathbf{v_e}}{\tau}, \tag{2.41}$$

where m_e is the mass of an electron, and e is the electron's charge, $\mathbf{v_e}$ is the mean electron velocity and τ is the mean time of electron-ion collisions, which is of the order of 10^{-14} s [71]. Considering a volume of the metal, which has an electron and ion density of n_e and N_i, respectively, the momentum arising from the excitation of the electrons described in equation 2.41 is imparted to ions in the conductor through collision processes [71]. Assuming that the volume has a neutral charge ($n_e e = N_i Z_i$) and that the period of the oscillations of the electric field is much longer than the mean collision time, then the force per unit volume on the ions reduces to [71, 78]:

$$\mathbf{f} = -ne\mathbf{v_e} \times \mathbf{B_0} = \mathbf{J_e} \times \mathbf{B_0}. \tag{2.42}$$

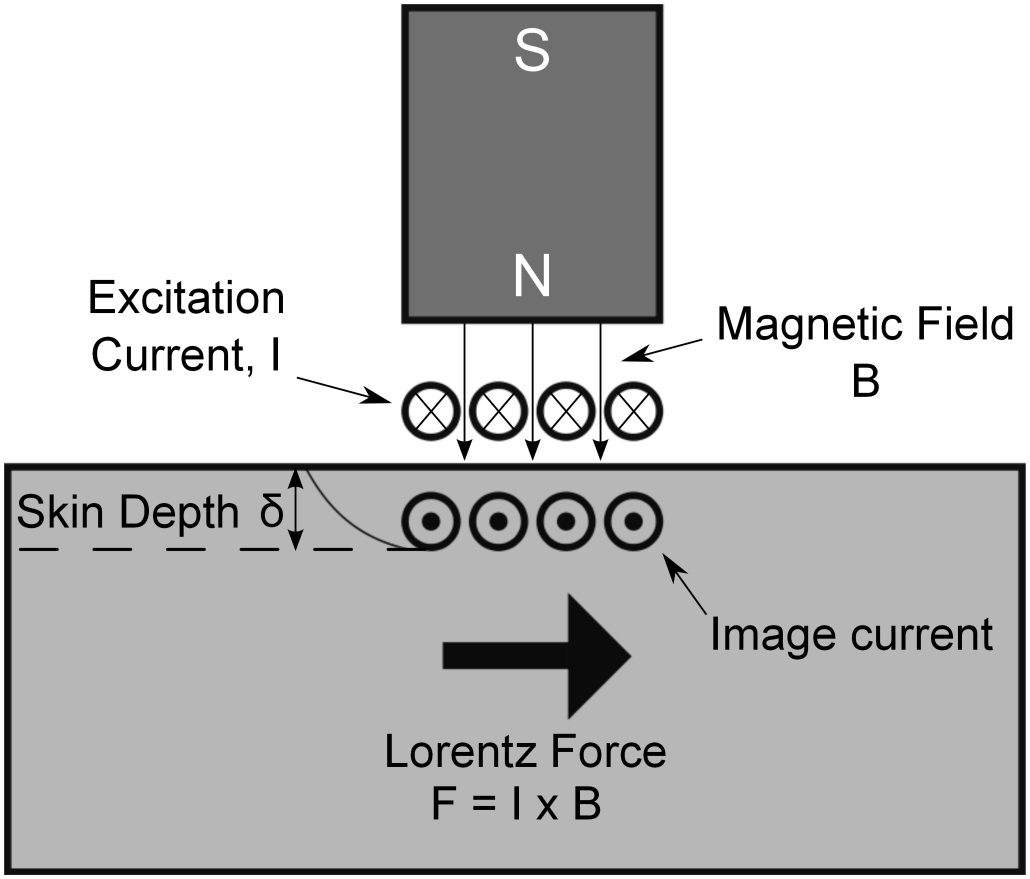

Figure 2.5: A schematic showing the Lorentz force coupling mechanism of EMATs. As the electromagnetic skin-depth is much less than the ultrasonic wavelength, the induced current can be described as an image current, as described in equation 2.39.

This expression shows how the interaction between the mirror current density and the static magnetic field creates a Lorentz force that can cause an acoustic vibration. This force is perpendicular to both to the magnetic field and the mirror current, as demonstrated in figure 2.5. The direction of the applied Lorentz force, and hence the polarisation of the generated waves, can be controlled by changing the relative directions of the magnet field and mirror current.

The Lorentz force mechanism is reversible, which means it can also be used to detect ultrasound [78]. The presence of an ultrasonic disturbance causes the material, including the ions and electrons, to oscillate in phase with the wave. When in the presence of a static magnetic field, which is orientated parallel to the displacement of the wave, both the ions and electrons experience a Lorentz force. Due to

its much smaller mass, the electrons are accelerated by this force to a much greater extent than the ions, meaning they play a dominant role in the detection of the ultrasonic wave. In a similar way to the generation Lorentz mechanism, where an image current was generated in the surface of a conducting sample, these accelerated electrons will give rise to electromagnetic fields that will induce a current in the coils of a nearby EMAT [71, 79].

As shown in the literature, EMATS are in fact velocity sensors [7, 80]. The displacement, $u\,(z,\,t)$, of an ultrasonic wave that is travelling to the surface of an sample can be described as:

$$\mathbf{u}\,(z,\,t) = u_0 e^{i(\omega t - kz)}\,\hat{\mathbf{z}}. \tag{2.43}$$

Here, $\hat{\mathbf{z}}$ denotes a unit vector that is perpendicular to the plane defined by the surface of the sample. At this surface, the wave will be reflected, and so the surface displacement vector, ξ, is the sum of these two waves:

$$\begin{aligned} \xi &= u_0 e^{i\omega t}\left(e^{-ikz} + e^{ikz}\right)\,\hat{\mathbf{z}} \\ &= 2u_0 \cos\left(kz\right) e^{i\omega t}\,\hat{\mathbf{z}}. \end{aligned} \tag{2.44}$$

A dynamic electric field is created by the electrons' motion in a static magnetic field and is given by [71, 78, 79]:

$$\mathbf{E_d} = \frac{\partial \xi}{\partial t} \times \mathbf{B_0}. \tag{2.45}$$

As the displacement field and magnetic field are perpendicular to one another, this means that the magnitude of the induced current density is given by:

$$|\mathbf{J}| = 2i\omega\sigma u_0 \cos\left(kz\right) e^{i\omega t} |\mathbf{B_0}|. \tag{2.46}$$

This can be integrated throughout the skin depth, δ, to yield an average value

of the induced current density within this range:

$$\begin{aligned} J &= \frac{1}{\delta}\int_0^{\delta} 2i\omega\sigma u_0 \cos(kz)\, e^{i\omega t}|\mathbf{B_0}|\, \mathrm{d}z \\ &= \frac{2i\omega\sigma}{k\delta} u_0 e^{i\omega t}\, |\mathbf{B_0}| \sin(kz)\,. \end{aligned} \tag{2.47}$$

However, as the eddy current density, $\mathbf{J}$, is confined within the skin depth, and this skin depth is generally much smaller than the ultrasonic wavelength, then the small angle approximation can be used to state that $\sin(kd) \sim kd$ and hence the expression simplifies to:

$$\begin{aligned} J &= 2i\omega\sigma\, |\mathbf{B_0}|\, u_0 e^{i\omega t} \\ &= 2\sigma\, |\mathbf{B_0}|\, \frac{\partial u(0,\, t)}{\partial t}. \end{aligned} \tag{2.48}$$

It is this current density that is detected by the coil of the EMAT [79]. From equation 2.48, it can be seen that the EMAT does indeed act as a velocity sensor, as it measures the temporal derivative of wave displacement on the surface.

Whilst the Lorentz force acts to generate ultrasound in all conductive materials, there are a further two mechanisms that are present only in ferromagnetic materials [71, 72, 81]. Aluminium is primarily used in this work, and so does not experience the ferromagnetic coupling contributions. However, it is important to discuss these mechanisms, which are termed the magnetisation force and the magnetostriction force [71]. The magnetisation force arises in a ferromagnetic material that is exposed to an external magnetic field strength, $\mathbf{H}$. The magnetisation force occurs when the generated electromagnetic field interacts with the internal magnetisation that is induced in the material, causing a re-orientation of the magnetic dipoles within the material [82]. This magnetisation force is split into two components; a volume force, $\mathbf{F_v}$, and a surface force, $\mathbf{F_s}$ [71]:

$$\mathbf{F_M} = \mathbf{F_v} + \mathbf{F_s} = \int_v \nabla^* \left(\mathbf{M} \cdot \mathbf{H}\right) \mathrm{d}\mathbf{x^3} + \frac{1}{2}\mu_0 \int_s M_n^2 \hat{\mathbf{n}}\, \mathrm{d}\mathbf{x^2}, \tag{2.49}$$

where ∇^* denotes a gradient operator that acts only on $\mathbf{H}$. It has been noted that for tangential biasing magnetic fields, the magnetisation force acts to oppose the Lorentz force, meaning that EMATs are ineffective in generating longitudinal forces in ferromagnetic materials [71, 72].

The final mode that the EMAT can couple to a sample is through the magnetostriction force. This force is generated because the magnetic domains want to align with an external magnetic field, which leads to a net mechanical strain [73]. The magnetic domain walls will either move, or the polarisation of the domains will rotate to cause this mechanical deformation [83]. If the magnetic field is time dependent, then the dimensions of the ferromagnetic material will change, which can be used to launch an ultrasonic wave [68, 71, 72, 84]. Whilst, for polycrystalline materials, the magnetostrictive effect is non-linear, the dynamic magnetic field is small in comparison to the larger bias field [71, 83, 84]. This means that, locally, the effect can be assumed to be a linear phenomenon [85].

A lot of work related to the coupling of EMATs with ferromagnetic samples has been focused on the relative strength of the magnetostrictive mechanism compared to the Lorentz force [86]. For low biasing field strengths, the magnetostrictive force dominates over the Lorentz mechanism, with the latter becoming more important for strong fields [84, 86, 87]. The Lorentz force becomes dominant at high field strengths as the mechanism increases linearly, whilst magnetostriction saturates at a particular field strength, which depends upon the sample type [87]. The direction of the applied magnetic field is also important in determining the efficiency of the respective mechanisms. For example, if the current density and magnetic field act in the same direction, there will be no Lorentz force generated, whilst magnetostriction can still occur.

As with the Lorentz force mechanism, the magnetostrictive effect is also revers-

ible, meaning it can also be used to detect ultrasonic disturbances. This inverse magnetostrictive, or Villari, effect appears as the application of tensile stress gives rise to change in magnetic flux [25, 88]. The magnetic flux induces a current in the coils of the EMAT, meaning that the ultrasonic disturbance can be detected [25,71].

Whilst these electromagnetic coupling mechanisms mean that the transducer does not require contact with the sample, the transducer's efficiency is greatly reduced as the distance between sample and sensor is increased [89, 90]. As the electromagnetic fields decrease in amplitude exponentially, the lift-off of the transducer is limited to a few millimetres [85, 89]. However, these few millimetres offer a significant number of potential advantages. For instance, as the transducer is not in contact with the test sample, it can be automatically scanned, even at speed [16]. Also, the EMAT does not provide mechanical loading and does not require liquid couplant, ensuring that the coupling between transducer and sample occurs with repeatable efficiency [86, 91]. EMATs can also be used for high temperature work, as problems involving liquid couplant and cooling are reduced [91,92]. They can also be used to generate ultrasound in metals that are covered in a protective coating, provided that the coating is not too thick or conductive [91].

However, these advantages come at a cost. The efficiency of generation of ultrasound for EMATs is very low, especially when compared to piezoelectric transducers [91]. EMATs only work effectively on highly conductive materials or strongly magnetostrictive samples. This leads to poor signal to noise ratios in materials such as austenitic steel, which is non-ferromagnetic and is an order of magnitude more resistive than aluminium [93]. Other important engineering materials, such as composites or plastics, cannot be inspected unless the sample is coated in a conducting layer [94]. Also, as different coupling mechanisms are more or less dominant in different materials, transducers may not be transferable between samples [84]. In addition to this, EMATs have poor transduction efficiency for frequencies greater than a few megahertz. This can be attributed to the electrical impedance of the

coil required to construct the EMAT. Whilst increasing the number of turns in the EMAT coil may, at first, appear to always increase the signal amplitude, this is not true. By adding more turns to the coil, the inter-wind capacitance will increase as well as the mutual inductance of the coil [95]. As the electrical impedance of an inductor linearly increases with frequency, the efficiency of EMATs to generate or detect ultrasonic waves with a frequency above a few megahertz is significantly reduced [96].

Despite these disadvantages, they have a range of properties that make them indispensable for NDT purposes. As the direction of the generated force is controlled by the orientation of the magnet and the coil, the polarisation of the wave can be carefully controlled [71, 97]. This has been demonstrated in the literature, with a whole range of EMATs being created to generate various different wave modes [38,70,72,81,83,97–100]. A particular advantage of EMATs is that they can be used to generate SH wave modes. SH waves are difficult to generate using piezoelectric transducers, as the shear energy cannot propagate through low viscosity coupling fluid, and they cannot be excited via mode conversion either [38, 83]. However, SH waves can be easily and efficiently generated using EMATs [38, 68, 70, 83].

2.2.1.1 Periodic Permanent Magnet EMAT

One way of generating SH waves is to use periodic permanent magnet (PPM) EMATs [38,68,70]. A PPM EMAT consists of an array of magnets, which alternate polarity with their nearest neighbours, and a racetrack coil that is excited with an alternating current. The configuration can is shown schematically in figure 2.6. The alternating polarity of the magnet array means that, in non-ferromagnetic samples, the PPM EMAT sets up an alternating Lorentz force within the skin depth of the sample. It is this Lorentz force arrangement, caused as a result of the interaction between the induced eddy currents and the static magnetic field, which generates the SH wave. The generated SH wave has a wavelength on the surface equal to the periodic

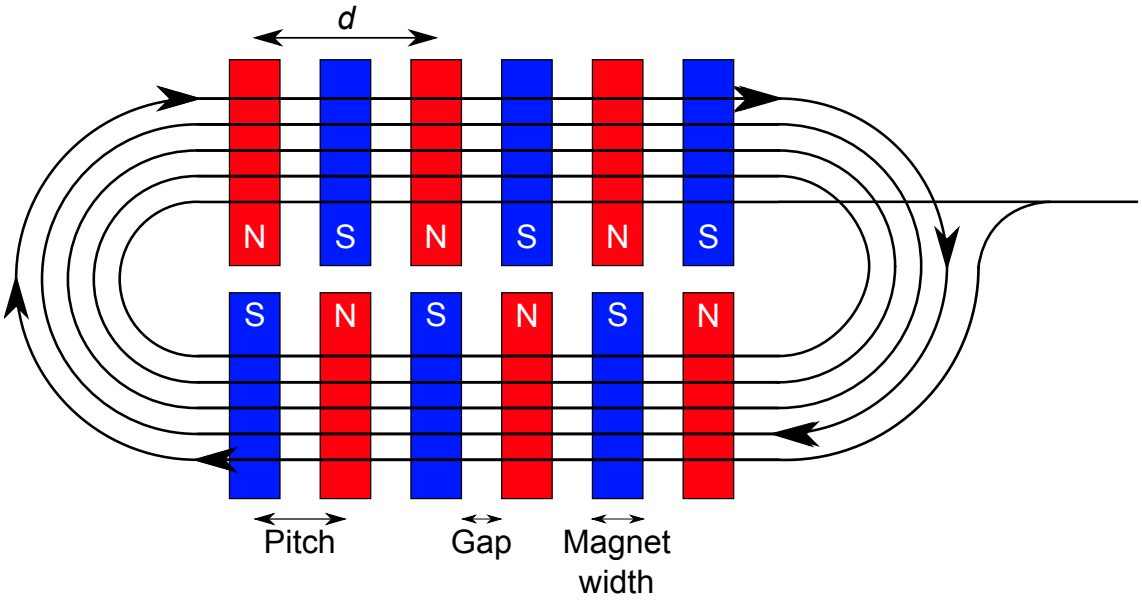

Figure 2.6: PPM EMAT configuration, showing the layout of the magnets and racetrack coil.

distance of the array, d, which is twice the pitch of the PPM array. The EMAT needs to be kept close to the sample so that the alternating magnetic field pattern leads to a similar force distribution on the surface of the sample. The force distribution generated by an EMAT shown in figure 2.6 leads to six isolated regions of applied force that can be considered as individual elements.

The generated SH waves can also be launched at an angle into the bulk of a sample [97, 98]. This method utilises the spatial periodicity of the magnet array of the PPM EMAT [101]. By driving the array with a narrowband signal, the waves created from the individual elements will interfere with each other. This leads to constructive interference at a particular angle, with the signal destructively interfering at other angles. Constructive interference occurs when the path length difference between the waves from two elements of the same polarity is equal to an odd integer number of wavelengths, as shown in figure 2.7. This condition changes with frequency, and hence the SH beam can be steered by simply changing the frequency of the tone-burst excitation [101, 102]. The relation between the angle, θ, at which the SH wave of wavelength, λ, is steered by a PPM EMAT with a periodic

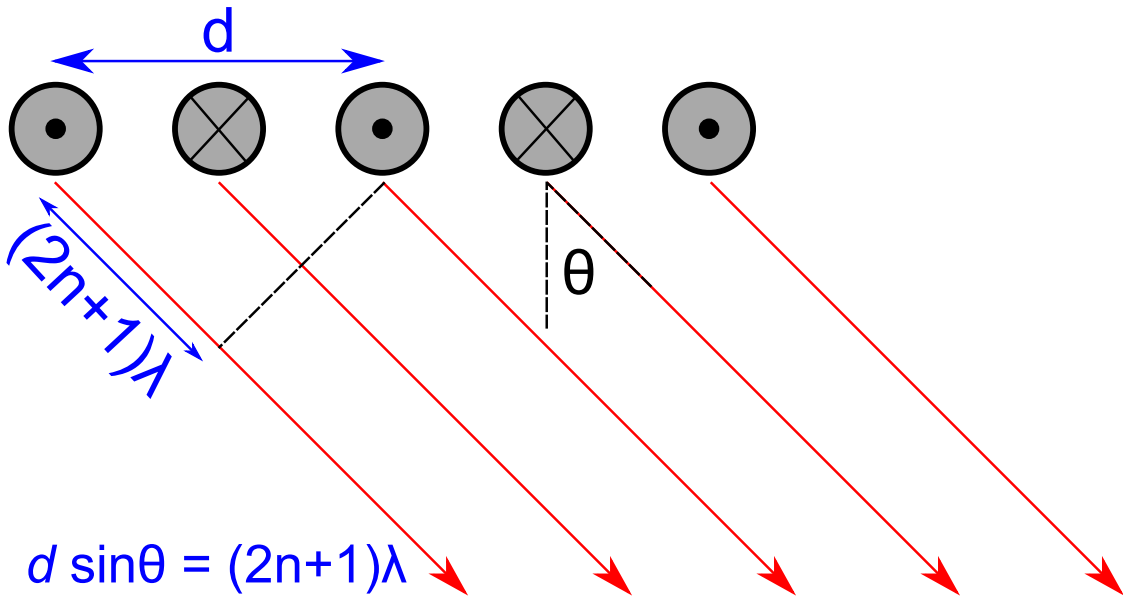

Figure 2.7: Array configuration, which shows the surface force distribution. It shows how the condition for constructive interference can be derived.

distance, d, is given by [101, 102]:

$$d \sin\theta = (2n+1)\,\lambda. \tag{2.50}$$

Here, n is an integer index that refers to the order of interference. This relation is reminiscent of the diffraction grating equation. However, as the frequency of the generated wave is inversely proportional to the physical size of the array, thinner magnets are required to generate higher frequency waves [71]. As the magnets become smaller, the field strength, and therefore the efficiency, of the EMAT is reduced. This means that there is a compromise between the efficiency of the EMAT and the frequency that it can generate. Typically, the smallest magnets that are used are 1 mm wide, which restricts the SH wave frequency to below 1.6 MHz for common steels [71].

2.2.2 Piezoelectric Transducers

Currently, the dominant technology for ultrasonic transduction incorporates piezoelectric materials, mainly for their simplicity of use and high signal-to-noise ratios

that can be achieved [4,6]. When a piezoelectric material is deformed by mechanical stress, electrical charge develops on the surface of the material [6, 91]. Hence, if an acoustic wave impinges on the transducer, the pressure of the wave will generate electric charge that can be detected and used to infer the presence and details of an ultrasonic disturbance. This relationship between deformation of the material and generation of electric charge is reciprocal; the dimensions of the piezoelectric material change under the application of an electric field, and this is known as the inverse piezoelectric effect [4, 16, 26, 91]. Hence, a piezoelectric transducer can be used to generate and receive ultrasonic waves.

All materials that exhibit piezoelectric behaviour must also have a microscopic crystallographic structure that lacks any centre of symmetry. This lack of a centre of symmetry is important because it ensures a separation of the positive and negative charge within the unit cell. This separation of charge creates an electric dipole, and is responsible for the piezoelectric behaviour. The axis along which this asymmetry is present makes it possible to generate either longitudinal or shear displacements [91]. Whilst piezoelectric ceramics will not have a bulk crystallographic structure, the material will comprise of a collection of randomly orientated crystalline structures, which will have a unit cell that lacks a centre of symmetry. Typical materials used in modern transducers are ceramics rather than single crystals, and examples are Barium Titanate (BaTi) and Lead Zirconate Titanate (PZT), amongst others. Due to the reciprocity of the piezoelectric effect, both the elastic and electrical properties are coupled and are described by the following linear equations [91, 103]:

$$\mathbf{D} = d\mathbf{T} + \varepsilon^T \mathbf{E}, \tag{2.51}$$

$$\mathbf{S} = s^E \mathbf{T} + d\mathbf{E}. \tag{2.52}$$

Where $\mathbf{D}$ is the electric displacement, $\mathbf{E}$ is the electric field, $\mathbf{S}$ is the elastic strain,

$\mathbf{T}$ is the elastic stress, ε^T is the permittivity of the piezoelectric material under constant stress, and s^E is the mechanical compliance for a constant electric field. d is the piezoelectric charge constant, which is defined as the electric polarisation generated per unit mechanical stress that is applied [103]. Piezoelectric transducers are usually utilised as thickness resonators, with the operational frequency of the transducer determined by the thickness of the active element as well as by its material properties [6, 91, 103]. Normally, there will be many of these resonances, associated with thickness or lateral modes as well as coupled modes between the two. However, usually the transducer is required to operate when it is oscillating in the thickness mode only. In order for this to occur, the resonances associated with the thickness mode must be isolated from any other modes. Analysis of the vibrational behaviour of piezoelectrics can be performed using a range of modelling techniques [104–109].

As the ultrasonic excitations exist within the piezoelectric material, the energy must be able to be easily transferred between the transducer and the sample. However, the acoustic impedance of the piezoelectric material is generally very dissimilar to that of the load material, leading to a requirement for a matching layer. The matching layer's purpose is to bridge the acoustic impedance difference between the piezoelectric material and the sample that is to be inspected [16, 91]. For a single matching layer, the optimum acoustic impedance of the matching layer is the geometric mean of the active material and the load material, $\sqrt{Z_T Z_L}$ [110]. It has also been shown that the optimum thickness for a matching layer is a quarter of the wavelength, meaning that successive reverberations in the matching layers will be in phase with each other, and therefore will re-enforce each other [26, 110, 111]. In addition to this, liquid couplant is often required to couple the transducer with the test subject. This leads to two drawbacks of piezoelectric transducers; that direct physical contact is required, and that, because of the liquid couplant, the coupling efficiency is not repeatable. This makes the use of piezoelectric transducers for certain scenarios, such as working at elevated temperatures or work involving scanning,

more difficult than with non-contact methods.

2.2.3 Other Transduction Methods

There are a whole host of other transduction methods that are used, with the topic still an active area of research. For example, laser ultrasonics is an expanding area of research. Laser ultrasonics is a truly non-contact approach, as there can be a relatively large distance between the sample and laser [91, 112]. The laser spot used to generate and detect ultrasound can be focused to a small spot size, typically less than 100 μm. This, coupled with the temporally sharp pulse of laser energy, means that the generated ultrasound is of a broadband nature [91, 96]. However, unlike piezoelectric transducers and EMATs, the mechanisms for generation and detection are not reversible. This means that separate generation and detection lasers are needed, which increases the cost of an already expensive system [91]. Detailed reviews of the various mechanisms for generating and detecting ultrasonic disturbances using lasers can be found in the literature [91, 96, 113].

2.3 Advanced Ultrasonics

The basic ultrasonic technique is called pulse-echo inspection, and describes a technique where a pulse of ultrasonic energy is generated by a single transducer, passes through a sample, and is reflected back to the transducer [4]. As a flaw or defect will reflect or scatter some of the ultrasonic energy, an echo will be detected. This time of flight of this echo gives information about the presence and location of a discontinuity in the test sample [4, 6, 16]. More advanced techniques have been developed that improve the spatial resolution of these measurements, and can even be used to create ultrasonic images of the test sample.

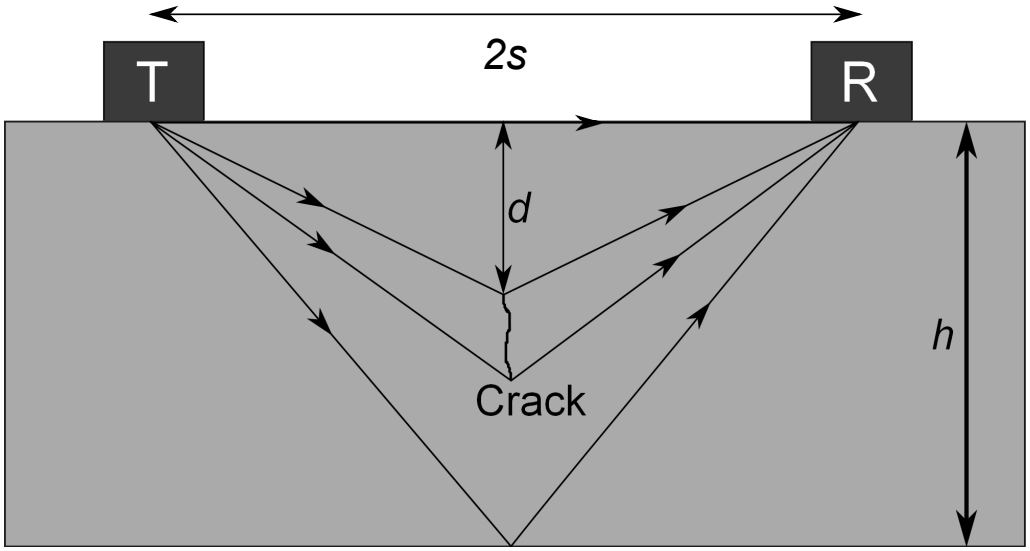

Figure 2.8: Example time of flight diffraction configuration.

2.3.1 Time of flight Diffraction Technique

The pulse-echo technique relies on detecting specular reflections from planar defects, which relies on favourable alignment [35]. Instead, the time of flight diffraction (TOFD) technique uses signals diffracted from the tips of a crack [35]. By measuring the time of flight of the tip diffracted signals, it is possible to locate and size the crack. A typical TOFD arrangement is shown in figure 2.8, which demonstrates how a two transducer system can be used to locate a vertically aligned crack. It consists of a transmitted transducer, T, which emits an ultrasonic pulse that propagates through an isotropic medium. Some of this ultrasonic energy will be incident on the crack, and get scattered by it. As well as reflections of the incident wave from the crack, there will also be diffraction of the wave from the crack tips. The diffracted energy will be spread over a large angular range [114], with some of this energy being detected by the receiving transducers, R.

By scanning the pair of transducers along the surface of the sample, the lateral position of the defect can be found. The time domain data obtained at a single scan position is typically referred to as an A-scan. By stacking a series of these A-scans together, a B-scan can be formed. The time of flight of the crack tip diffracted signals

will vary as the transducers are scanned across the sample, leading to characteristic parabola-shaped signals being formed in the B-scan [115–117]. The lateral position of the defect can be found from the scan position that minimises the time of flight, which corresponds to the vertex of the parabola [35]. By analysing these parabolas, it is possible to determine the position and size of the defect. The depth of the crack, and the through-wall extent of the crack can be calculated by analysing the arrival times of several key signals. These can be calculated from geometry, and are given by:

$$t_l = \frac{2s}{c_1}, \tag{2.53}$$

$$t_1 = \frac{\sqrt{(s-x)^2 + d^2}}{c_1} + \frac{\sqrt{(s+x)^2 + d^2}}{c_2}, \tag{2.54}$$

$$t_2 = \frac{\sqrt{(s-x)^2 + (d+a)^2}}{c_1} + \frac{\sqrt{(s+x)^2 + (d+a)^2}}{c_2}, \tag{2.55}$$

$$t_{bw} = \frac{2\sqrt{s^2 + h^2}}{c_1}. \tag{2.56}$$

The time of flight of the signals from the top and bottom of the crack are given by t_1 and t_2, respectively. The surface travelling wave travelling takes a time t_l to travel from the transmitting transducer to the receiving transducer, whilst the back-wall reflection has a time of flight equal to t_{bw}. The speed of the wave used in the inspection is denoted as c_1 and c_2 (to allow for mode conversion), with x being the displacement of the probes relative to the lateral position of the crack. When the crack is midway between the two probes, which can be found by minimising the time of flight, equation 2.54 can be re-arranged to give the depth of the crack. Assuming that the diffracted wave does not mode convert and therefore has the same wave speed as the incident wave, it becomes [116]:

$$d = \frac{1}{2}\sqrt{(c_1 t_1)^2 - 4s^2}. \tag{2.57}$$

The through-wall extent of the crack can be found from re-arranging equation 2.55, to form:

$$a = \frac{1}{2}\sqrt{(c_1 t_2)^2 - 4s^2} \; - d. \tag{2.58}$$

These expressions have been derived from a vertically oriented crack, although expressions can be found for inclined defects [117]. Typically, longitudinal waves are used for TOFD inspections, as it will always be the fastest wave, and avoids ambiguity in identifying the different modes [35]. It also means that the diffracted signals will always arrive between the lateral surface wave and the back-wall reflection. However, there has been work using shear waves for TOFD inspection, especially for sizing surface breaking cracks or thin samples [118]. Recent work in the area has been attempting to automate the TOFD process; both in terms of data acquisition and data analysis [115, 116, 119].

Whilst TOFD has proven useful in being able to accurately size cracks, there are a number of scenarios where TOFD cannot be applied. In particular, the use of TOFD to detect and size cracks that are close to the surface of the sample is limited. This is because the low amplitude diffracted signals get obscured by the surface lateral wave [118]. Also, due to the limited efficiency of tip diffraction, the signal amplitudes are generally very small and hence have poor SNR, precluding the use of TOFD in highly attenuative material. Indeed, the limited amplitudes of SH diffraction signal means that TOFD can not be performed with these waves [52,120].

2.3.2 Synthetic Aperture Focusing Technique

The Synthetic Aperture Focusing Technique (SAFT) can be split into two sequential stages. First, the radio frequency pulse-echo data is obtained, before then being processed to form an ultrasonic image. The SAFT requires pulse-echo measurements that are obtained from a single transducer that is scanned along the surface of a

sample. For each of the pulse echo measurements, the time of flight of the echoes from any defects that may be present will be different. This ultrasonic data can then be utilised to form an image by applying an appropriate time shift to the data, and coherently summing. The processing of the scanned data can be used to mimic the focal properties of a much larger transducer [121] - creating a synthetic aperture. As well as the increased lateral resolution, obtained from the larger synthetic aperture [122–124], the coherent summing algorithm acts to increase the SNR of the data, as the defect echoes constructively interfere, whilst the micro-structure noise will destructively interfere [116, 125]. This makes the SAFT, unlike TOFD, good for use with data that has a low SNR, as may be obtained when inspecting highly attenuative materials. However, the SAFT is very susceptible to imaging artefacts caused by grating and side lobes [126–128]. Work has been performed to try to alleviate these problems, for example, by using dynamic focusing and aperture apodisation [128–131]. Whilst apodisation will decrease the resolution and signal-to-noise ratio of the SAFT image, it will help to reduce the side-lobe levels and the artefacts that they introduce [131].

The physical principle behind the SAFT can be seen in figure 2.9. A single ultrasonic transducer is scanned along the sample, recording pulse-echo data as the transducer is being moved. The ultrasonic data is then post-processed in order to synthetically focus the ultrasound to a point, $P(x, y)$. The return time of flight (TOF) between the transducer, which is at a location $(x_i, 0)$ and the point, P, can be calculated from geometry:

$$\tau_i(x, y) = \frac{2}{c}\sqrt{(x - x_i)^2 + y^2}. \tag{2.59}$$

Equation 2.59 describes a hyperbolic curve: this means that the defect that caused the echo with a time of flight, τ_i, will lie on this hyperbolic curve. However, when the transducer is moved to a position $(x_j, 0)$, the echo caused by the same defect will now lie on another hyperbolic curve described by the time of flight τ_j.

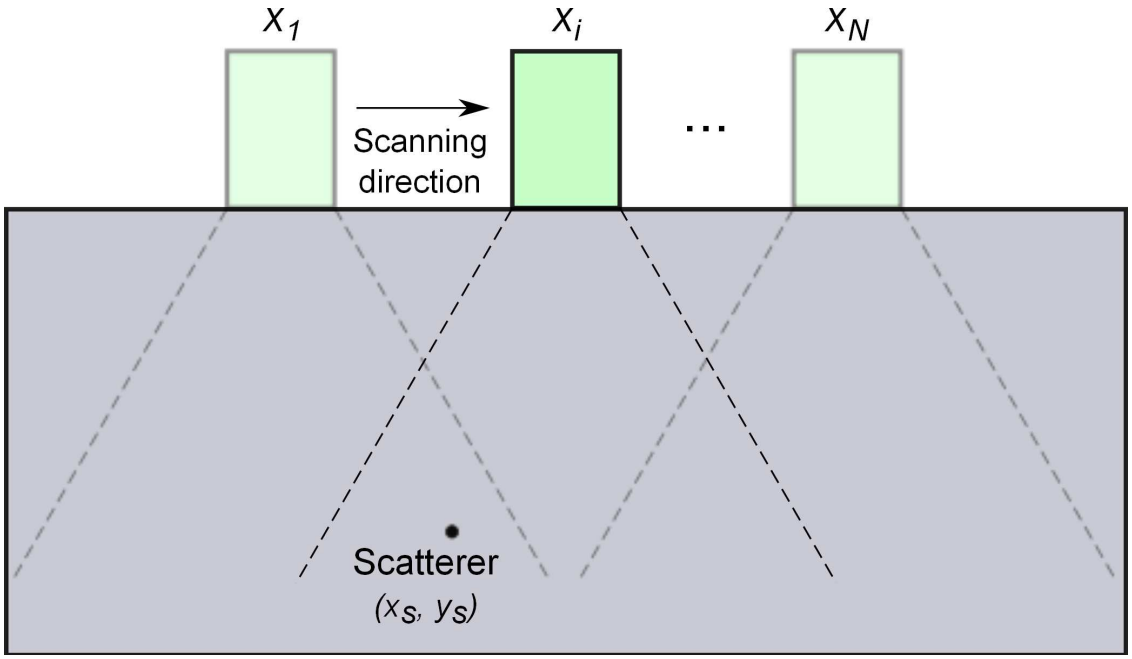

Figure 2.9: A synthetic aperture is created by scanning a transducer along the surface, whilst recording pulse-echo data.

By coherently summing these TOF curves, the location of the defect can be found as it will correspond to the position at which all of the TOF loci intersect. This is shown in figure 2.10. An ultrasonic image can be formed by splitting the inspected area into a number of pixels, and the intensity of the image given by:

$$I(x, y) = \sum_{i}^{N} s_i (t - \tau_i) . \tag{2.60}$$

Where $s_i (t - \tau_i)$ represents the radio frequency data obtained from the transducer at position $(x_i, 0)$ having being shifted in time by an amount τ_i, with the summation is over all N measurement positions. The imaging algorithm can be improved by considering the spatial impulse response of the transducer, including attenuation effects and implementing digital apodisation [122, 128, 131].

Whilst the heuristic, delay-and-sum algorithm shown in equation 2.60 is simple to understand, it can prove slow to implement, especially for a large number of measurements. However, versions of the algorithm that utilise Fourier transforms also exist, and are considerably quicker than the delay-and-sum algorithm shown

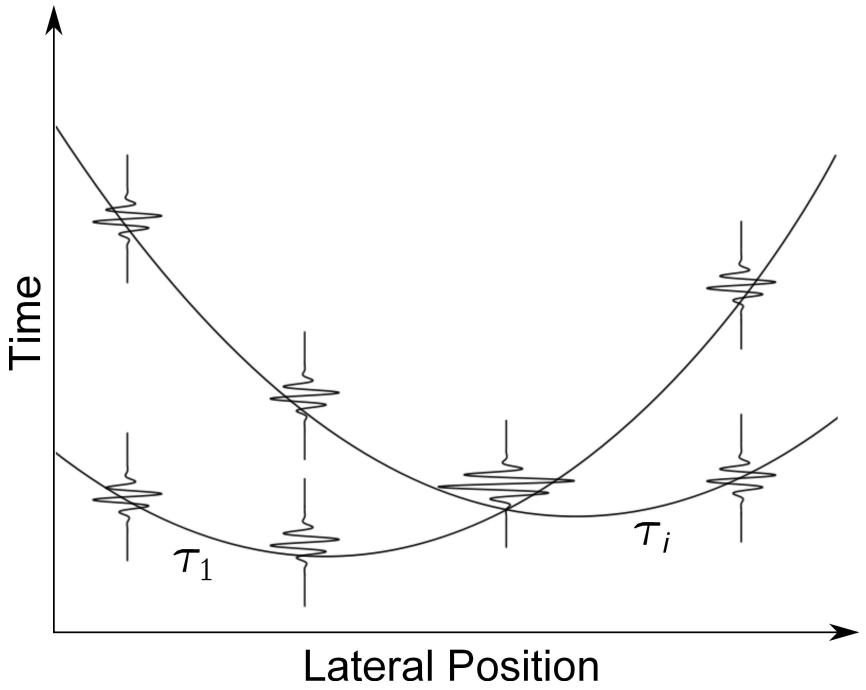

Figure 2.10: A schematic diagram showing two time of flight loci, τ_1 and τ_i, and the respective signals obtained at transducer positions x_1 and x_i that are shown in figure 2.9. The location of the defect, (x_s, y_s), is given by the intersection of the loci, where the signals constructively interfere.

here [123, 132–134].

2.3.3 Phased Array Techniques

Whereas the SAFT simulates the effect of a larger aperture by scanning a single transducer across a surface, array technology has made it possible to physically manufacture similar apertures. Ultrasonic arrays are transducers that are composed of a number of individually controllable elements. The fact that each of the elements in the array are independently controllable means that arrays are very versatile. Consequently, the array can be excited using electronic delay schemes, that individually adjust the firing of individual elements to control the ultrasonic beam [1, 3, 135–139]. These delay schemes can be changed, so that a single array is able to undertake a range of different inspections from a single location, making it much more flexible than a single element transducer [1]. Phased arrays have led to a range of ultrasonic imaging techniques being utilised [124, 140, 141].

Arrays can be created in a number of forms, and can be generally classified into one of three groups; one dimensional, two dimensional and annular arrays [1]. One dimensional linear arrays are the most popular form of array currently used, mainly due to the complexities associated with manufacturing and controlling the large number of elements that are required to create a two dimensional array. One dimensional arrays tend to be a linear arrangement of rectangular elements. Whilst it is possible to locally electrode a monolithic piezoelectric ceramic to form an array, this leads to strong elastic cross-coupling between the array elements [2]. Rather than piezoelectric ceramic, modern ultrasonic arrays are manufactured from composite piezoelectrics, as they utilise the complementary properties of piezoelectric ceramics and polymers [108, 142]. Normally incorporated into the so-called 1-3 format, where pillars of piezoelectric ceramic are embedded in a polymer phase, composite piezoelectrics offer improved acoustic matching, increased bandwidth and high piezoelectric efficiency [109, 143]. Whilst the piezoelectric efficiency of some ceramics is high, their high acoustic impedances mean that it is difficult to couple that energy into the test piece. Conversely, piezopolymers have low acoustic impedances, but high dielectric losses and low electromechanical efficiencies, which means that their sensitivity is low [142]. By combining the two materials, the quality of the transducer is improved [144].

As the elements in the array can be individually controlled, phased array methods can be used to electronically focus and steer the ultrasonic beam, within the near field of the array. The Fraunhofer distance denotes the limit between the near- and far-field, and is given by [145]:

$$D_f = \frac{2D^2}{\lambda}, \tag{2.61}$$

where D is the size of the array aperture and λ is the wavelength of the generated ultrasound. Control of the beam is achieved by applying time delays in the firing of each of the elements. By applying the correct delay between the elements, the waves

from each individual element interfere constructively at the focal point [1, 146] in accordance with Huygens' principle [39]. The appropriate delays, often called focal laws, can be calculated using simple geometry [39, 135]. For beam-steering, the appropriate time delay, $\Delta\tau$, between two neighbouring elements is given by [3]:

$$\Delta\tau = \frac{d \sin\theta}{c}, \tag{2.62}$$

where d is the spacing between the elements, θ_s is the desired steering angle and c is the speed of sound in the sample. For focusing the beam, the time delay between the j^{th} element and the central element, $\Delta\tau_j$ is given by [135]:

$$\Delta\tau_j = \frac{r_j - r_0}{c}, \tag{2.63}$$

where r_j is the distance between the desired focal point and the j^{th} element, r_0 is the distance between the focal point and the central element. These delay laws can be trivially extended to three dimensions, if a two-dimensional array is being used [138]. By focusing the energy in this way, the lateral resolution of the measurements is increased, due to the decrease in the effective beam width. Also, as there is now more ultrasonic energy focused into a smaller volume, the sensitivity is also increased, meaning improved signal to noise ratios and the ability to detect smaller defects.

However, there are limitations to the steering and focusing capabilities of an array, and these must be considered in the design. Ideally, an ultrasonic array would consist of an infinite number of infinitesimal elements. However, as this is not possible, the effect that a limited number of finitely sized elements would have on the generated wavefield must be considered. The size and number of the elements, as well as the overall size of the array, will all affect the ultrasonic beam, and place limits of the ability of the array to manipulate the beam.

The finite size of the array elements will have an effect on the generated beam as the shape of the element changes the way in which the energy is emitted. For an ideal

infinitesimal point source, the element is capable of emitting energy equally over all angles. However an element of finite size can no longer emit waves omnidirectionally. The angular distribution of the wavefield generated by a single element is called its directivity function. For an omnidirectional point emitter, the directivity function is equal to unity for all angles, as it emits waves of equal intensity at all angles. However, for a finite sized element, the directivity function is modified, according to the shape of the element, as is shown in figure 2.11 for a strip source aperture. The directivity function can be calculated by integrating a series of point sources over the area covering the array element. In the far-field, due to the application of the Fraunhofer diffraction equation [39, 145], this reduces to the spatial Fourier transform of the shape of the element [147–149]. Due to the simplicity and symmetry associated with rectangular elements, the directivity function for a single wave mode, $D(\theta)$ can be calculated analytically:

$$\begin{aligned} D(\omega,\, \theta) &= \int_{-\infty}^{\infty} \mathrm{Rect}(a)\, e^{-ikx}\, \mathrm{d}x \\ &= \frac{1}{a} \int_{-\frac{a}{2}}^{\frac{a}{2}} e^{-ikx}\, \mathrm{d}x \\ &= \mathrm{sinc}\left(\frac{ka}{2}\right) = \mathrm{sinc}\left(\frac{\pi a \sin\theta}{\lambda(\omega)}\right). \end{aligned} \tag{2.64}$$

From equation 2.64, the directivity of a rectangular element is dependent on the width of the element, a, relative to the wavelength, λ, of the ultrasound that is being generated. It must be emphasised that equation 2.64 is only true if the element is generating a single wave mode. For multiple wave modes (for instance, if the element generates longitudinal, shear and surface waves), the partition of the energy of these different wave modes must be considered [150]. However, for a single wave mode, the change in directivity as the size of the element grows relative to the size of the wavelength can be seen in figure 2.12. So, if the element is much smaller than the wavelength of the generated wave, then it can be approximated as an omnidirectional

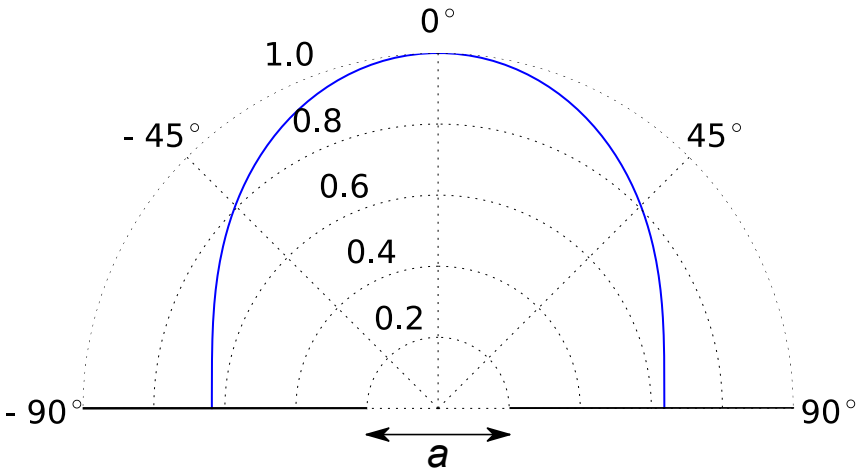

Figure 2.11: The angular intensity of the radiated field from an element of size a, which is emitting a wave with a wavelength $\lambda = \frac{a}{2}$.

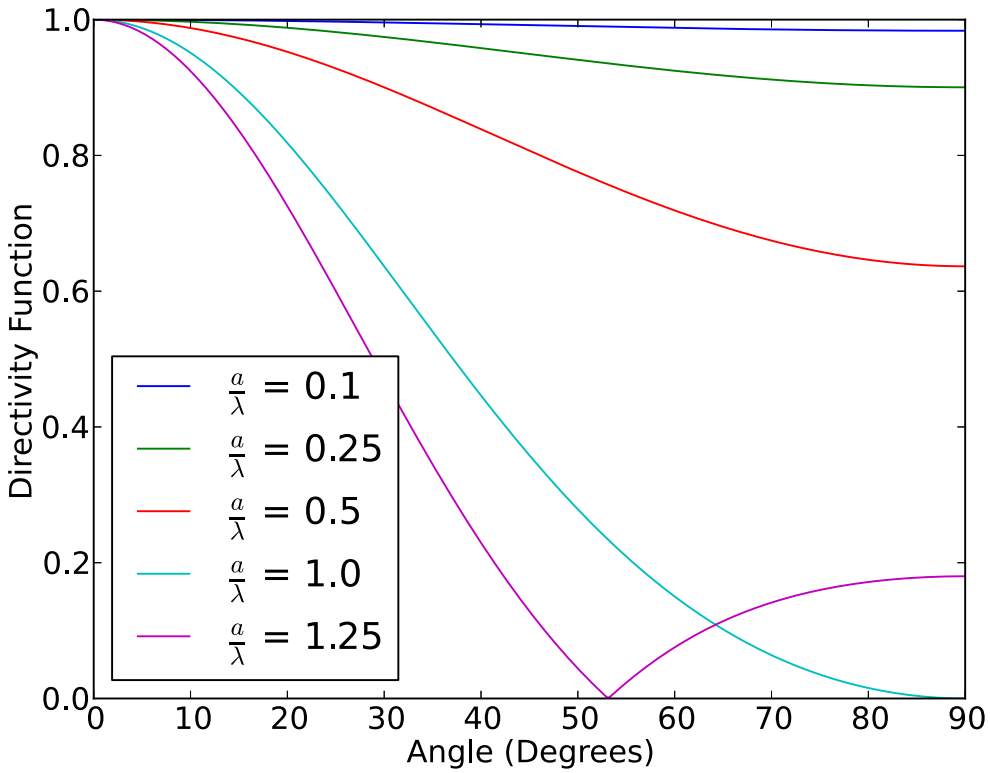

Figure 2.12: Variation of directivity of an array element as the size, a, relative to the emitted wavelength, λ, changes. If the size of the element is small in comparison to the wavelength, it will act as an omnidirectional source. However, as the size of the element increased, the emitted energy becomes more directional, being concentrated towards $\theta = 0°$.

source. However, as the size of the element becomes comparable with the size of the wavelength, the directionality of the emitter becomes more pronounced, with the energy being more concentrated towards $\theta = 0°$. When the size of the element exceeds the size of the wavelength that is being generated, minima will appear in the directivity function. These zeros will occur when the size of the element is an integer number of wavelengths. When the size of the element aperture becomes larger than the wavelength of the generated ultrasound, side lobes are formed. Side lobes consist of multiple low-intensity beams located outside of the main ultrasonic beam [151]. These side-lobes can be sufficiently intense to cause spurious indications, as the imaging algorithms assume the presence of a single ultrasonic beam. Another consequence of the directivity of elements is the limited beam steering capabilities. As the array element gets larger, the generated beam becomes more directional. Consequently, the ability to steer and focus the ultrasound at large angles is reduced, due to the limited ultrasonic energy that can be produced at these angles [1, 152].

Another key parameter in array design is the spacing between the elements. If the inter-element spacing is not carefully considered, then the array could support grating lobes, which will give rise to extra lobes that can be of equal magnitude to the main beam [1, 135, 152]. Due to the regular, periodic spacing of array elements, there will be constructive interference when waves from neighbouring elements are separated by an integer number of wavelengths. At this point, the array acts like a diffraction grating, with a grating lobe being generated at an angle θ_G [131]:

$$kd \sin \theta_G = n\pi. \tag{2.65}$$

Here, d is the inter-element spacing of the array, n is an integer and $k = {}^{2\pi}/_{\lambda}$ is the wavenumber of the generated ultrasound. These grating lobes are a result of spatial under-sampling of the array, and can be eliminated if the spacing of the elements is less than ${}^{\lambda}/_{2}$ [131, 136]. As ultrasonic arrays are generally excited with pulses, rather than continuous waves (CW), this condition can be relaxed slightly and the

grating lobe amplitudes are less than would be expected in the CW case [1, 136]. Grating lobes can also be suppressed by redistributing the array elements in a sparse aperiodic patterns [153, 154], by relying on short pulses [135, 136], or by using a staggered, overlapping element array pattern [149].

2.3.3.1 Full Matrix Capture and Total Focusing Method

The imaging algorithms and beam manipulations described above show how a physical wavefront can be created by electronically controlling the delay in the firing of individual elements. However, similar to the way in which SAFT can synthetically create an aperture, many phased array techniques can be post-processed. Post-processing works by acquiring and storing the relevant ultrasonic data before later digitally processing this data as required. If the array is excited so that all the possible send-receive combinations are obtained, by performing a so-called Full Matrix Capture (FMC), then all possible imaging techniques can be digitally applied at will [1,140,155]. If the array controller can receive data in parallel thn, despite having to capture every send-receive possibility, the data can be obtained in a similar time to a swept aperture B-scan measurement [140]. However, FMC does suffer from a degradation of SNR as the ultrasonic power is limited by the use of a single element, rather than multi-element aperture, excitation [1, 140]. Nevertheless, this is mitigated by the averaging effects of the imaging algorithms that are applied to the data [140].

A full matrix of time domain signals gives the maximum information that is possible to obtain from an ultrasonic array. Consequently, all possible ultrasonic array inspections form a subset of the FMC data, as shown in figure 2.13. Some of the possible post-processing algorithms are discussed below, showing their implementation and imaging results. The complex analytic signal is generally used for imaging purposes, as the phase information included improves the image resolution [156]. The analytic signal, $h(t)$, is obtained from the real experimental signal, $s(t)$, by

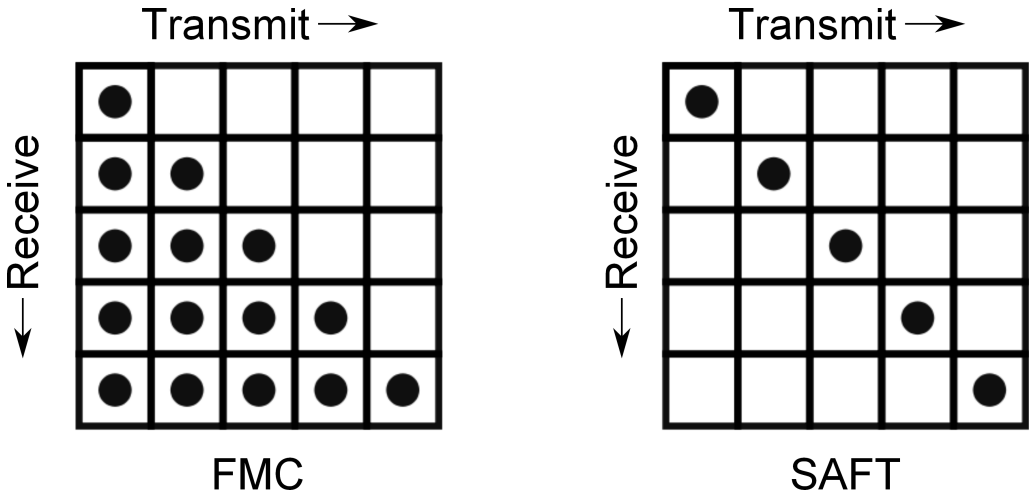

Figure 2.13: Transmit-receive data matrices, showing the data obtained, for full matrix capture (FMC) and the synthetic aperture focusing technique (SAFT). Due to reciprocity, $s_{i,j}(t) = s_{j,i}(t)$ and so only half of the matrix of data is required.

applying the Hilbert transform, which applies a 90° phase shift to the experimental signal. Hence the analytic signal can be formed by the quadrature sum of the original signal and its Hilbert transform. The envelope of the signal can be obtained by taking the complex magnitude of the analytic signal, and it is this that is presented in ultrasonic images.

The rise in FMC is accompanied by the use of the total focusing method (TFM) imaging algorithm. TFM acts to focus the beam at every point within the region of interest, utilising the ultrasonic data from each send-receive pair [126, 140, 157]. The region of interest is discretised into a grid of pixels, with the extent of this grid limited only by the maximum travel time present in the obtained A-scans. The data are then focused at every point, by applying the appropriate time delay to the analytic signal, with the intensity of the image, $I(x, y)$ at any point being:

$$I(x,y) = \left| \sum_i \sum_j h_{i,j} \left(\frac{\sqrt{(x_i - x)^2 + y^2} + \sqrt{(x_j - x)^2 + y^2}}{c} \right) \right|. \tag{2.66}$$

Here, $h_{i,j}$ refers to the analytic signal that is excited by element i and received by element j, c is the speed of the ultrasonic wave, with x_i and x_j the position of the transmit and receive elements, respectively. A simulated TFM image is compared

with a SAFT image, which can be formed by ensuring that $j = i$, in figure 2.14. From both algorithms, it can be seen that the scatterer has been localised in the correct position. However, the point-spread function for SAFT image is smaller than in the TFM image, meaning that SAFT can better localise a defect [124]. However, it should be noticed that the TFM image has much lower side lobe amplitudes. Also, as TFM utilises the full matrix of data, it has a greater averaging effect than SAFT and hence is more resistant to image degradation from random noise [124]. In addition, the imaging noise floor is much lower for TFM than SAFT, due to the increased amount of data used to form the image [124]. The main disadvantage of TFM - the computation time [157] - is being diminished due to improvements in computational time and parallelisation using graphics processing units [158].

2.4 Conclusions

This chapter has discussed some of the underlying physical principles that underpin the work performed here. It outlines how ultrasonic disturbances can propagate in elastic media, and exist with various polarisations. In a infinite isotropic and homogeneous medium, three independent wave modes exist in the form of a longitudinal wave and two transverse shear waves. A multitude of other ultrasonic modes are also supported in media of finite extent, with their propagation behaviour depending upon the dimensions of the sample as well as the material properties that determine bulk wave speeds. With knowledge of the speeds of these modes, and how they interact with discontinuities in the propagation medium, ultrasonic waves can be used as powerful probes to investigate and non-destructively test a material. Most ultrasonic non-destructive testing methods are based upon the time of flight of an ultrasonic pulse between transducer and a discontinuity.

More advanced techniques, whilst still relying on time of flight measurements, can improve the resolution of the localisation of the defect, and even lead to the

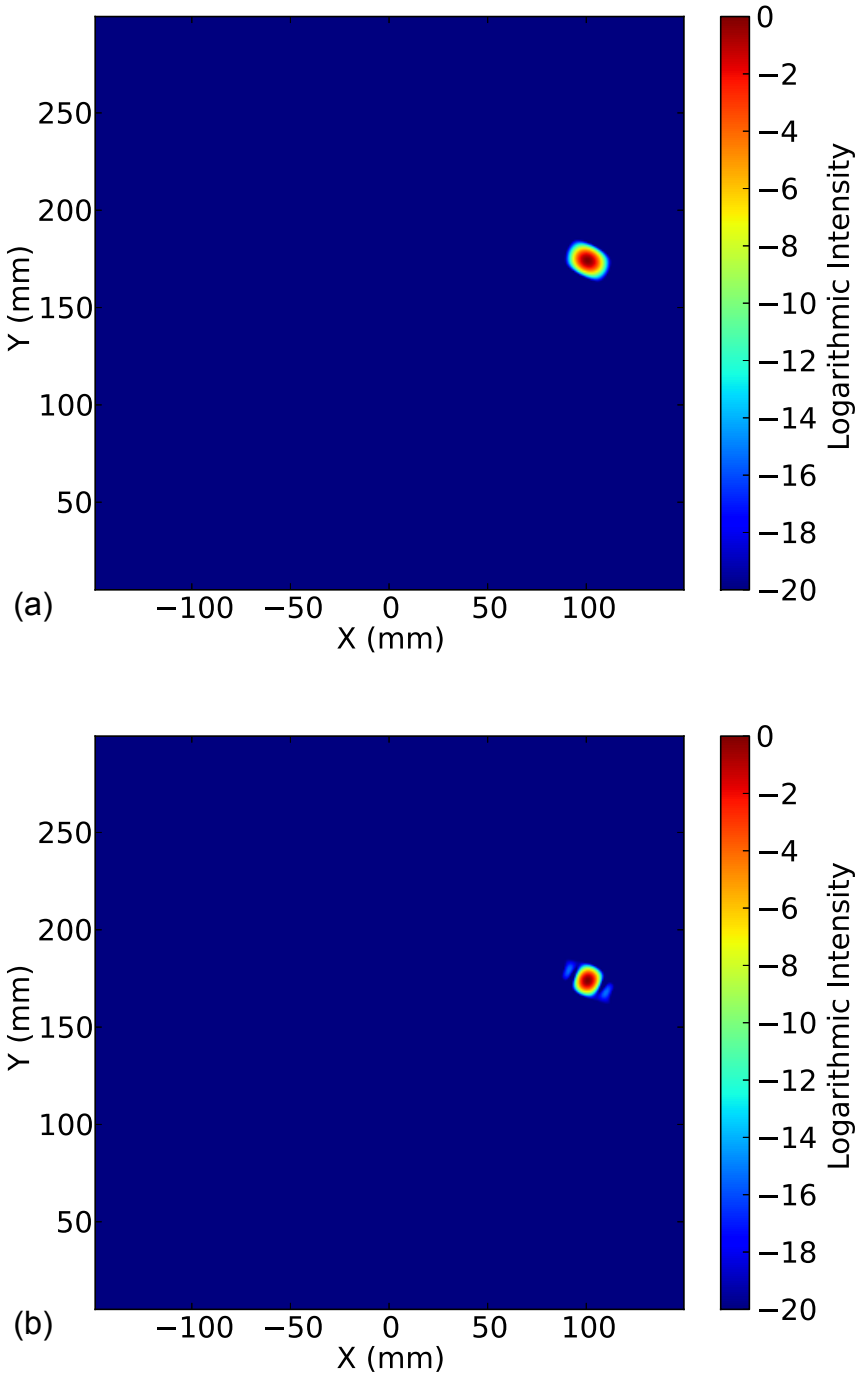

Figure 2.14: Outputs of post-processed TFM image (a) and SAFT image (b) using simulated data. The simulated array, which consists of 32 elements that are spaced by 5 mm, generates longitudinal waves in aluminium with a speed of 6306 ms^{-1}, and is centred on the position $(0, 0)$. The array is excited with a Hann windowed, four cycle tone-burst signal with a frequency of 600 kHz. The point-like defect is at an angle of 30° and a distance of 200 mm relative to the centre of the array.

ability of imaging an inspection area. For example, SAFT simulates a larger aperture transducer by scanning a single transducer whilst obtaining pulse-echo data. Delay-and-sum algorithms can then be applied to this data in order to form the synthetic aperture. By synthetically creating a larger aperture in this way, the SAFT algorithm leads to improved spatial resolution when compared to a single pulse echo measurement, as well as the ability to locate and image a defect. As computer processing power, manufacturing practices and electronic processing improved, the complexity of ultrasonic testing has also increased, along with the versatility of the inspections. This has led to the regular use of phased array technology and subsequent research interest in full matrix capture and the total focusing method. Phased arrays can control, steer and focus the ultrasonic beam, which improves the spatial resolution and signal to noise ratio of measurements, as well as making ultrasonic inspection a more flexible tool.

However, these advantages come at a cost. In order to independently control the elements in the array, complex high-speed electronics are required along with significant computing power; both adding considerable complexity to the operation. Hence, it is desirable to have an array that is capable of retaining the beam-steering capabilities, while avoiding the inherent complexities of phased arrays. This is shown in Chapter 3, where the spatial periodicity of an ultrasonic array is utilised to steer the ultrasonic beam by simply varying the excitation frequency.

Chapter 3

Frequency Steered Arrays

Phased array techniques, described in section 2.3.3, have made it possible to physically control an ultrasonic beam by adjusting the time delay between the excitation of different elements by an appropriate amount. The ability to steer and focus the beam leads to an increase in the sensitivity of measurements, due to an enhancement in the signal to noise ratio, as well as an improvement in the resolution of the localisation of the defect. However, the requirement to individually control every element in the array necessarily leads to significant hardware and software complexity. Consequently, it is desirable to have a system that retains the beam-steering capabilities of phased arrays, whilst significantly reducing the levels of complexity.

This is achieved with frequency steered arrays, which utilise the periodic structure of an array to generate a frequency dependent angle of propagation. The advantage of frequency steered arrays is that all of the elements are excited simultaneously, removing the complexities that are associated with phased arrays. Beam steering can be achieved due to the spatial periodicity of the array, with the elements laid out in a regular arrangement that possesses a natural spatial frequency. When the array is excited with a narrowband tone-burst signal, the individual waves from each element in the array interfere with each other, leading to constructive interference at a particular angle. This interference effect generates a wave that has

a frequency dependent angle of propagation, with the direct relationship between frequency and angle dependent upon the physical layout of the array. For a fixed array structure, the condition for constructive interference changes with frequency, and the angle at which the ultrasound is steered to can be adjusted by simply varying the tone-burst frequency. This principle has been demonstrated for both two-dimensional [159–162] and linear ultrasonic arrays [69, 93, 98, 101].

In section 2.2.1.1, it was seen how the periodic structure of the PPM EMATs, with regular elements of alternating polarity, can be used to generate SH waves on the surface. The alternating polarity of the magnets leads to a similar force distribution of the surface of the sample; the periodicity of this distribution defines the wavelength of SH waves along the surface. This spatial periodicity can also be used to generate a steered SH beam that propagates at an angle to the sample surface, as described by equation 2.50. This condition for constructive interference, when the path length difference between waves from two neighbouring elements of the same polarity is equal to an integer number of wavelengths, clearly changes with frequency, and so the ultrasonic beam can clearly be steered by simply changing the frequency of the tone-burst signal [38]. In this sense, the PPM EMAT can be compared to a diffraction grating, but with an alternating polarity configuration. Hence, it is possible to steer the ultrasonic beam from $\theta = 90°$, which corresponds to the surface up to an angle where the higher order diffraction modes are activated. Due to the alternating polarity structure of the PPM EMAT, this occurs when $\lambda = {}^{d}/_{3}$, meaning that the beam can be steered in the range $20° \leq \theta \leq 90°$ [101,102].

3.1 Ewald Sphere Construction

However, whilst this modelling approach can be used to predict the relationship between frequency and the peak position of the ultrasonic beam, it says nothing about the width or shape of the beam. These parameters can be equally important,

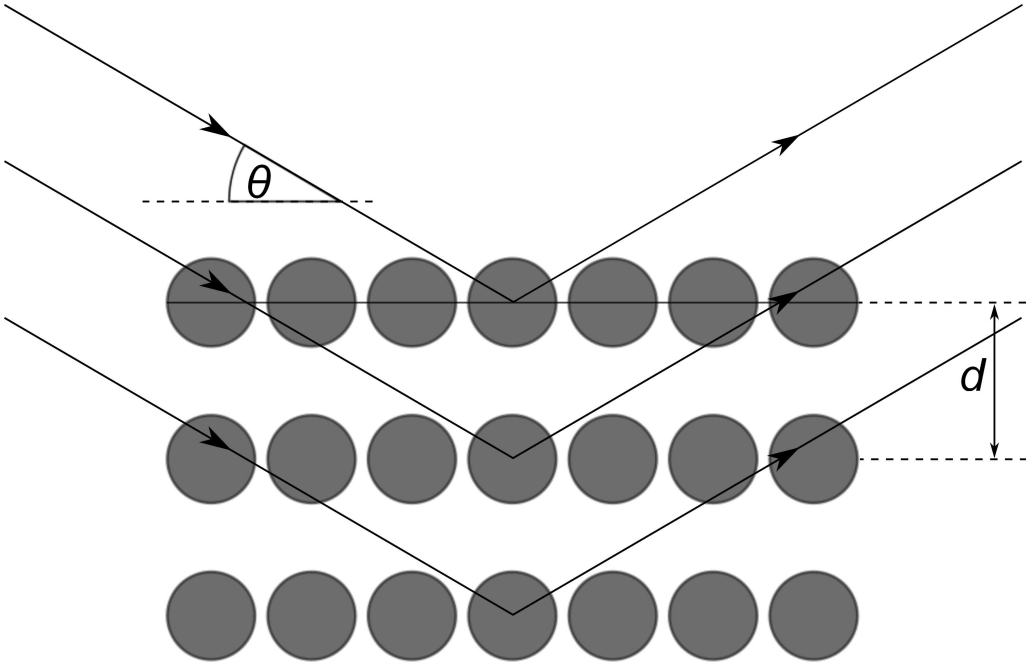

Figure 3.1: An example crystallographic structure, showing a periodic arrangement of atomic planes, separated by a distance, *d*. The incident X-rays are scattered by these atomic planes, and constructively interfere at an angle θ.

and hence the whole directivity of the array should be modelled. Due to the spatial periodicity of arrays required for this frequency steering approach, this modelling is best performed in the spatial frequency domain. This can be done by taking inspiration from diffraction physics, specifically from the Ewald sphere construction for diffraction phenomena, for instance, X-ray diffraction of a crystal [163]. The structure of a crystal is extremely ordered, formed by the repeating atomic structure of the crystal's unit cell [164], meaning that crystallographic structure also possesses spatial periodicity, in a similar way to the regular arrangement of elements in an array. If X-rays are incident on the crystal, schematically shown in figure 3.1, then they will be scattered by the crystallographic planes. The X-rays, after being scattered from successive planes, will constructively interfere at a particular angle when the path length difference is a integer number of wavelengths [164]:

$$n\lambda = 2d\sin\theta. \tag{3.1}$$

This is called Bragg's law, and similarities can be seen between this and equation 2.50, due to the same physical mechanisms underlying both phenomena. However, this relation can be more easily seen by inspecting the reciprocal lattice, which shows the crystallographic structure in the spatial frequency domain, as shown in figure 3.2. The lattice is transformed from real space into wavenumber, or momentum, space by the application of a spatial Fourier transform [165]. The reciprocal lattice shows the underlying spatial frequencies associated with the structure, and how the lattice is orientated. An incident X-ray beam, of energy E, will have a wavenumber that is given by the relation $k = \frac{E}{\hbar c}$, which is travelling in a particular direction, as described by its wavevector, $\mathbf{k_i}$. The X-ray beam will then be elastically scattered in any direction, which changes the wavevector to a value $\mathbf{k_f}$. However, as the X-rays are elastically scattered, the energy, and therefore the wavenumber, of the beam remains constant. This means that all the possible scattering directions lie on the surface of a sphere, termed the Ewald sphere or sphere of reflections [164]. For a two-dimensional structure, the sphere of reflection is reduced to a circle, with all the possible scattering positions lying on the the circumference of the Ewald circle. However, X-ray diffraction can only occur when the Ewald sphere intersects a point of the reciprocal lattice, which is equivalent to Bragg's law reformulated in $\mathbf{k}-$space. This idea is shown graphically in figure 3.3, and explains how constructive interference occurs when the energy and orientation of the X-ray beam complements the spatial periodicity of the lattice, as detailed by the Laue Equations:

$$\mathbf{k_f} - \mathbf{k_i} = \sigma_{\mathbf{ijk}} = \frac{2\pi}{\mathbf{d_{ijk}}}. \tag{3.2}$$

Here, $\mathbf{d_{ijk}}$ is a vector that indicates a periodic crystallographic plane from which the X-rays can diffract. From figure 3.3 and geometry, it can be seen that Bragg's law can be recovered from the Ewald construction:

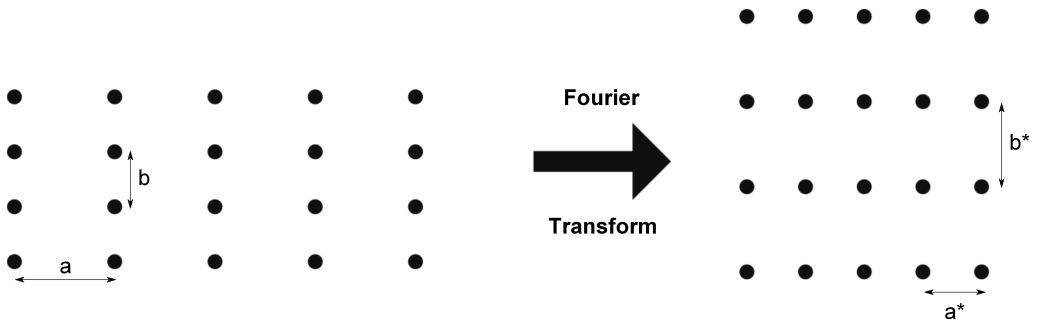

Figure 3.2: The reciprocal lattice can be found from the real-space arrangement of atoms by applying a Fourier transform. Consequently, the spacing of the reciprocal unit cell are given by $a^* = \frac{2\pi}{a}$ and $b^* = \frac{2\pi}{b}$.

$$|\sigma_{\mathbf{ijk}}| = \frac{2\pi}{|\mathbf{d_{ijk}}|} = 2k \sin\theta. \tag{3.3}$$

The Ewald construction can be used to predict the occurrence of diffraction peaks, and at what angle and frequency they will occur; making it a valuable tool for interpreting X-ray diffraction data. The similarities between a periodic array and a crystallographic structure means that this model can be adapted in order to predict the frequency dependent directivity of ultrasonic arrays [101].

3.2 Frequency Domain Directivity Modelling

The directivity of a periodic array can be calculated by considering the displacement field, $\mathbf{u}(\mathbf{x}, \omega)$, generated by the applied load distribution of the array elements, which can be described by the function, $\mathbf{f}(\mathbf{x}, \omega)$. This can be described by investigating the elastodynamic behaviour of the medium [162]:

$$\mu\left(\nabla^2 \mathbf{u}(\mathbf{x},\, \omega) + \mathbf{f}(\mathbf{x},\, \omega)\right) = \rho \ddot{\mathbf{u}}(\mathbf{x},\, \omega). \tag{3.4}$$

This can be re-written, in terms of differential operators, as [159, 161]:

$$\mathcal{D}[u(\mathbf{x},\, \omega)] = f(\mathbf{x}, \omega). \tag{3.5}$$

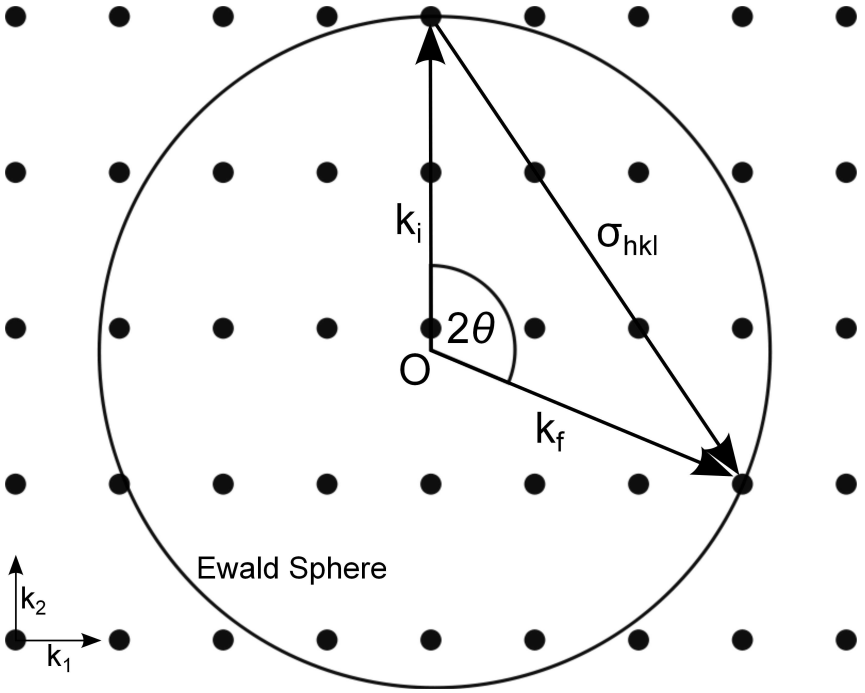

Figure 3.3: The Ewald sphere construction, showing the reciprocal lattice and the Ewald sphere of reflection. The X-rays are diffracted by the (hkl) plane at an angle θ due the Ewald sphere intersecting a pair of reciprocal lattice points, which corresponds to the X-ray beam satisfying the constructive interference condition for the (hkl) plane. The centre of the Ewald sphere is denoted by O.

Here, $\mathcal{D}$ is a linear differential operator that defines the medium considered, and how the ultrasonic disturbance will propagate. As was seen with the Ewald sphere construction, a periodic structure is best examined in the spatial frequency domain through the application of a Fourier transform. By applying this transformation, the partial differential equation can be changed into an algebraic expression [33]:

$$\tilde{D}\left(\mathbf{k},\,\omega\right)U\left(\mathbf{k},\,\omega\right)=F\left(\mathbf{k},\,\omega\right). \tag{3.6}$$

This converts the various functions from the spatial domain, which rely on the co-ordinate vector $\mathbf{x}$, into the spatial frequency domain, denoted by the wavevector co-ordinate vector, $\mathbf{k}$. Equation 3.6 can be re-arranged in terms of the displacement field:

$$U\left(\mathbf{k},\,\omega\right)=\tilde{D}^{-1}\left(\mathbf{k},\,\omega\right)F\left(\mathbf{k},\,\omega\right). \tag{3.7}$$

Equation 3.7 can be interpreted as showing that the Fourier domain displacement is dependent upon both the load distribution, $F\left(\mathbf{k},\,\omega\right)$, and the medium characteristics, defined by $\tilde{D}^{-1}\left(\mathbf{k},\,\omega\right)$. With reference to the Ewald construction, $F\left(\mathbf{k},\,\omega\right)$ is analogous to the reciprocal lattice, whilst $\tilde{D}^{-1}\left(\mathbf{k},\,\omega\right)$ corresponds to the Ewald sphere of X-ray energy. From equation 3.7, it is clear that the greatest displacement amplitudes are achieved when both $\tilde{D}^{-1}\left(\mathbf{k},\,\omega\right)$ and $F\left(\mathbf{k},\,\omega\right)$ are maximised. The maxima of $F\left(\mathbf{k},\,\omega\right)$ are ascertained from the periodic load distribution, corresponding to a peak in the reciprocal lattice arrangement of the array [101]. The second condition is clearly met when $\tilde{D}\left(\mathbf{k},\,\omega\right)=0$, which is equivalent to satisfying the dispersion relation [159–162]. So, the largest amplitude is achieved when the dispersion relation intersects a maximum in the load distribution. This is analogous to the Ewald construction, where diffraction occurs when the Ewald sphere crosses a point in the reciprocal lattice.

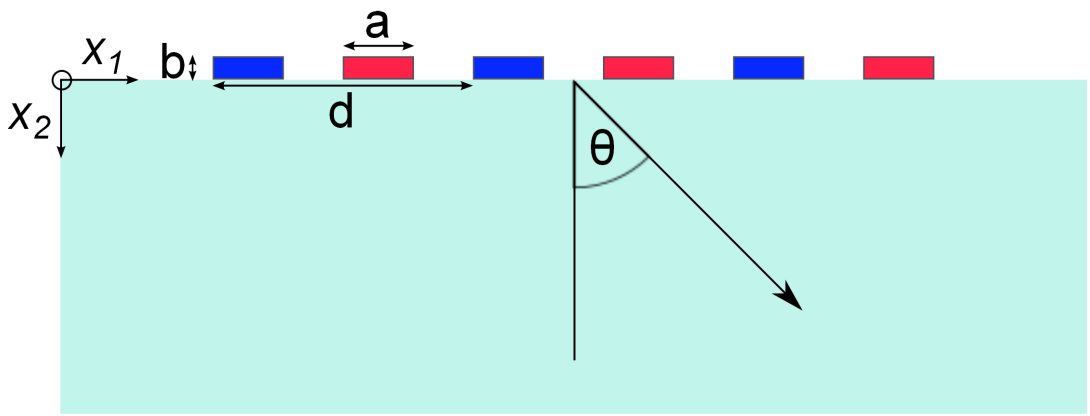

Figure 3.4: The periodic geometry of the PPM EMAT, showing the alternating polarity of the elements, as well as the length, a, and depth, b, of the array elements, as well as the periodic distance of the array, d.

3.2.1 Reciprocal Lattice of PPM EMAT

It has been seen how the frequency dependence of the directivity of the array can be established by finding an expression that encapsulates the generated force distribution, and then Fourier transforming it into the reciprocal $\mathbf{k}-$space domain. Hence, in order to calculate the directivity of a PPM EMAT, such an expression must be found. As the length of the PPM array elements is much larger than either the width, a, or the depth, b, the problem can be reduced to two dimensions. Hence, by modelling the load distribution as a linear array of N sources of alternating polarity, as shown in figure 3.4, the expression is given by:

$$f\left(\mathbf{x},\, \omega\right) = f_0\left(\omega\right) p\left(x_1,\, x_2\right) \circledast \sum_{n=0}^{N-1} \left(-1\right)^n \delta_2 \left(x_1 - \frac{nd}{2},\, x_2\right), \tag{3.8}$$

where $f_0\left(\omega\right)$ represents the frequency content of the drive signal, d is the periodic distance of the array (equal to twice the pitch), $\delta_2\left(x_1 - \frac{nd}{2},\, x_2\right)$ is the two dimensional Dirac delta function representing the centre of the n^{th} array element, $p\left(x_1,\, x_2\right)$ is the spatial impulse response that describes the shearing force generated the elements of the array, and $\circledast$ represents the convolution operation. The reciprocal lattice can be calculated by applying a two-dimensional Fourier transform to convert the co-ordinates $\mathbf{x}$ into wavenumber $\mathbf{k}-$space, leading to:

$$F\left(\mathbf{k},\,\omega\right) = f_0\left(\omega\right) P\left(k_1,\,k_2\right) \sum_{n=0}^{N-1} \left(-1\right)^n e^{\frac{ink_1 d}{2}}, \tag{3.9}$$

where $P\left(k_1,\,k_2\right)$ is the array element impulse response in the Fourier domain. The PPM array elements can be described as a rectangular function, as shown in figure 3.4, meaning their impulse response, in the far-field, can be calculated.

$$\begin{aligned} P\left(k_1,\,k_2\right) &= \int_{-\infty}^{\infty}\int_{-\infty}^{\infty} \text{Rect}\left(a\right) e^{-ik_1x_1}\,\text{Rect}\left(\text{b}\right)e^{-ik_2x_2}\,\text{d}x_1\,\text{d}x_2 \\ &= \frac{1}{ab}\int_{-\frac{b}{2}}^{\frac{b}{2}}\int_{-\frac{a}{2}}^{\frac{a}{2}} e^{-ik_1x_1}e^{-ik_2x_2}\,\text{d}x_1\,\text{d}x_2 \\ &= \text{sinc}\left(\frac{k_1a}{2}\right)\text{sinc}\left(\frac{k_2b}{2}\right). \end{aligned} \tag{3.10}$$

However, the thickness of the force distribution, along the x_2-direction, will be limited by the electromagnetic skin depth [17]. Consequently, b is very small and hence $\text{sinc}\left(\frac{k_2b}{2}\right) \approx 1$, meaning that this term can be neglected in most cases. Hence, the force load distribution is given by [101]:

$$F\left(\mathbf{k},\,\omega\right) = f_0\left(\omega\right)\text{sinc}\left(\frac{k_1a}{2}\right)\sum_{n=0}^{N-1}\left(-1\right)^n e^{\frac{ink_1d}{2}}. \tag{3.11}$$

This expression can be used to investigate the reciprocal lattice of a PPM EMAT, which is plotted in figure 3.5. The array modelled in figure 3.5 is a six element array consisting of 4 mm wide elements, with a pitch of 5 mm. Unlike the atomic structure for crystals, which are periodic in three dimensions, the array only repeats along the x_1-axis. Consequently, the reciprocal lattice shows lines of constant intensity along the k_2-axis, with the lattice only varying along k_1-axis. There are two diffraction 'rods', which can be seen at ± 628 m^{-1}, corresponding to the fundamental spatial frequency of the 5 mm pitch array. In addition, due to fact that the reciprocal lattice is symmetric about $k_1 = 0$, it can be seen that two equal *magnitude* beams will be travelling off in opposite directions, $\pm\theta$. However, the array is anti-symmetric

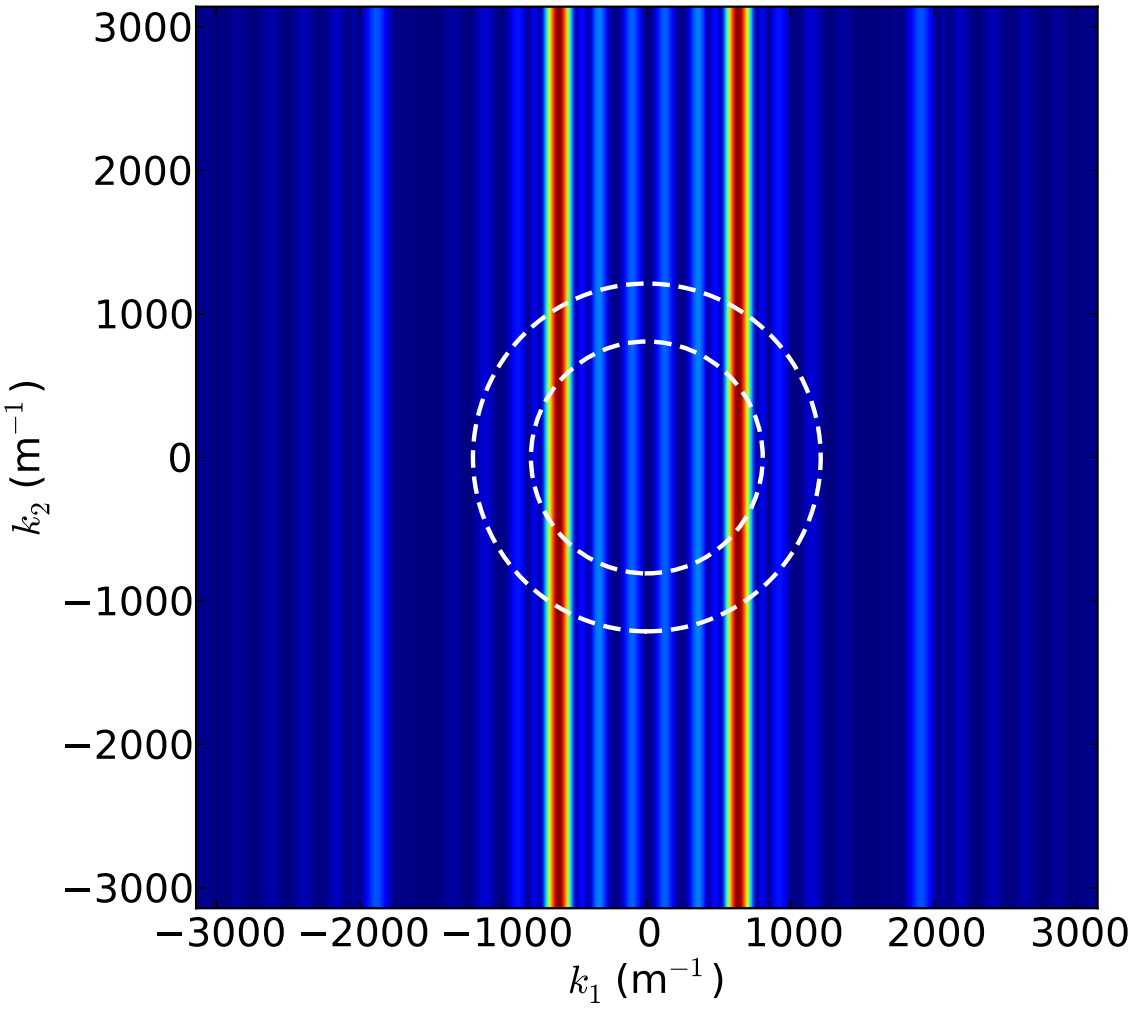

Figure 3.5: The force load distribution of a six element, 5 mm pitch PPM EMAT array, shown in the frequency domain. The circles represent the dispersion relations of two bulk shear waves propagating in aluminium ($v_s = 3111$ ms^{-1}). The smaller radius circle represents a 400 kHz shear wave, whilst the larger radius circle represents the dispersion relation for a 600 kHz shear wave.

about its centre as it contains an even number of elements. Hence, by symmetry, the generated wavefronts will also be anti-symmetric and the beams, whilst having equal magnitudes, will have a 180° phase shift relative to each other. By considering this phase shift and using a separate transducer to detect the wavefront, it is possible to determine whether the wave was launched in the $+\theta$ or the $-\theta$ direction.

It should also noted that, due to the alternating polarity of the array, the second order diffraction terms have been eliminated from the reciprocal lattice, although third order diffraction bands can be seen at ± 1885 m^{-1}. These third order diffrac-

tion rods are much lower in intensity than the first order rods, due to the frequency dependence of the element impulse response. The directivity of an individual element, encapsulated in the $P(k_1,\ k_2) = \mathrm{sinc}\,(k_1 a/2)$ term, allows lower frequencies to be transmitted at a greater efficiency than higher frequencies. Consequently, the higher order diffraction modes are suppressed, relative to the first order diffraction terms. There are also a number of 'side lobes' around the main diffraction rods, and these are a consequence of the limited number of elements in the array. As there are only six elements in the array, the interference could not build up to a sufficient level to eliminate them completely. An increased number of elements would act to reduce the side lobe levels, as well as sharpen up the main diffraction beams [39,101], although this would increase the length of the signal in the temporal domain, as a consequence of time-frequency duality.

In addition to the reciprocal lattice of the array, an expression for the dispersion relation of the ultrasonic signal used to excite the array must be found. This will depend upon the material into which the array is operating, and special consideration must be paid to the relevant dispersion curves. However, for bulk waves in an isotropic medium, the dispersion relation is given by:

$$\tilde{D}\,(\mathbf{k},\ \omega) = k_1^2 + k_2^2 - \left(\frac{\omega}{c}\right)^2 = 0. \tag{3.12}$$

This means that, in 2D $\mathbf{k}-$space, the dispersion relation reduces to a circle, with a radius, k_T:

$$k_T = \sqrt{k_1^2 + k_2^2} = \frac{\omega}{c}. \tag{3.13}$$

Whilst it is not strictly isotropic, aluminium can be considered to be macroscopically isotropic with variations in shear speed of typically less than a few percent [166, 167]. Anisotropy can be easily handled by this model, provided that the dispersion relation can be calculated and parametrised [159]. The dispersion relation

for shear waves in aluminium of two different frequencies, 400 kHz and 600 kHz, is shown in figure 3.5. From equation 3.7, the maximum displacement amplitudes are achieved when both the dispersion relation and the reciprocal force distribution are maximised. Graphically, it can be seen when this condition is met as it corresponds to the locations where the dispersion relation overlaps the bands of strong intensity of the reciprocal lattice. As this happens within confined regions of $\mathbf{k}-$space, the ultrasonic beam is steered to a particular angle, $\theta = \arctan\left(\frac{k_1}{k_2}\right)$. The total directivity of the array being driven at a particular frequency can be calculated from equation 3.11. For a given drive frequency $\omega = k_T c$, then $k_1 = k_T \sin\theta$ and so equation 3.11 gives the directivity function $d(\theta,\, \omega)$:

$$d(\theta,\, \omega) = f_0(\omega)\,\mathrm{sinc}\left(\frac{\omega a \sin\theta}{2c}\right)\sum_{n=0}^{N-1}(-1)^n\, e^{in\omega d\sin\theta/2c}. \tag{3.14}$$

However, a real signal will not contain a single frequency, ω, but a range of frequencies. If the frequency spectrum of the excitation signal is given by $S(\omega)$, then the directivity of the array driven by such a signal is:

$$d(\theta) = \int_0^\infty S(\omega)\,\mathrm{sinc}\left(\frac{\omega a \sin\theta}{2c}\right)\sum_{n=0}^{N-1}(-1)^n\, e^{in\omega d\sin\theta/2c}\,\mathrm{d}\omega. \tag{3.15}$$

Equation 3.15 can be used to numerically calculate the directivity by truncating the integral to an appropriate, finite limit. Example directivities in figure 3.6 show how the beam is steered by simply changing the input frequency. A clear shift in the peak position of the main beam can be seen, with the steering angle changing by simply varying the frequency of the excitation signal. It is also clear that the beam is brought into tighter focus at the lower angles, which is achieved by activating the array with a higher frequency signal. This is due to the inverse proportionality between frequency and angle, that can be seen from the diffraction grating equation; the angular spread is much smaller, for a given bandwidth, at the higher frequencies than the lower frequency values.

The driving signal obviously also has an effect on the beam width obtained by frequency steering. If the array is driven with a narrow bandwidth signal, the ultrasonic energy will be steered over a very narrow range of angles as there are only few frequencies present, and so there is only a limited range of angle over which the signal can constructively interfere. However, a narrow bandwidth signal necessarily implies that it will have a large temporal range, hence leading to poor axial resolution. Conversely, a temporally well-defined pulse, whilst having good axial resolution, will contain a range of frequencies and therefore have poor beam steering capabilities. Therefore, there is an explicit compromise between angular and axial resolution caused by time-frequency duality; increased angular resolution directly causes a reduction in the axial resolution that could be achieved, and vice versa.

3.3 Conclusion

Ultrasonic beam manipulation and steering can be achieved by carefully controlling the frequency content of the generation signal used to simultaneously excite all the elements within the periodic array. The interference between the waves produced by each individual elements causes preferential propagation of ultrasound with a certain frequency along a particular angular path. The relationship between the angle of propagation and the excitation frequency is given by the diffraction grating equation, and occurs when the spatial periodicity of the array and the wavenumber of the excitation signal overlap in $\mathbf{k}-$space. This conjunction occurs when there is constructive interference of that signal at that particular angle, when the path length differences between elements of the same polarity are equal to an odd integer number of wavelengths. As this condition of constructive interference changes with frequency, ultrasonic beam steering and sector scans can be achieved by simply varying the frequency of the excitation signal. This eliminates the need to be able

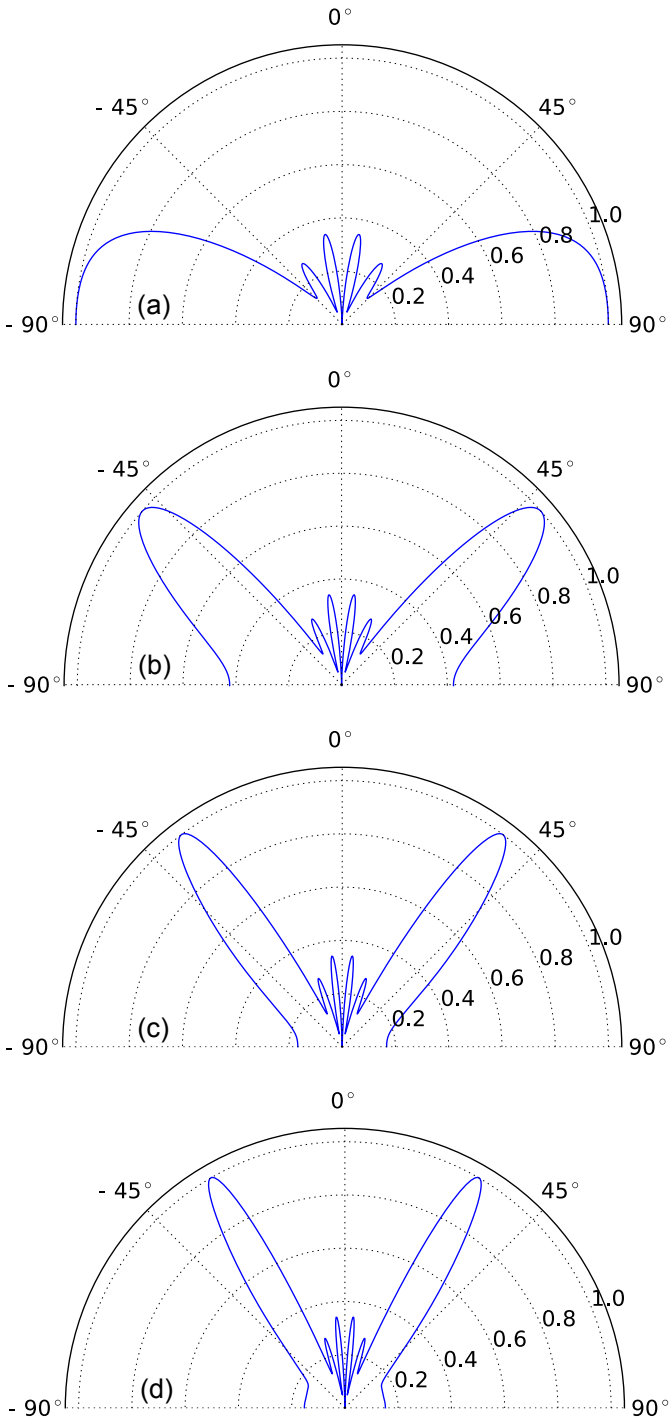

Figure 3.6: The directivity of a six element, 5 mm pitch array that generates SH waves in aluminium ($c_s = 3111\ \mathrm{ms}^{-1}$), which is being driven by a five cycle tone-burst signal with a frequency of (a) 300 kHz, (b) 400 kHz, (c) 500 kHz and (d) 600 kHz.

individually control and phase each array element, thereby avoiding the requirement for expensive hardware.

A frequency domain model, based upon the Ewald construction used in elementary diffraction modelling, was used to fully describe the frequency dependent directivity characteristics of the array. This model, unlike the diffraction grating equation, allows for the full directivity of the array to be calculated, not just the peak position of the ultrasonic beam. The model illustrates how the array's ability to strongly focus the ultrasonic beam changes with angle, with the beam being tightly focused for higher frequency excitations. The model is also very flexible, as it can trivially extended to two dimensional arrays and can handle known anisotropy in the velocity profiles of the generated wavefront [159, 168].

However, there is an inherent compromise between the axial and lateral resolution of frequency steered arrays, due to the principle of time-frequency duality. In addition, whilst a wide angular range ($20° \leq \theta \leq 90°$) can be scanned through this method, it requires a number of measurements, with the excitation frequency being swept through the appropriate range. The method, like the phased array methods described in section 2.3.3, can be relatively time consuming in acquiring the relevant ultrasonic data. A new approach, described in Chapter 4, shows how the periodicity of the array can be used to generate a wavefront that extends over the same angular extent. Consequently, the pulsed approach can inspect the same area as the frequency steered arrays, but only requires a single measurement. The pulsed wavefront also retains the frequency dependent directivity, which can again be utilised to locate any defects that may scatter this wavefront.

Chapter 4

Analytic Model of the Pulsed Array Wavefront

4.1 Overview

The physical principles of a new and alternative way to operate a linear array of wave emitters is described in this chapter. The method involves driving all of the elements simultaneously with a pulse that must have a carefully controlled frequency content. However, unlike the frequency steered arrays shown in Chapter 3, the excitation signal is designed to contain a large range of frequencies. If the bandwidth of the generation signal is correctly chosen, the subsequently generated wave has a number of interesting characteristics. Firstly, the wavefront extends in two dimensions over a large range of solid angles, meaning that it samples a large volume of the propagation media with a single excitation. However, perhaps more interestingly, the wavefront also exhibits a variation in frequency as the propagation direction is changed. This effective frequency change occurs monotonically over a large angular range, and is smooth and continuous in nature [102]. This smooth variation means that there is a unique transformation between wave frequency and angle of propagation. By measuring the local frequency of the wave, the angle of propaga-

tion, relative to the centre of the array, can be determined. As all of the elements are pulsed simultaneously with the same excitation signal, there is a reduction in the complexity of the hardware required to operate the array. This reduction in complexity is particularly noticeable when compared to the hardware required to control modern phased array systems.

In a two-dimensional measurement using a one-dimensional array, the frequency variation of the wavefront can be used to locate the position of a defect with a single measurement, whereas with other methods, the defect position can only be localised to a circle (or an ellipse, depending upon whether or not the transducers are co-located), or located after many measurements (Phased array methods [1, 124, 141]). If the wave, as it travels through the medium, is scattered by a discontinuity, the information from this wave is sufficient to localise the discontinuity that caused this signal. The radial distance between the discontinuity and the array can be calculated from the time of flight measurement of the wave. By measuring the frequency of the wave, the angle at which the wave was scattered can be determined. So, with a single wavefront, a large volume of the medium can be inspected, with the location of any discontinuities being determined by combining of the time of flight measurements and the frequency of the scattered wave.

However, in order to utilise the pulsed array to locate any discontinuities, a quantitative knowledge of how exactly the frequency of the wavefront varies, and how it depends on angle, is required. The pulsed array, in a simplified form, can be modelled using an analytic approach.

4.2 Analytic Model

The pulsed array can be simply modelled as a linear array of point sources, where the elements alternate in polarity, as shown in figure 4.1. It is assumed that the generated waves propagate through a linear, isotropic and homogeneous medium.

Whilst, in reality, the individual elements will not be infinitesimal in size, the approach can be used to provide interesting physical insights that help to explain the underlying principles of the pulsed array. Finite element analysis (FEA) can be utilised if a more representative model, which may, for instance, include material inhomogeneity, is required.

However, this enhanced realism comes at the expense of losing a physical understanding, as FEA is based upon extensive numerical calculations. Using an analytic technique, the array elements can be considered as infinitesimal point sources, which radiate wave energy equally over all angles. In order to calculate the wavefield produced by an array of these point sources, the contribution from each individual element must be summed, considering both the amplitude and phase of the waves. This can be handled with a well established method for calculating wave propagation, based on the Huygens-Fresnel principle [30]. The Huygens-Fresnel principle states that each point on an advancing wavefront is the source of a new wave, which spreads out equally in all directions with a speed equal to the wave speed. The amplitude of the total wavefield at any given point can then be calculated from the summation of these wavelets. This summation must consider phase, as well as the amplitude, of the wavelets, so that the superposition of the wavelets can lead to destructive, as well as constructive, interference of the waves. Huygens' principle can be used to explain a range of wave phenomenon, such as refraction and diffraction, and can be used to simulate the acoustic fields from a range of ultrasonic transducers [3, 135, 169, 170].

As has been seen in Chapter 3, the wavefield produced by a simultaneously excited array is highly dependent upon the excitation signal that is being used to drive the array. Therefore, it is important to consider the frequency content of the excitation signal, $s(t)$, which can be found by applying the Fourier transform to the signal:

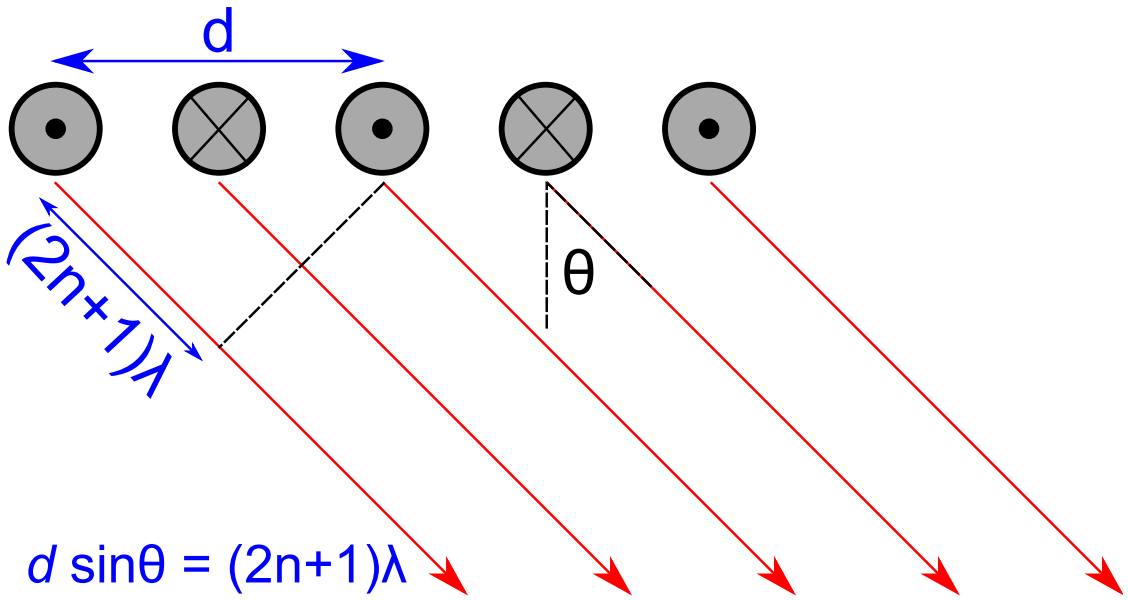

Figure 4.1: A schematic diagram showing the applied force distribution of the pulse array, and illustrates the alternating polarity of the array.

$$S(\omega) = \frac{1}{\sqrt{2\pi}} \int_{-\infty}^{\infty} s(t)\, e^{-i\omega t}\, \mathrm{d}t, \tag{4.1}$$

where ω represents the angular frequency. As the considered array is linear, consisting of equally spaced elements as shown in figure 4.1, the problem can be reduced to a two dimensional one. As there are no elements or periodicity in the array in the third spatial dimension, there are no interesting physical phenomena to model. Also, due to the length to width ratio of the elements, they can be treated as being infinitely long in that direction. As a consequence of reducing the model to two dimensions, the waves generated by each of the individual elements can be considered as a cylindrical wave:

$$u(r, \theta, t) = \frac{u_0}{\sqrt{r}} e^{i(kr - \omega t)}. \tag{4.2}$$

As the wavefront is spreading out in a cylindrical fashion, the energy of the wave is being spread out over the surface of a circle, and hence the initial amplitude of the particle displacement of the wave, u_0, reduces inversely proportional to the square

root of the propagation distance, r. However, the excitation signal will not be of a single frequency; it will contain a range of frequencies which can be calculated from equation 4.1. Hence, the wave produced by the element can be considered as a linear superposition of these cylindrical waves of increasing frequency, with the response at a particular frequency being weighted by the complex frequency spectrum $S(\omega)$ shown in equation 4.1:

$$u_T(r,\theta,t) = \frac{1}{\sqrt{r}} \int_0^\infty S(\omega)\, e^{i(kr-\omega t)}\, \mathrm{d}\omega. \tag{4.3}$$

Now that the wavefield for a single element can be calculated, the pulsed array wavefield can be calculated by utilising Huygens' principle, with the contribution from each individual emitter needed to be summed in amplitude and phase. For an array of N elements, the generated wavefield, ψ, is given by:

$$\psi(x,y,t) = \sum_{p=1}^{N} \frac{(-1)^p}{\sqrt{r_p}} \int_0^\infty S(\omega)\, e^{-i(kr_p-\omega t)}\, \mathrm{d}\omega. \tag{4.4}$$

Here, r_p is the distance from the p^{th} element to the position (x, y). This equation can be numerically evaluated in order to determine the wavefield generated by a linear array of point sources, each being driven simultaneously by an excitation signal $s(t)$. As the formulation is semi-analytical, it gives the freedom to investigate how the generated wavefield evolves in time, and how it varies with different excitation signals. One of the most interesting excitation signals to use to drive the linear array with is a simple Gaussian impulse, which has general form:

$$s_G(t) = \frac{A}{\sqrt{2\pi\delta^2}} e^{-(t-t_0)^2/2\delta^2}. \tag{4.5}$$

The width of the Gaussian function is controlled by the parameter δ, with the pulse peaking at time t_0. The function s_G is an interesting and useful one to investigate; it is the approximate shape of some of the pulses generated by experimental function generators, meaning that the results can be directly compared to experi-

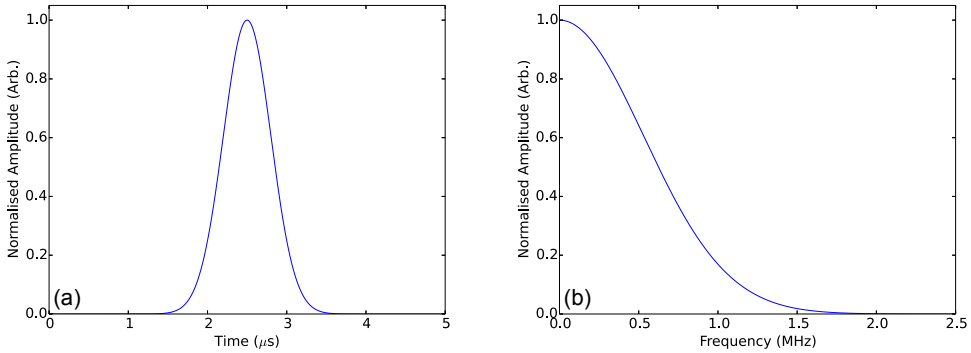

Figure 4.2: The (a) time domain and (b) frequency domain representation of the Gaussian impulse. The Gaussian impulse has a width factor, $\delta = 3 \times 10^{-7}$ s, and is used to excite all of the arrays in this chapter (except Figure 4.7, which is excited with a more broadband Gaussian signal, $\delta = 3 \times 10^{-8}$ s).

ment. Gaussian functions also have the useful property that the Fourier transform of a Gaussian function is another Gaussian function [33], so analysis and conversion between the time and frequency domain becomes easier. In the frequency domain, the Gaussian pulse becomes:

$$S_G(\omega) = \frac{A}{\sqrt{2\pi}} e^{-\delta^2\omega^2/2} e^{-i\omega t_0}. \tag{4.6}$$

From equation 4.6, it is clear that the parameter δ is inversely proportional to the frequency bandwidth in the signal, and it is through δ that the frequency content of the excitation signal can be controlled. An example of the Gaussian excitation signal is shown in both the time and frequency domain in figure 4.2. Substituting equation 4.6 into the general equation 4.4, and utilising the Gaussian integral relation [171], the wavefield produced by pulsing the array with a Gaussian impulse is:

$$\psi(x, y, t) = \sum_p \frac{(-1)^p}{\sqrt{r_p}} e^{-(k_0 r_p - \omega_0(t-t_0))^2/2\omega_0^2\delta^2}. \tag{4.7}$$

Equation 4.7 can be used to simulate the time evolution of the wavefield produced by the array being driven by a Gaussian impulse, as it can be evaluated over a range of spatial values for a range of time steps. By inspecting a series of these "snap-

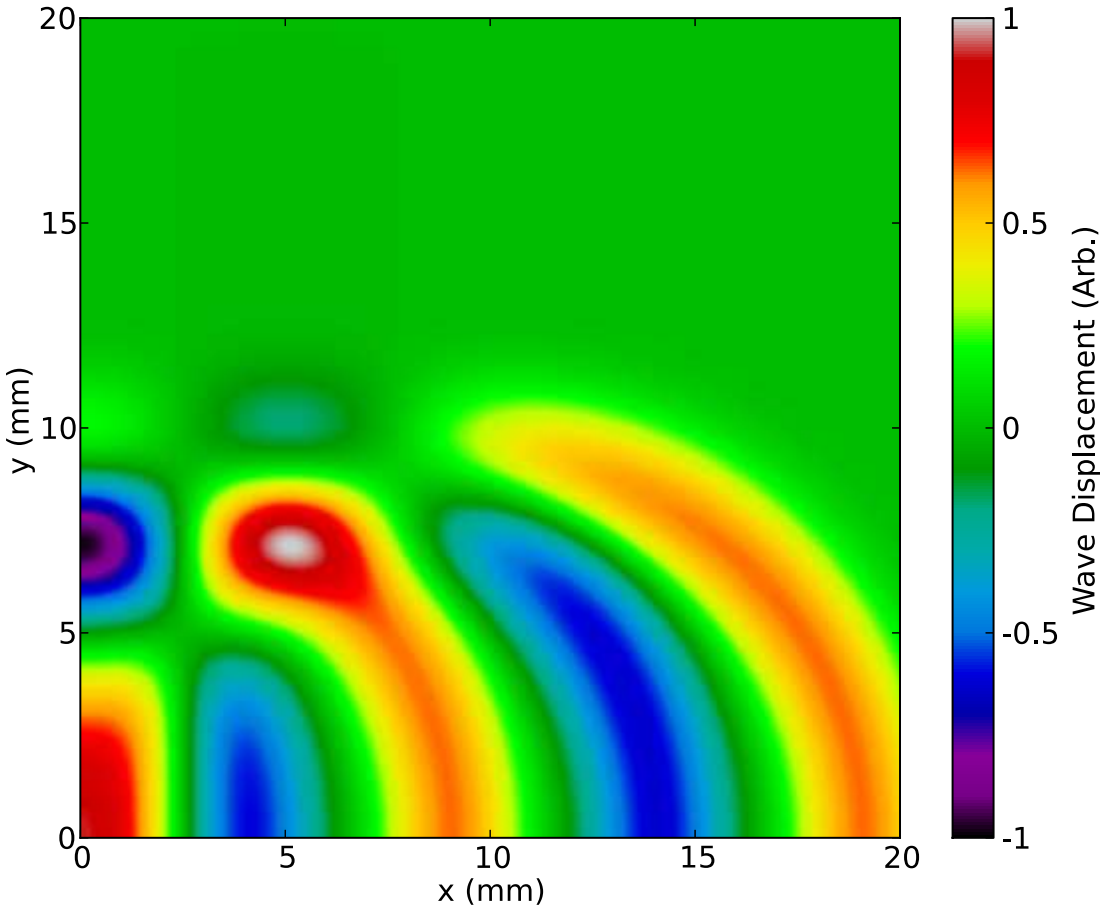

Figure 4.3: Pulsed Array wavefield, generated by a five element array with a pitch of 5 mm, shown in the near-field, 3.5 μs after being pulsed. The array elements are excited with a Gaussian impulse of $\delta = 3 \times 10^{-7}$ s.

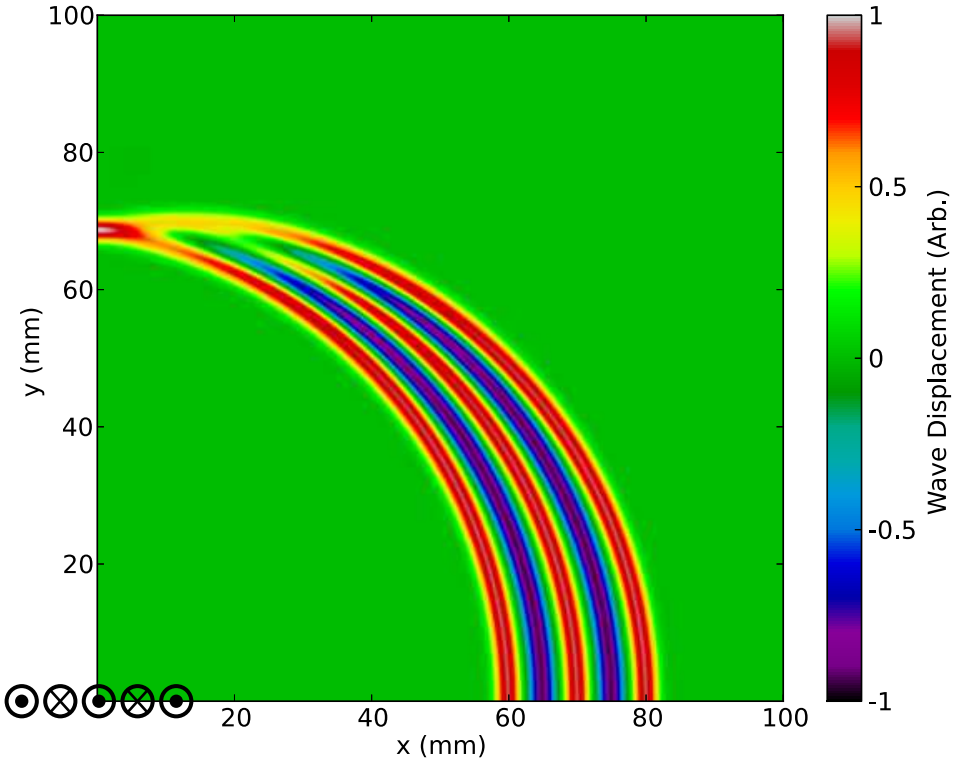

Figure 4.4: Pulsed Array wavefield, generated by a five element array with an elemental separation of 5 mm, shown in the far-field, 22.5 μs after being pulsed. Again, the array elements are excited with a Gaussian impulse of $\delta = 3 \times 10^{-7}$ s. The array elements, with the alternating polarity structure, are shown in the lower left corner of the figure.

shots", it can be seen how the wavefront develops in time, as well as gaining an insight into how the wavefront is created. From the snap-shot, shown in figure 4.3, several important and interesting features of the generated wave can observed. For instance, it can be seen that this phenomenon fundamentally occurs because of the interference between the waves generated by each individual element of the array. This can be observed just after the array has been pulsed, when the wavefront is in the near-field of the array, as the wavefield is complex and rapidly changing. Once away from the near-field, as shown in figure 4.4, it can be seen that a stable wavefront propagates with the speed equal to the wave velocity in the medium of propagation.

Another property of the pulsed wavefront can also be seen from this model; the generated wavefront extends over a large angular range, meaning that a large area can be inspected with just a single wave pulse. Whilst there is clearly ultrasonic energy over the entire angular range, the variation of the frequency of the wavefront is no longer useful in the range $0° \leq \theta \leq 20°$. It should also be noted that, because of the symmetry of the array, there will be a symmetric copy of the wave mirrored along the y-axis. If the array consists of an even number of elements, it is anti-symmetric about its centre, and therefore the wavefront travelling in the $-\theta$ direction will be an anti-symmetric copy of the wave travelling in the $+\theta$ direction.

4.3 Frequency Variation

Perhaps the most surprising and novel aspects of the generated, pulsed wavefront is that the frequency of the wavefront varies smoothly and continuously as a function of angle. From figure 4.4, it can be seen that the frequency appears to be changing monotonically; along the x-axis, at 90°, the frequency of the wavefront is at its lowest, equal to the fundamental frequency of the array. As the angle decreases, the frequency of the wavefront increases until it is three times this fundamental frequency at $\theta = 20°$. This means that for a given measured frequency, it uniquely maps frequency to an angle of propagation in the angular range $20° \leq \theta \leq 90°$. Consequently, the angular position, relative to the centre of the array, can be found by simply measuring the frequency of the wave. The analytic model can be used to gain quantitative knowledge of how the frequency changes along the wavefront, therefore allowing for a relationship between angle and measured frequency to be obtained. Instead of calculating the spatial distribution of the wavefront at a particular time, equation 4.7 can be used to calculate the time history of the wave at a particular position in space; effectively taking a 'measurement' at a point in space. The frequency content of this recorded signal can then be measured, and the peak

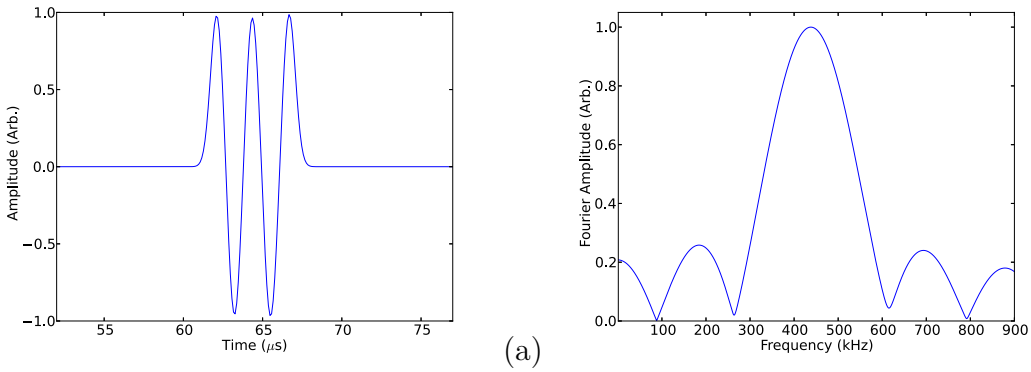

Figure 4.5: (a) Simulated time domain signal of wavefront at 45°, along with (b) frequency domain representation of the same signal.

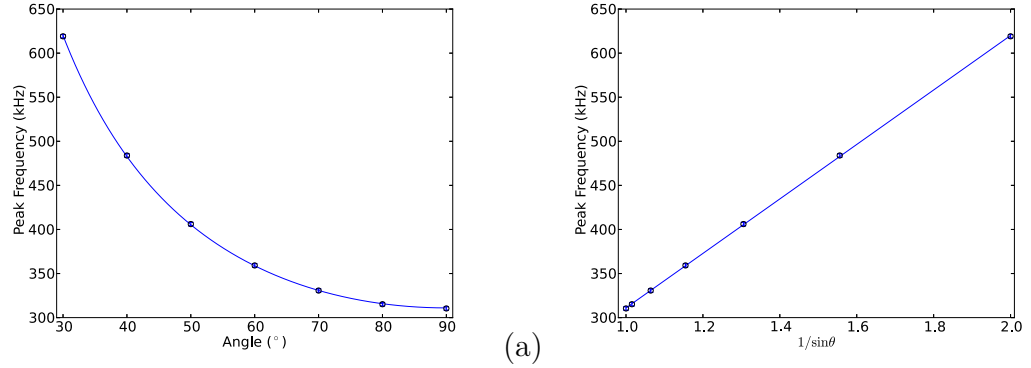

Figure 4.6: Peak frequency of the simulated wavefront as a function of angle (a), which shows the linear relationship with $1/\sin\theta$ (b).

of the frequency spectrum can be obtained. If this is done with a sufficient number of points covering the angular region of interest, it is possible to see how the peak frequency of the wavefront depends upon the angle of propagation. An example of this is shown in figure 4.5, with the time domain signal of the wavefront at 45° to the array; the frequency spectrum of this signal is shown next to the time domain signal. The peak frequency component of the spectrum can be extracted and used to relate the measured frequency of the wave to the angle of propagation. If the peak frequency is obtained at many angular positions along the array, the relationship between frequency and angle can be observed, as shown in figure 4.6.

From figure 4.6, there is a clear relationship between peak frequency and angle of propagation, and the frequency does indeed change as a function of angle, with the

frequency having a $1/\sin\theta$ dependence upon the angle of propagation. This relation is similar to the diffraction grating equation, and acts as confirmation that the pulsed wavefront is an interference effect. Clearly, then, comparisons can be drawn between the pulsed array and a diffraction grating, with elements of alternating polarity, being 'illuminated' by a broadband pulse. In the narrowband excitation case described in Chapter 3, the waves from each element constructively interfere at a particular angle, governed by the diffraction grating equation, which act to steer the ultrasound. However, in the broadband case, the signal contains a range of different frequencies, each of which steer to a different angle; it is this that causes the wavefront to extend over such a range of angles, with a unique frequency, dependent on the direction of propagation. The diffraction grating equation can be re-written in terms of frequency, $\nu = \frac{c}{\lambda}$, to be in the form:

$$\nu(\theta) = \frac{(2n+1)\,c}{d\sin\theta}. \tag{4.8}$$

Here, d is the periodic distance over which the array structure repeats, c is the ultrasonic shear speed and n is the order of diffraction. A consequence of this inverse proportionality between the frequency and the angle propagation is that the frequencies change much more rapidly at the lower angles. This means that the angle of propagation can be measured more accurately as large changes in frequency are needed in order significantly alter the angular position. Hence, for a given uncertainty in the peak frequency component, the uncertainty in the estimated angle of propagation is much less at lower angles than it is at higher angles.

Viewing the array as an alternating polarity diffraction grating also helps to explain why the frequency content of the excitation signal is so important in generating this pulsed array wavefront. If the principle frequency content of the excitation pulse is below the fundamental frequency, $\nu_0 = c/d$, then it is not possible for constructive interference to occur. Consequently, all that is generated is a wavefront of a single frequency, as if it has been generated by a monolithic transducer. Furthermore, if

the signal has significant frequency above three times the fundamental frequency, then higher order diffraction modes ($n > 0$) can exist. If these higher order modes are allowed to exist, they can mix in with the fundamental diffraction mode. This can lead to a distortion of the wavefront, and will mean multiple frequencies will be present at a particular angle. Therefore, it can be seen that it is not just a case of exciting the array with a broadband pulse; the signal needs to have a wide range of frequencies, this range must be carefully selected with respect to the array geometry, with special consideration being paid to the periodicity of the array.

4.3.1 Frequency Domain Representation

An alternative, although ultimately equivalent, way to investigate the frequency variation is to apply a Fourier transform to the generated wavefield once it is in the far field. Once in the far field, the stable wavefront will propagate with a constant speed, with the amplitude decaying as the wave energy is spreading out over a greater area. As the propagation of the wave has the effect of varying only the phase of the wave, and geometric attenuation is frequency independent, the peak frequency of the wavefront at a given angle will not change in the far field. By calculating the wavefield at a sufficient distance, and then applying a discrete Fourier transform (DFT) to this, the frequency content of the signal as a function of angle can be seen.

The DFT is calculated numerically, by calling the fast Fourier transform (FFT) function from the numpy module of the Python programming language. The numpy implementation of this FFT is based upon the Cooley–Tukey algorithm [172], which works by dividing the input signal into even- and odd-indexed components and calculates the DFT of these separated inputs. By dividing the input in this way, and utilising the circular symmetry property of the DFT [33], the number of operations (in this context, an operation involves a complex multiplication followed by a complex addition [172]) can be reduced from $\mathcal{O}\left[N^2\right]$ to $\mathcal{O}\left[\frac{N^2}{4}\right]$, where N is the number of samples. This division can be done recursively, and in the asymptotic

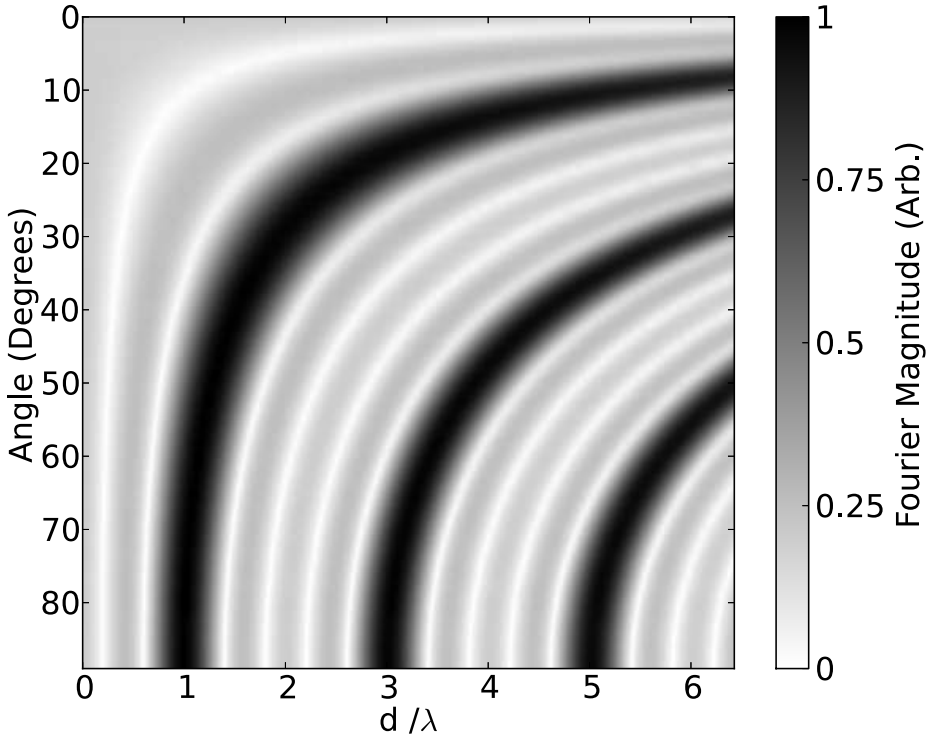

Figure 4.7: Frequency spectrum of wavefield generated by a 5 element array excited by a Gaussian impulse of $\delta = 3{\times}10^{-8}$ s. This broadband signal allows the impulse response of the array to be seen.

limit, the complexity scales as $\mathcal{O}\left[N \log N\right]$ [172]. Therefore, the input signal should have a length equal to a power of two to ensure efficient calculation. All signals used within this work had the same length, 65536 (2^{16}) samples, so that DFT coefficients correspond to the same frequency bins, and that different spectra can be compared.

This is first done for an extremely wideband pulse in figure 4.7, whereby the Gaussian impulse signal has a width $\delta = 3 \times 10^{-8}$ s, which corresponds to a -6dB bandwidth of 40 MHz. Due to this large bandwidth, the frequency response of the array to be calculated, and all of the key frequency domain features of the array can be seen. Figure 4.7 has been plotted in a dimensionless way, so that it is independent of array size. Many strong bands of intensity can be seen in the frequency spectrum, and these correspond to the different orders of diffraction modes predicted by equation 4.8. This again highlights the diffraction grating-like nature

of the array.

The necessity of carefully selecting the frequency content used to drive the array can also be seen from figure 4.7, especially when compared to figure 4.8, where the frequency content has been correctly chosen so that only the lowest order mode can be generated ($\delta = 3 \times 10^{-7}$ s). Below $d/\lambda = 1$, there is limited energy generated at any angle meaning that there would be inefficient conversion of the generation signal into a propagating wave. The higher order diffraction modes can also be clearly seen, with successive modes being activated at odd-integer values of the fundamental dimensionless frequency of the array. If the signal is allowed to contain frequencies higher than $3c/d$, then the generated wavefront will be a mixture of the fundamental $n = 0$ mode and at least one other higher order mode. Hence, by limiting the frequency content of the excitation pulse below this value, one can ensure that no higher order modes can overlap with the lowest order constructive interference modes, as is the case with figure 4.8.

4.4 Design Considerations

4.4.1 Alternating Polarity

It is interesting to see what effect the alternating polarity structure of the pulsed array has on the generated wavefront. Whilst it is not particularly difficult to achieve, it is unusual to have an array where the elements alternate in polarity; so it is important to have some justification for implementing this design. The analytic model can be easily adapted to simulate the pulsed wavefield from an array where all elements are excited in phase with each other. This simulated wavefield can be compared to the wavefront generated with an alternating polarity, to see if the structure offers any advantages when compared to the traditional, in-phase configuration. The wavefield generated by a wideband pulse ($\delta = 3 \times 10^{-8}$), shown in the frequency domain, can be seen in figure 4.9. There are a number of interesting

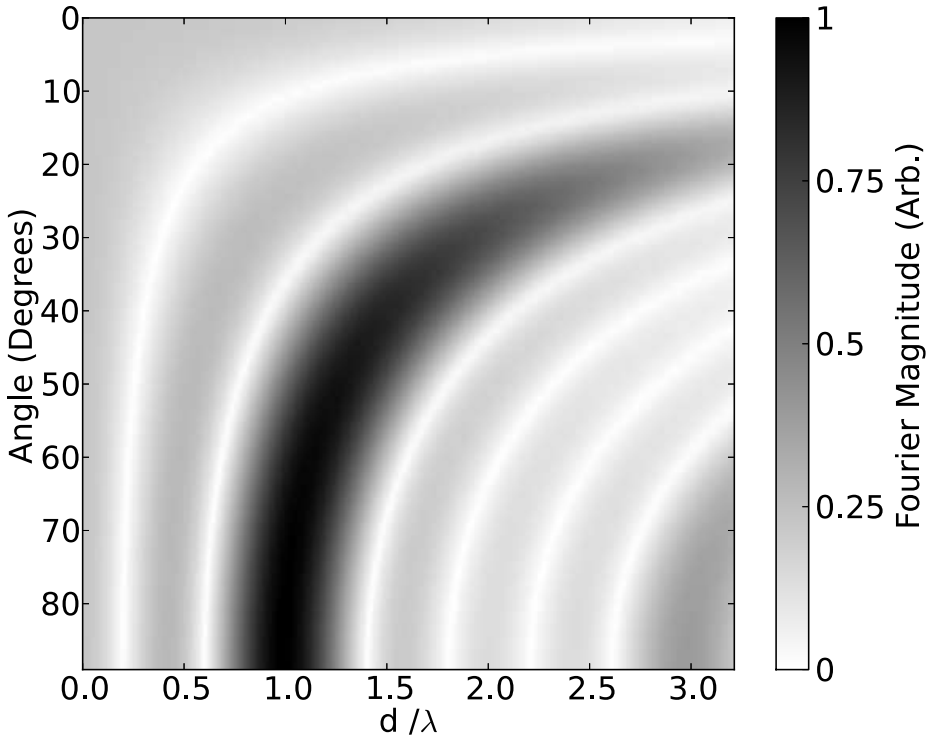

Figure 4.8: Frequency spectrum of the wavefield generated by a 5 element array excited by a Gaussian impulse with a carefully selected frequency spectrum, with $\delta = 3{\times}10^{-7}$ s.

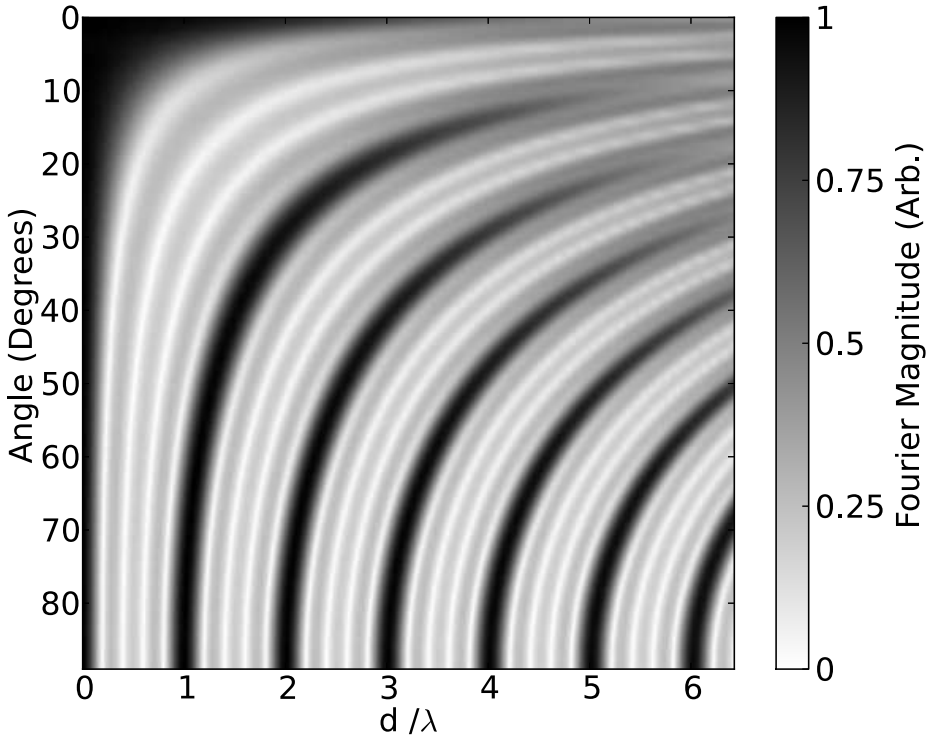

Figure 4.9: Frequency spectrum of wavefield generated by a 5 element array, with all of the elements in phase, excited by a Gaussian impulse of $\delta = 3{\times}10^{-8}$ s.

and useful differences between the in-phase wavefield and the direct comparison of the anti-phase array, shown in figure 4.7.

The first difference is that the in-phase arrays can support the even-number diffraction modes, in addition to the odd-number diffraction modes that the anti-phase array can generate. This means that in order to satisfy the condition that only the lowest order diffraction term, the upper bandwidth limit of the excitation signal must be dropped so that the $n = 2$ mode is not activated. For this to be the case, there must be no components of the generated wave with a wavelength smaller than $\frac{\lambda}{2}$. This constraint limits the angular extent of the wavefront to the range $30° \leq \theta \leq 90°$, which means the wavefront generated by the anti-phase array covers more than 10° extra when compared to the in-phase array.

There is also a strong response, at all angles, for frequencies equivalent to $\frac{d}{\lambda} = 0$. This response is caused by the coherent shearing force of all the elements acting in unison, and has no strong dependence on the angle of propagation. This zeroth order mode, then, just acts to obscure the useful, frequency dependent first order mode. This is in contrast to phased array systems, where frequency dependent grating lobes obscure the useful phased beam [1, 136].

4.4.2 Element Number

All of the models in this chapter have been simulating arrays with an odd (five) number of elements, which has been for practical reasons. By using an odd number of elements, symmetry can be evoked with a plane of reflectional symmetry running through the centre of the of the middle element. This symmetry can be beneficial as it can reduce the size of the model, which leads to a reduction in computation time and the demands on computer resources. Whilst this is not important for the semi-analytical modelling performed here, it can have significant effects when using finite element analysis, which is used in Chapter 5. Hence, in order to compare the semi-analytical models with the FEA, they also simulated five element arrays.

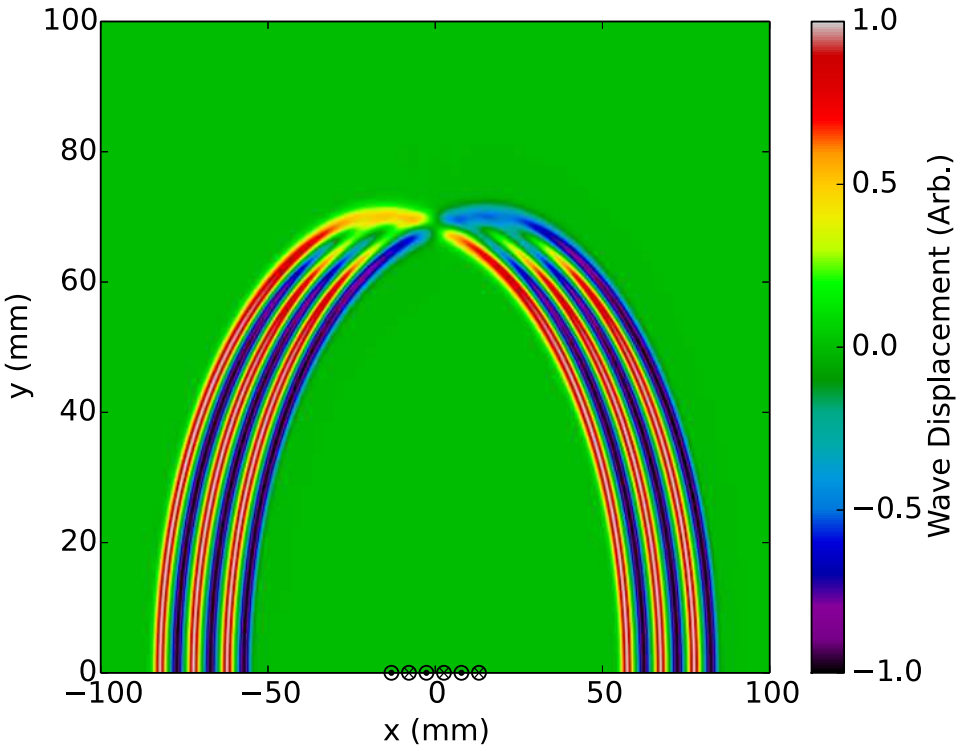

Figure 4.10: Pulsed Array wavefield, generated by a six element array with an elemental separation of 5 mm, shown in the far-field, 22.5 μs after being pulsed. The array, which is centred at $(x, y) = (0, 0)$, is excited with a Gaussian impulse of $\delta = 3 \times 10^{-7}$ s. The anti-symmetry of the array is reflected in the phase inversion of the wavefront.

However, because this technique does not implement symmetry and, being an analytic technique, it can simulate the wavefield relatively quickly, it can be used to investigate the effect of number of elements has on the generated wavefront.

There are two differences between the wavefield from a five or a six element array. The most obvious difference is between the symmetry conditions; for an odd number of elements, the array is symmetric about the centre of the array. However, for an array with an even number of elements, the array is now anti-symmetric about its centre. The symmetry of the array is important as it indicates the symmetry that the wavefield will possess. In the case of the anti-symmetric array, it is possible to discriminate between the section of the wavefront travelling in the $+\theta$ direction and the wave travelling in the $-\theta$ direction; the two waves are phase shifted by π

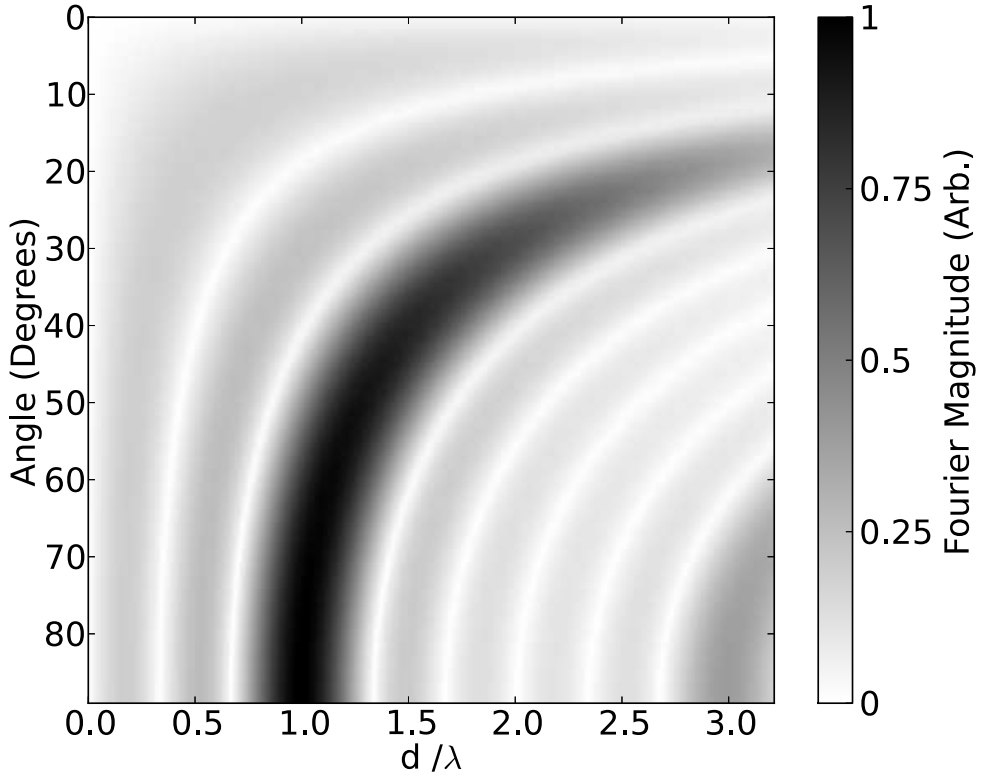

Figure 4.11: Frequency spectrum of the wavefield generated by a six element array excited by a Gaussian impulse with a carefully selected frequency spectrum, with $\delta = 3{\times}10^{-7}$ s.

radians relative to one another. In addition to this, as there are the same number of 'positive' and 'negative' polarity elements, there is no displacement directly above the centre of the array, as the waves from each elements cancel out at this point. This is shown in both the time and frequency domains in figures 4.11, which shows the result from an array consisting of six elements. For the odd number of elements, there is no wave to cancel out the central element, meaning that there is a small signal generated at 0°.

As well as symmetry considerations, the total number of elements in the array also has an effect. The length of the time domain signal increases in proportion with the number of elements in the array, as is apparent in figure 4.12. This longer time domain signal leads to a decrease in axial resolution [173]. However, whilst the increased pulse length leads to a reduction in the axial resolution, it leads to a

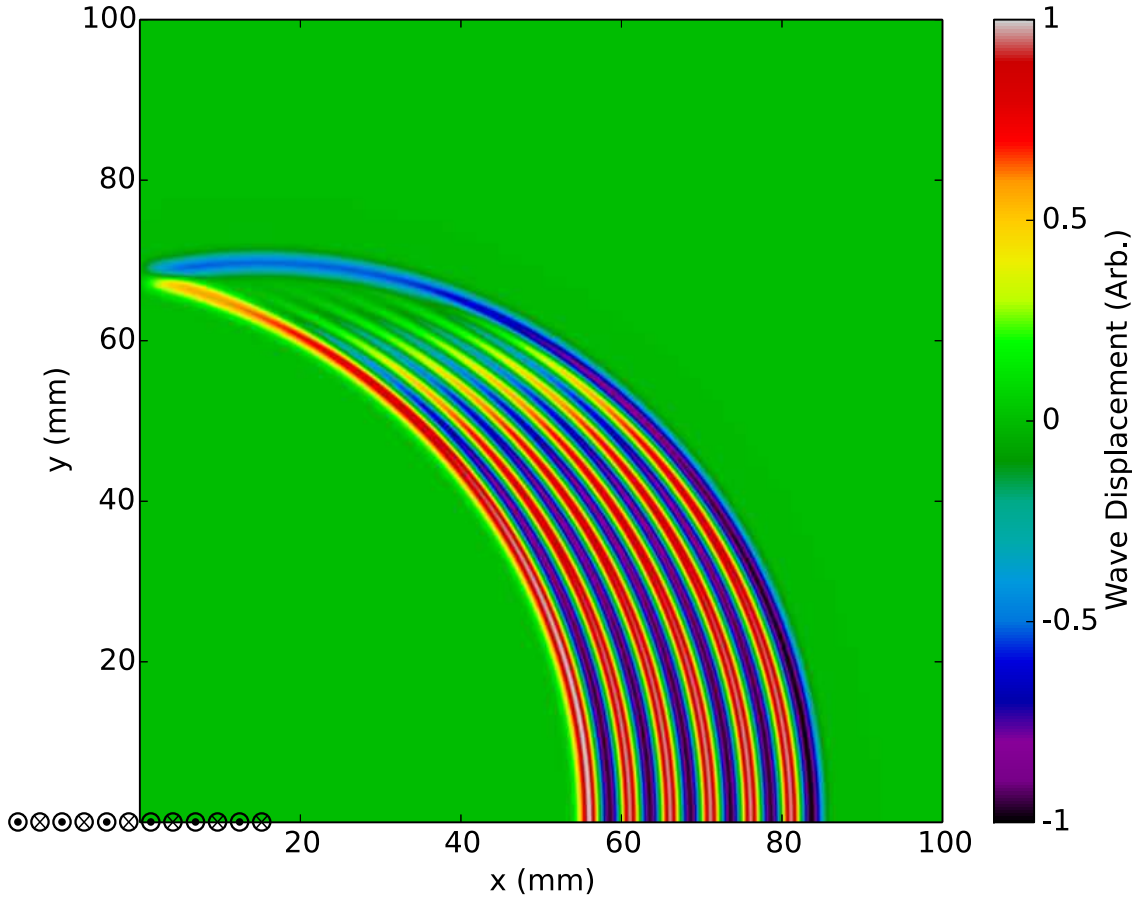

Figure 4.12: The time domain signal from a pulsed array that consists of 12 elements of alternating polarity. The array is pulsed with a Gaussian impulse with $\delta = 3 \times 10^{-7}$ s. Note the significant increase in length of the signal when compared to figure 4.4, which consists of five elements.

narrower spectrum in the frequency domain with a reduced bandwidth, as can be seen from figure 4.13. Therefore, any improvements in axial resolution will come at the expense of a wider frequency distribution, and vice versa. This trade-off is a consequence of the time - frequency uncertainty principle, with a narrower time distribution necessarily leading to a broader frequency distribution, with the reverse also being true. Therefore, there is a compromise between an array with enough elements to create a coherent interference wavefront, whilst still being temporally compact enough to retain good axial resolution.

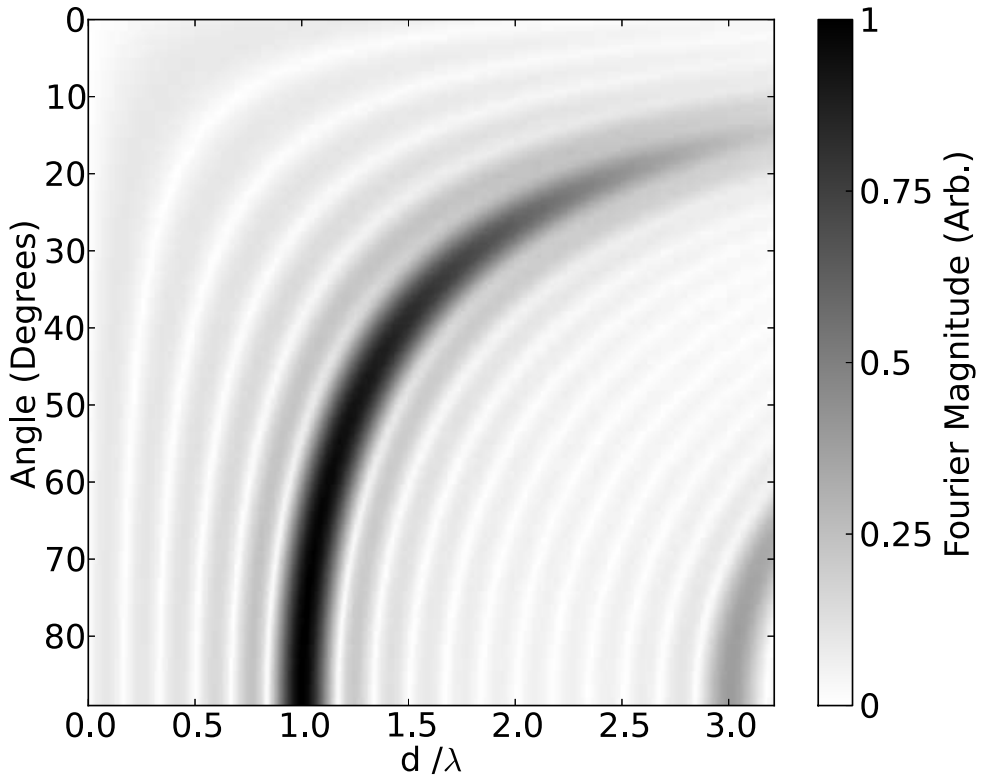

Figure 4.13: The frequency domain signal from a pulsed array that consists of 12 elements of alternating polarity. The array is pulsed with a Gaussian impulse with $\delta = 3 \times 10^{-7}$ s. The interference bands are localised more in frequency, when compared to figure 4.8, which is obtained from an array consisting of five elements.

4.5 Conclusions

A simple Huygens construction model has been created in order to explain the physical processes behind the generation of this interesting wavefront, with its novel properties. This wavefront has the surprising property of having a smoothly varying frequency and amplitude profile, as well as covering a large angular region. These novel characteristics can be easily achieved, as the wavefront is generated by simultaneous activation, precluding the need for any complex or expensive electronics to control the excitation of the array, as is the case with phased array controllers. Whilst this approach is not meant to accurately model every single aspect of the array, the simplifications allow for some physical insights to be gained. For example, the fact that the generated wavefield arises from interference effects, and that the array can be treated like a diffraction grating, becomes apparent from this analysis. The semi-analytic nature of the model means the calculation times are low, when compared to finite element analysis, for instance. This makes it an ideal tool for sweeping through different array parameters, such as the number of elements or the frequency bandwidth of the excitation signal.

It has been shown that the frequency content of the excitation signal is very important, with the generation signal needing to have significant frequency content between the fundamental frequency, $\nu_0 = \frac{c}{d}$, and three times this value. This ensures that the signal is of high enough frequency to ensure that the spatial periodicity of the array can be used to create a diffraction pattern, whilst limiting the range of frequencies so that no higher order modes are present. The requirement to have alternating polarity elements is also highlighted, as are the advantages of using an array with an even number of elements. This approach is also very general. There has been no mention of the nature of the array, only that it consists of a line of point emitters that generate a wave. Consequently, this result is universally applicable to ultrasonic, as well as radar and sonar arrays. Whilst the model neglects the conversion from electrical energy into a propagating wave, as long as the force

distribution on the surface is known, this model can be used to propagate the waves in order to determine the generated wavefront.

However, whilst applying some simplification can give some physical insights into the principles, it also means that some aspects of the array are neglected and not modelled. For instance, this model assumes that the wave is travelling in a semi-infinite linear, isotropic and homogeneous material. Whilst it is possible to model more complex scenarios using the Huygens' approach [174, 175], the problem is better suited to finite element analysis. FE analysis can be used to obtain a more representative simulation of the wavefield generated by an actual array, as well as how the wavefront interacts with discontinuities, however this does not provide the same physical understanding as the analysis performed in this chapter.

Chapter 5

Finite Element Analysis

The analytic model discussed in Chapter 4 was useful, as it could be used to investigate and extract the key physical features that are responsible for generating the pulsed array wavefront. However, certain simplifications had to be made in order to make the calculations tractable, which inevitably lead to some aspects of the array being neglected. A more complete model can be obtained through increasingly numerically intensive methods, although this comes at the expense of losing some physical insight, which is obscured by the computational complexity of the models. Finite element modelling was chosen to perform this numerical analysis, as it has the advantage that anisotropy, inhomogeneity, complex geometries and global conditions are easily handled by the discretisation of the finite element model [176]. Finite element analysis, performed with the commercial package PZFlex, is used in this chapter to create a more accurate model of the pulsed array wave, which considers an arbitrary excitation signal and finite sized array elements. Once a suitable model for the pulsed array has been constructed, and verified with experiments, it can be used as an aid to investigate more complex scenarios, such as simulations of the wavefront interacting with scatterers.

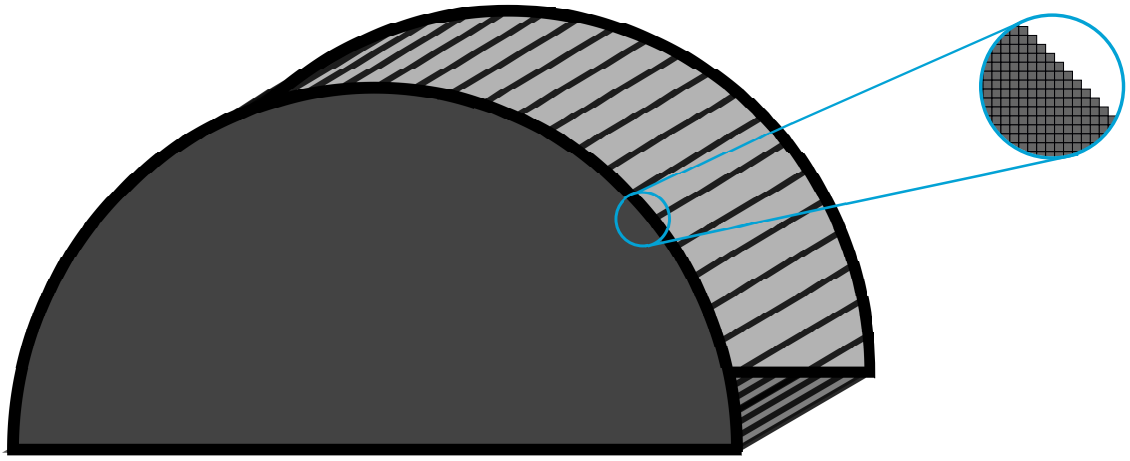

Figure 5.1: An example of a complex shaped component being discretised into finite elements.

5.1 Finite Element Theory

Finite element analysis is commonly used as a modelling tool to numerically investigate the behaviour of complex dynamic systems. This complexity may be in the form of an arbitrarily shaped region of interest, scattering events or a general lack of symmetry in the calculations, precluding analytical solutions. The basis of the FE method is to decompose a structure into a series of discrete elements, as shown in figure 5.1, to form a mesh. Due to the relative simplicity of the discrete element shape, when compared to the overall shape of the structure, the series of difference wave equations that describe the situation can be solved for each individual element. By solving the difference equations for each element across the entire mesh, as well as imposing representative global boundary conditions, a solution to a complicated problem can be found. For example, ultrasonic wave propagation can be modelled by considering the wave equations (equation 2.9), and attempting to numerically solve these equations for a given mesh of finite elements. After finding a self-consistent series of solutions for each individual element, these can be used to obtain a global solution of the wave equation for the entire model, which can then be used to calculate various model parameters, such as wave displacements, velocities or pressures.

However, the numerical approximations used in finite element analysis can introduce numerous errors, and so care must be taken when discretising the model. For instance, if the mesh is not sufficiently fine, a propagating wave will experience numerical dispersion [177, 178]. Suggestions of appropriate mesh density are given by various sources, although these are little more than rules of thumb. Therefore, in order to check whether the solution is accurate, the convergence of the solution should be checked [176,179,180]. Model convergence is the idea that, as the element size is reduced, the finite element solution should more closely resemble the 'true' solution. In this work, convergence was checked for by increasing the mesh density by 50%, and quantitatively investigating whether the output of the model changed significantly. If the residual difference between the two models was below 1%, it was assumed that the solution had converged. If the solution had not converged, the mesh density was increased by 50% again until convergence was achieved. Whilst increasing the mesh density will lead to improved accuracy in the model results, it will also increase the amount of elements in the model, which will lead to increased computation times and memory usage. Therefore, a balance must be achieved in order to obtain an adequate amount of elements needed to simulate the system. If the mesh density is too low, then the model will not converge to the correct value. However, if the element size is made too small, the simulation will become impractically large.

The number of elements used in a FEM can be reduced by adroit use of the model boundary conditions and the introduction of symmetry. For instance, the size of a model can be reduced by a half with the introduction of a single symmetric boundary condition. Hence, if the array and sample possess a degree of symmetry, this can be exploited to reduce the computation time. Absorbing boundary conditions can also be used to reduce the model size, by scaling it down in directions that are not important [181]. The use of absorbing boundary conditions is also advantageous as it can reduce the amount of unwanted scattering from the interfaces

of the model, making the simulated signals easier to interpret. PZFlex implements the so-called Material Independent Non-reflecting Treatment (MINT) condition for absorbing boundary condition, as it works equally effectively with non-linear disturbances as it does with linear wave propagation [181, 182].

PZFlex is a commercial finite element package that utilises an explicit time domain approach. Consequently, it lends itself to rapid analysis of broadband wave phenomenon, as time domain approaches are inherently broadband [183]. PZFlex was used to model a similar array as in Chapter 4, but includes the effects of the array being comprised of elements with finite size. This allows for a quantitative comparison between the finite element and analytic models to see how the simplifications of the analytic model affect the generated wavefield. PZFlex is also capable of modelling the response of piezoelectric crystals to a given electrical impulse, which would allow for a piezoelectric pulsed array to be fully modelled. However, this was not implemented, in order to keep the model as general as possible. In this case, the the array elements were modelled as a suitable pressure load on the surface of the model.

5.2 Pulsed Array Model Geometry

The advantage of using FEM is that it can be used to create a realistic representation of a physical array. A five element array with a 5 mm pitch ($d = 10$ mm) is modelled, to allow for direct comparison with the analytic model wavefront shown in figure 4.4. However, in contrast to the analytic modelling, the finite size of the elements that form the array will be considered. Both two-dimensional and three-dimensional models were created, with the output of the three-dimensional model recorded in the plane intersecting the middle of the array. The results obtained from the three dimensional model were principally the same as the two dimensional model. This is due to the long nature of the array elements in the third dimension; for shorter array

elements, the edge effects cannot be ignored, and a full three dimensional model must be constructed. However, as the array elements were long enough so that there are not edge effects in the centre of the array, a two dimensional model was found to be sufficient. This has the advantage of significantly reducing the computation time of the models. In order to make direct comparison with the analytic model, shear horizontal waves need to be generated. Hence, a two dimensional SH model was constructed, with shear stresses being applied to the model surface, as shown in figure 5.2. The shear stresses, meant to represent an experimental pulsed array system, had a length of 4 mm, with a space of 1 mm between the elements, creating an array with a pitch of 5 mm. The shearing forces had a Gaussian time dependence, so that the displacement would be directly comparable to the analytic models. As the array has five elements, it is symmetric about its centre point. Therefore a symmetric boundary condition can be used to create a mirror plane along the centre of the array, as shown in figure 5.2. This symmetric boundary condition means that the model size is reduced by a factor of two, decreasing the amount of resources needed to complete the simulations.

The array was then simulated operating into a semi-circular sample, with a radius of 125 mm. This radius was chosen to ensure that the wavefield was measured comfortably in the far-field of the array. Measurements of the displacement in the z-direction were taken in 1° increments over the full 90° of the curved surface of the semi-circle. The semi-circular sample was simulated so that it represented aluminium, with characteristic wave speeds and material properties taken from reliable sources ($\rho = 2690$ kgm^{-3}, $v_l = 6306$ ms^{-1} and $v_s = 3111$ ms^{-1}) [184].

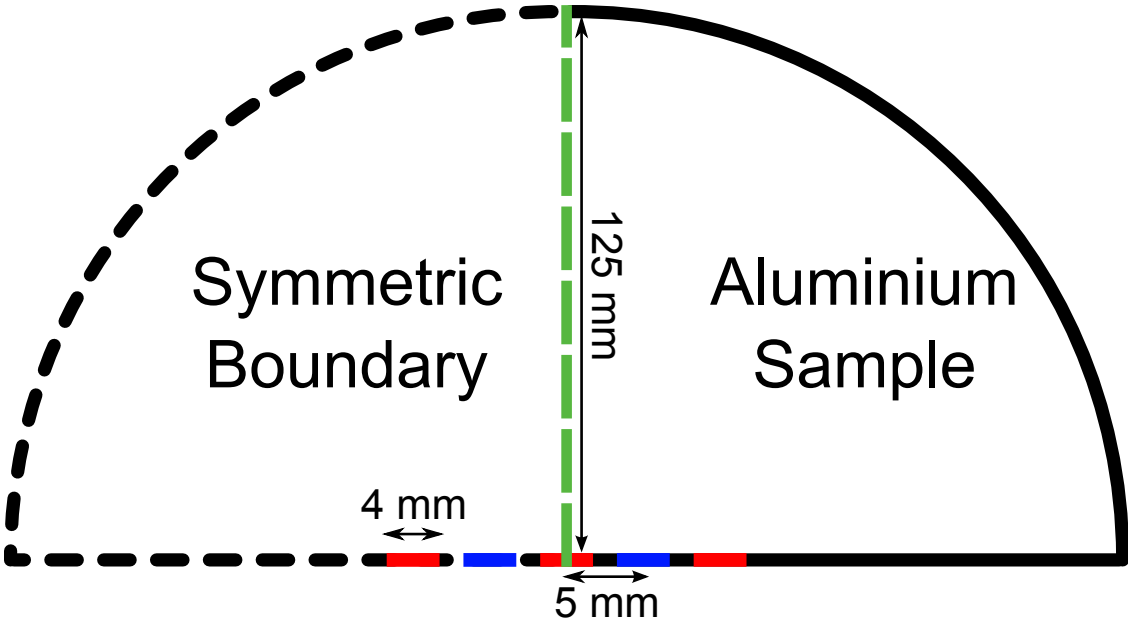

Figure 5.2: PZFlex Model diagram showing the boundary conditions of the model, with the symmetric boundary condition in the centre of the model. The shear stress loading position and polarity is also shown, with red indicating stress-loads shearing into the page, with the blue elements having shear stress being applied out of the page.

5.3 Results

5.3.1 Time and Frequency Domain Results

The aim of the model was to see what effects finite sized sources would have on the generated wavefront, both in the time domain and the frequency domain. As PZFlex is a time-domain modelling package, the results were immediately available in the time domain. However, as with the analytic model in Chapter 4, the frequency domain data can be obtained by applying a fast Fourier transform function, which is called from the numpy Python library, to the time domain data. As with Chapter 4, the time domain data is zero-padded so that it contains 65,536 (2^{16}) data points. This ensures that the frequency information can be directly compared to the data obtained from the analytic modelling. In addition to this, the same excitation signal, a Gaussian impulse was used, with $\delta = 3 \times 10^{-7}$ s. The time domain data, after being re-projected onto a Cartesian grid, can be seen in figure 5.3. Visually, it can be

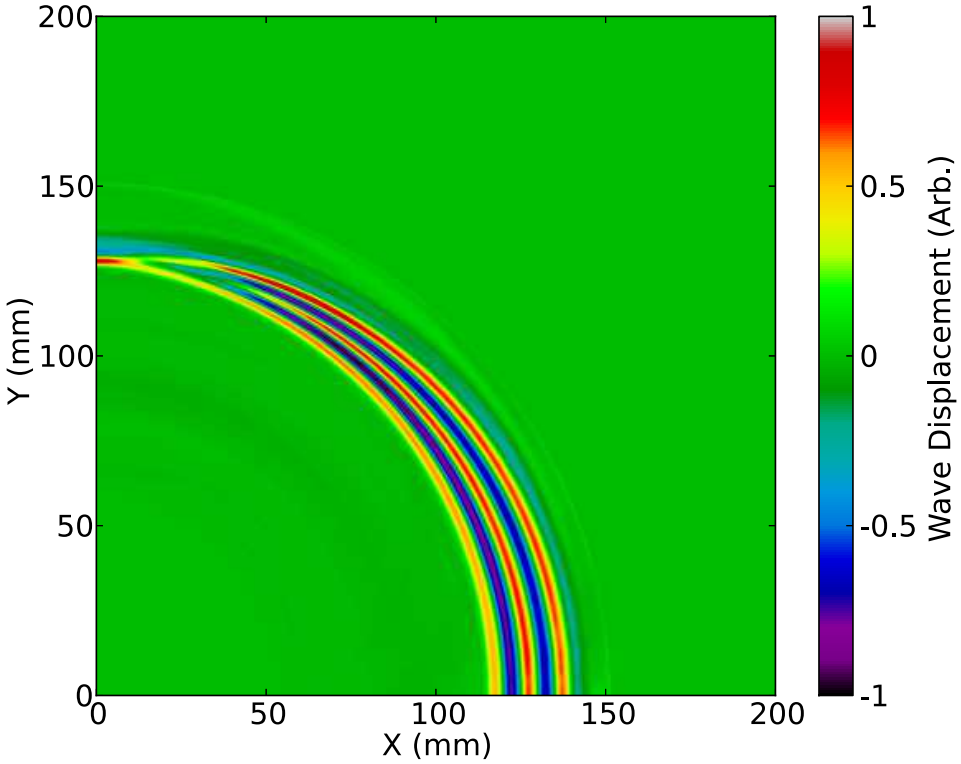

Figure 5.3: Time domain data obtained from the FE model, with the results projected onto a Cartesian grid. The shear wavefront is simulated in aluminium, and therefore has a group speed of 3111 ms^{-1}.

seen that figure 5.3 and figure 4.4 are very similar, with the same key characteristics. The finite element result shows that a wavefield is extended over the full range of angles, and the frequency of the wavefront clearly varying as a function of angle. The variation shows an inverse relationship between angle and frequency, with the lowest frequency section of the wave located at $\theta = 90°$, with the frequency of the wave steadily increasing until the wavefront becomes incoherent at around 20°. These are all important features of the wavefront, and can be seen in both the finite element model and the analytic model, with negligible differences between the two models in the time domain.

However, whilst there may be minimal differences between the two models in the time domain, it is also important to investigate the finite element results in the frequency domain, which can be seen in figure 5.4. The distinctive bands associated

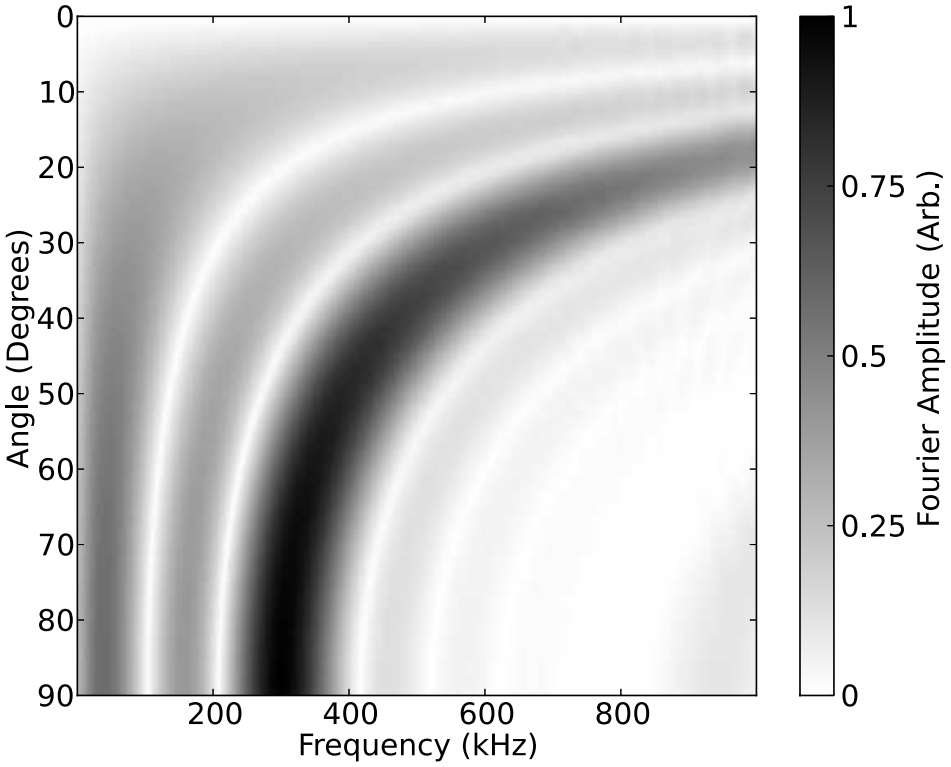

Figure 5.4: The frequency domain data obtained from the FE model, showing the frequency content of the wavefield generated by a 5 mm pitch array, with elements 4 mm in size. The array is excited with a Gaussian impulse with $\delta = 3{\times}10^{-7}$ s.

with diffraction modes can be clearly seen, which confirm that the frequency does indeed vary, due to the constructive interference of the waves as a consequence of the spatial periodicity of the array. However, there are some subtle differences between the frequency domain data in figure 5.4 and that in figure 4.8. Whilst the overall structure of the frequency representation is the same - a strong interference band that varies with angle, with smaller amplitude side bands - there are minor differences in the frequency domain data obtained from the finite element simulation. These differences come in the form of the relative amplitudes of the side lobes; with the low frequency side lobes having a higher amplitude, with the higher frequency lobes having a diminished amplitude. From equation 4.8, a higher order diffraction mode should be activated at 933 kHz. However, it has been much reduced in terms of amplitude when compared to the analytic model.

5.3.2 Frequency Variation

Whilst it has been seen that, in both the time and frequency domain, the wavefield simulated using finite element analysis conforms to the results predicted by the analytic model, an important parameter is the peak frequency component as a function of angle, as this will allow for conversion between measured frequency and the angle of propagation. Presented in figure 5.5 is the measured peak frequency of the wavefront at a particular angle. This was obtained in a similar fashion to the analytic model, with the time domain signal obtained at a particular angle. The numpy FFT algorithm was then applied to the time domain signal in order to transform the signal into the frequency domain, and then extracting the frequency at which the peak coefficient occurs. The expected behaviour, from a diffraction grating, is also shown in figure 5.5 to act as a comparison. It can be seen that there are some differences between the peak frequencies predicted by the analytic models, and those obtained from the finite element model. However, these differences appear to be small variations, with the general trend of the diffraction grating equation still being the dominant process driving the variation in frequency.

5.4 Comparison with Analytic Model

Whilst there appear to be negligible differences between the wavefront generated by finite element analysis and the analytic model, these differences need to be understood and explained. Clearly, the main physical difference between the two models is the inclusion, in the FE model, of the finite size of the sources. The finite size of the elements in the array will have a number of effects on the generated wavefield. Firstly, due to the increased generation area, the total energy of the wave will be increased for larger elements. The finite size of the element will also mean that the elements no longer emit waves omnidirectionally. The angular distribution of the intensity of the wavefield generated by a single element is called a directivity function.

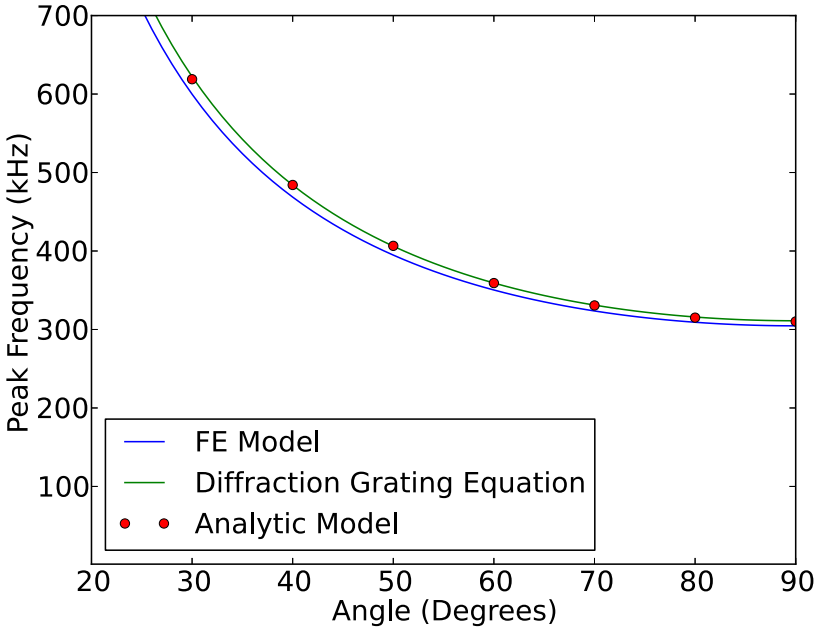

Figure 5.5: The peak frequency of the wavefront generated by the finite element model. For comparison, the expected peak frequencies from the diffraction grating equation, and results obtained from the analytic model, are also shown.

For an omnidirectional point emitter, the directivity function is equal to unity for all angles, as it emits waves of equal intensity at all angles. However, for a finite sized element, the directivity function is modified, according to the shape of the element, as is shown in figure 2.11 for a rectangular aperture. As discussed in Section 2.3.3, the far-field directivity function can be calculated from an element's shape by simply taking the spatial Fourier transform [147–149], which comes from the application of the Fraunhofer diffraction equation [39, 145]. For a simple rectangular aperture, the directivity function, $D(\omega,\ \theta)$ is given by:

$$D(\omega,\ \theta) = \operatorname{sinc}\left(\frac{\pi a \sin\theta}{\lambda(\omega)}\right). \tag{5.1}$$

As the signal that is used to excite the array is broadband, each frequency component will have an individual directivity function. The directivity of a 4 mm rectangular element, for the frequencies of interest, is shown in figure 5.6. It can be seen from these figures that the acoustic intensity, for all frequencies, is maximum at

$\theta = 0°$ and all frequencies are emitted equally efficiently in this direction. However, for high angles, the variation in the emission efficiency with frequency becomes more pronounced. For the lower frequencies, ultrasound can still be efficiently generated at higher angles ($\theta \rightarrow 90°$) as the element behaves more like an omnidirectional source; whereas at higher frequencies, the efficiency is very low, with no appreciable signal being generated at 800 kHz. As a consequence, for all angles not equal to 0°, a lower frequency wave will be more efficiently generated than higher frequency wave. This directivity phenomenon can be used to explain why the measured peak frequencies from the FE model are lower than the values expected from the diffraction grating equation. Whilst the diffraction grating equation predicts the relationship between frequency and angle for an omnidirectional source, it does not take into account the fact that different frequencies are emitted with different efficiencies. Hence, for an array comprising of elements with a finite size, the peak frequencies will be smaller than predicted from the diffraction grating equation.

However, it can be seen from figure 5.5 that the differences between the analytical model and the results obtained from the FE model are a small deviation from the expected diffraction grating equation. Whilst the difference between the FE model and the diffraction grating result is growing as angle is decreasing, the largest difference between the two is 28 kHz, which occurs at 24°. This corresponds to a percentage deviation from the diffraction grating equation of 3.8%. Indeed, the mean deviation from the diffraction grating equations, for angles above 25°, is less than 3%. Consequently, the diffraction grating equation still provides a relatively accurate conversion between peak frequency and angle of propagation. The difference in peak frequency is small because it is the lower frequencies that are steered to the higher angles, where the change in directivity is less pronounced. For these lower frequencies, the array elements act more like a point source, so the lower frequency energy can be steered these higher angles. For the higher frequencies, the elements act as a more directional source, but these frequency components are being steered

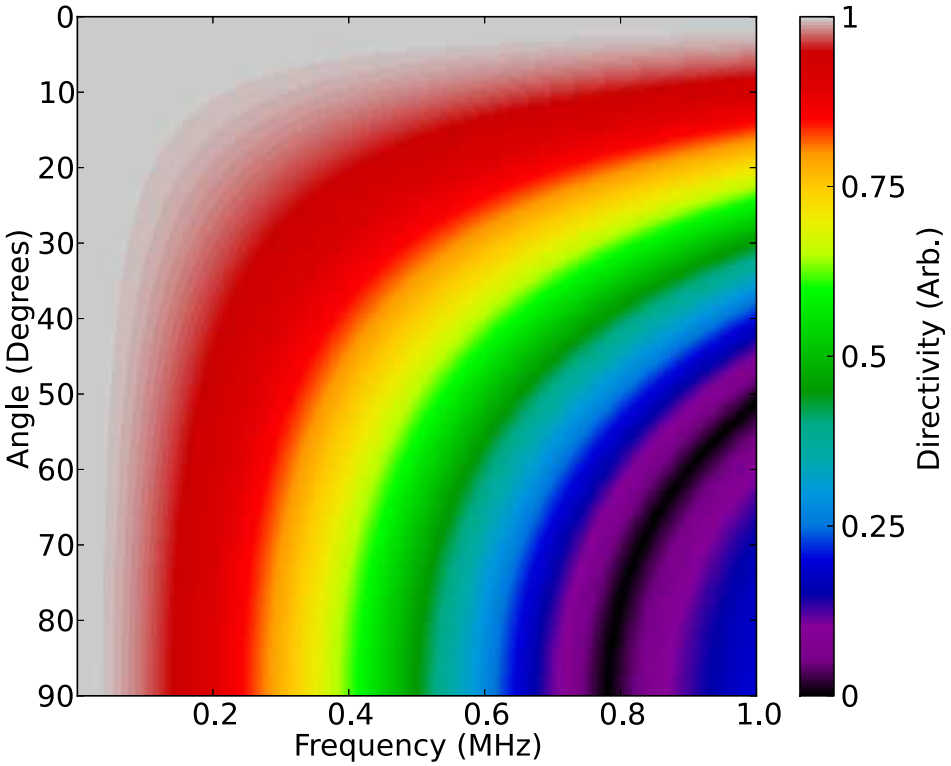

Figure 5.6: The frequency dependence of the directivity of a 4 mm source that is generating shear waves in aluminium.

to an angle where the ultrasound can be efficiently generated. So, the constructive interference that leads to the variation in frequency acts in a way that minimised the problems associated with the directivity characteristics of the array elements.

The directivity of the array elements also has the useful effect of suppressing higher order diffraction modes that may be activated if the frequency content of the excitation pulse is not selected with enough care. For the 5 mm pitch array, the next order diffraction mode is activated at 933 kHz. However, the angle at which this mode activated is at 90°, and the directivity function of a 4 mm element is near a minimum at this angle for 933 kHz. In general, the higher order modes will be at least three times the frequency than the lowest order mode, and hence the source will act much more uni-directionally at these frequencies, when compared the the lowest order mode. Consequently, the amplitude of higher order diffraction modes will be greatly reduced.

5.5 Conclusions

Finite element modelling was used to develop a numerical model to fully investigate the behaviour of the pulsed wavefront. After obtaining a physical understanding from the analytic model, the more numerically intensive finite element analysis was used in order to create a more realistic model, which can include other parameters not included in the analytic model. The FE model was used to model the effect of having an array comprised of elements with finite size. The FE approach can be used to model the wavefield generated array in complex geometries, as well as being able to simulate the interactions of the wavefield with an arbitrarily shaped discontinuity.

The FE models confirm the behaviour seen in the analytic models, with a wavefront covering a large angular region, which has a variation of the peak frequency as the angle of propagation changes. The variation in frequency is also inversely

proportional to the sine of the angle of propagation, as was seen with the analytic model. However, there are subtle variations between the peak frequencies predicted by the FE model when compared to the analytical model; namely that the peak frequencies are slightly lower in the FE model than the analytic model. It was shown in section 5.4 that this deviation can be explained by considering the finite size of the elements that constitute the array. Unless the array elements are much smaller than the wavelength that is being emitted, they no longer emit the ultrasonic energy equally in all directions. This directionality becomes more pronounced as the ratio between element size and wavelength increases. Therefore, for a fixed element size, the generated wavefield is more directional as the frequency is increased. This means that whilst all frequencies can be emitted equally effectively at 0°, the lower frequencies are generated with more efficiency at all other angles, with the difference becoming more pronounced as $\theta \rightarrow \pm 90°$, with the directivity for a rectangular aperture given by equation 3.15. Hence, as the lower frequencies can be generated with greater efficiency, the observed peak frequency at a particular angle is slightly lower than would be expected from the diffraction grating equation. So, the generated wavefront is a convolution of the spatial periodicity of the array and the spatial impulse response of the array elements, which can be calculated from information about their shape.

However, the discrepancy between the FE models and the diffraction grating equation is generally quite small, typically less than 3%. This is because of the inverse proportionality of peak frequency and the angle of propagation. The higher frequencies, for which the array elements act increasingly uni-directionally, are steered to the lower angles, where the directivity effects are less pronounced. The directivity of the array elements also has some useful benefits, as it suppresses the higher order diffraction modes, which will be at least three times the frequency of the fundamental mode.

The FE model was constructed in order to create a more realistic model of the

pulsed array. It was found that the size of the elements has a small effect on the frequency of wavefront by reducing it because of the directivity behaviour of elements with a finite size. However, the FE model also has the advantage of being able to be extended to a more complex and arbitrarily shaped geometry. Therefore, not only can it be used to gain more information about the generated wavefront, it can also be extended to model how the wavefront interacts with any discontinuities.

Chapter 6

Experimental Verification of Frequency Dependent Directivity

As well as creating theoretical models, it is also important to obtain experimental verification of these models. This section will describe the experimental procedures used to acquire the data that confirms the behaviour of the frequency dependent directivity of the pulsed array. Firstly, the frequency variation of the pulsed wavefront is measured, and it is demonstrated to behave as expected from the models constructed. The ability to steer ultrasound to a particular angle is also demonstrated as the array is excited with a narrowband signal, causing the ultrasound from the array elements to constructively interfere at an angle given by the diffraction grating equation.

6.1 EMAT Construction

6.1.1 PPM Array

The experiments were performed using a PPM EMAT, as shown in figure 2.6, to generate ultrasonic SH waves. The PPM EMATs were used to generate SH waves into aluminium, so that the obtained results are directly comparable with the models

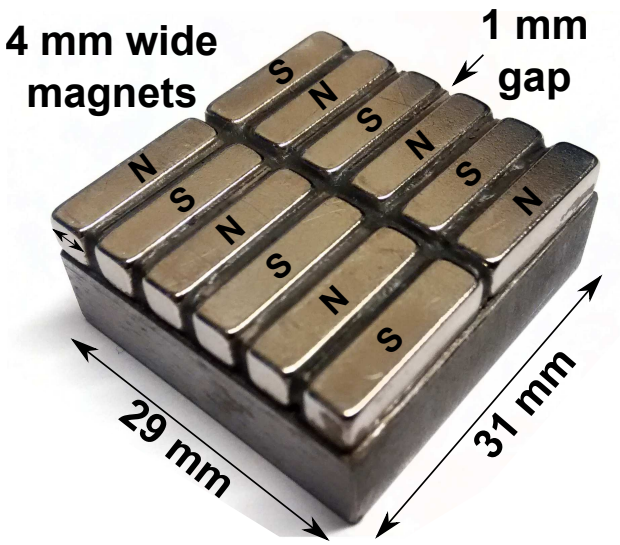

Figure 6.1: Image of an experimental magnet array, with the polarity written on the magnets. The 4 mm wide magnets are separated by 1 mm of alumina ceramic spacer.

in Chapters 4 and 5. For aluminium samples, which are used exclusively in this section, the EMATs generate and detect ultrasound via the Lorentz mechanism [38, 71, 95, 185]. The PPM EMAT is comprised of six elements, each 4 mm wide, with the pitch of the array being 5 mm. This means that the wavelength of the ultrasonic wave generated on the surface of the sample is 10 mm - corresponding to a frequency of 311 kHz for a shear wave in aluminium.

As seen from figure 2.6 and figure 6.1, the array does not simply just consist of six magnets, but consists of six rows of two neighbouring magnets. The polarity of the magnets in the array alternate with respect to the nearest neighbour. This alternating behaviour ensures two things. Firstly, it guarantees that the EMAT array will have an alternating structure, with the elements in the array being the opposite polarity to its neighbour. This will create an array structure that can only support odd-numbered diffraction modes, and therefore extends the angular region over which the array can operate, as discussed in Section 4.4. The intra-row alternation of polarity is due to the construction of the racetrack coil, which carries the excitation signal. As the direction of the current reverses as the coil spirals around, the direction of the magnetic field must also reverse, so that the Lorentz

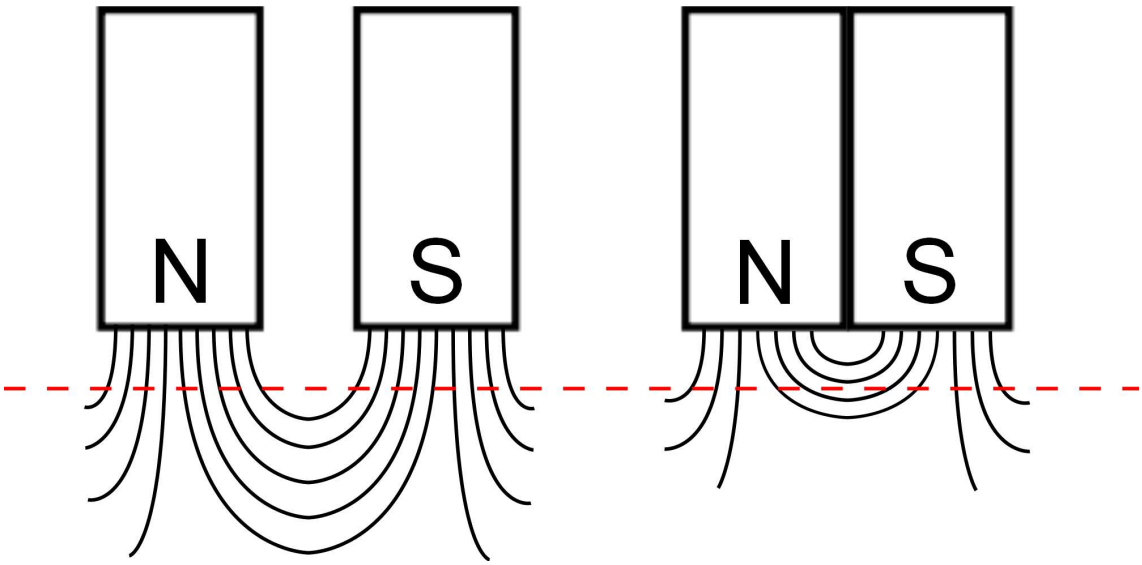

Figure 6.2: A comparison between the magnetic fields produced with two magnet configurations; one with a spacer between the magnets, and one with no spacer. The air/aluminium interface is shown as a horizontal dashed line.

force acts in the same direction along the length of the element. The magnets are separated by alumina ceramic spacers, which are used to create a 1 mm gap. These spacers are designed to not only improve the directivity performance of the array, but also to improve the lift-off performance of the EMAT. By creating a gap between the magnets in the array, it reduces the magnetic field 'shorting' across to the neighbouring magnet, as is shown schematically in figure 6.2. This ensures that the magnetic field vectors are still perpendicular to the sample surface, even if the EMAT is lifted away from the sample surface. If the magnets are close together, the magnetic field vector is parallel, rather than perpendicular, to the surface, and will therefore not generate SH waves. Lift-offs of a few millimetres were still found to achieve appreciable signal, although the lift-off was always minimised as generation efficiency greatly diminishes as the EMAT is moved away from the sample.

The wire used to create the racetrack coil depends on whether the EMAT is used to generate or detect ultrasound. For the generation EMAT, the diameter of the wire (including insulation) is 0.28 mm, whereas the diameter of the wire used for the reception EMAT is 0.2 mm. The generation EMAT will be excited with high

current levels, in order to generate ultrasound with a high enough intensity. Due to this, the wire carrying this current needs to be large enough so that the current density is not too high, as this will lead to Ohmic heating. So, in order to reduce the heating effects and thermal expansion of the wires, thicker wires should be used for generation EMATs. Such considerations are not required for the detection EMATs, as the current levels are much smaller. Hence, in order to maximise the number of turns and the sensitivity of the EMAT, a thinner wire is used. However, this improvement is limited. If the wire is made too thin, then the resistance and the inductance of the coil will increase, which will lead to a reduced bandwidth.

6.1.2 Linear Coil EMAT

As well as using a PPM EMAT to detect ultrasound, a linear coil EMAT, configured to be sensitive to SH waves, was also used. The EMAT, shown in figure 6.3, was used as it has a small physical size; meaning that the EMAT does not average the signal over a wide spatial range. As the small size of the EMAT limits the amount of spatial averaging, it can be used to make point-like measurements to see how the wavefront varies as a function of angle. However, as the coil width is limited to 3 mm, the detection efficiency of the EMAT is quite low. Hence, many turns (approximately 200) are needed so that the EMAT has adequate sensitivity. The diameter of the wire used to create the linear coil was 0.08 mm, with the total length of the coil being 17 mm. The coil is wound around a plastic former, which is covered in 0.5 mm thick copper tape. This copper tape, which is also grounded to the protective brass case that contains the EMAT, acts to electrically shield the top of the coil from the bottom. If the top of the coil was not shielded, current would be induced, which would oppose the current induced from the bottom of the coil; thereby reducing the overall signal. From the coil geometry and the direction of the magnetic field, it can be seen that this EMAT will be sensitive to waves of the same polarisation as those generated by the PPM EMAT, so that it can be used to detect

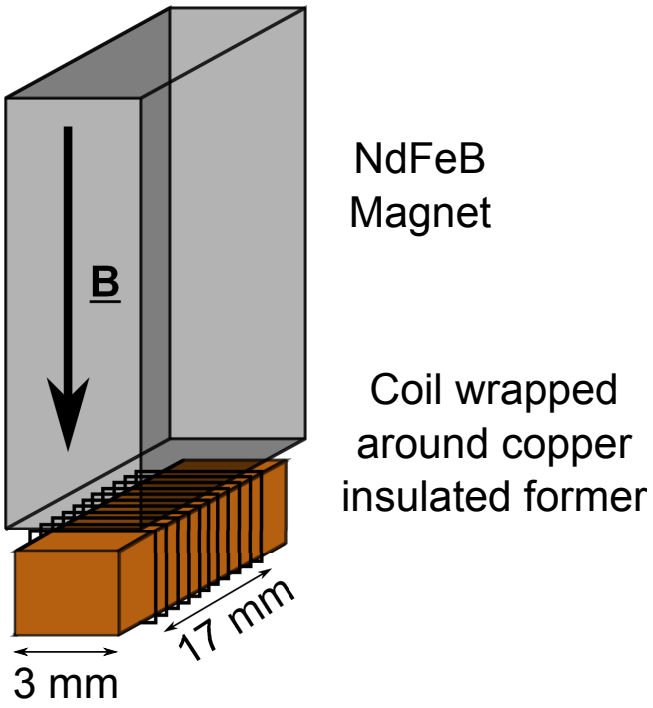

Figure 6.3: Schematic diagram of the linear coil detection EMAT.

SH waves.

6.1.2.1 Frequency Dependence of Linear Coil EMAT

As has been seen from Section 5.4, the finite size of a wave emitter can affect the frequency response of the transducer, so that it cannot emit waves of all frequencies omnidirectionally. The same also applies to receivers, with the size of the transducer limiting the frequency bandwidth that it is sensitive to. Of course, the exact construction of the EMAT, such as the number and configuration of coil turns, also has an effect on the frequency response of the EMAT. The change in the coil configuration can alter the inductance and therefore the impedance of the coil, which will have an effect that depends on frequency [185]. However, these effects are neglected here and only the effect of the size of the transducer is considered. Also, as before, the problem is considered in only two dimensions as the length of the linear coil EMAT is several times the width of the coil.

In a similar fashion to the way the directivity of the elements is considered for the

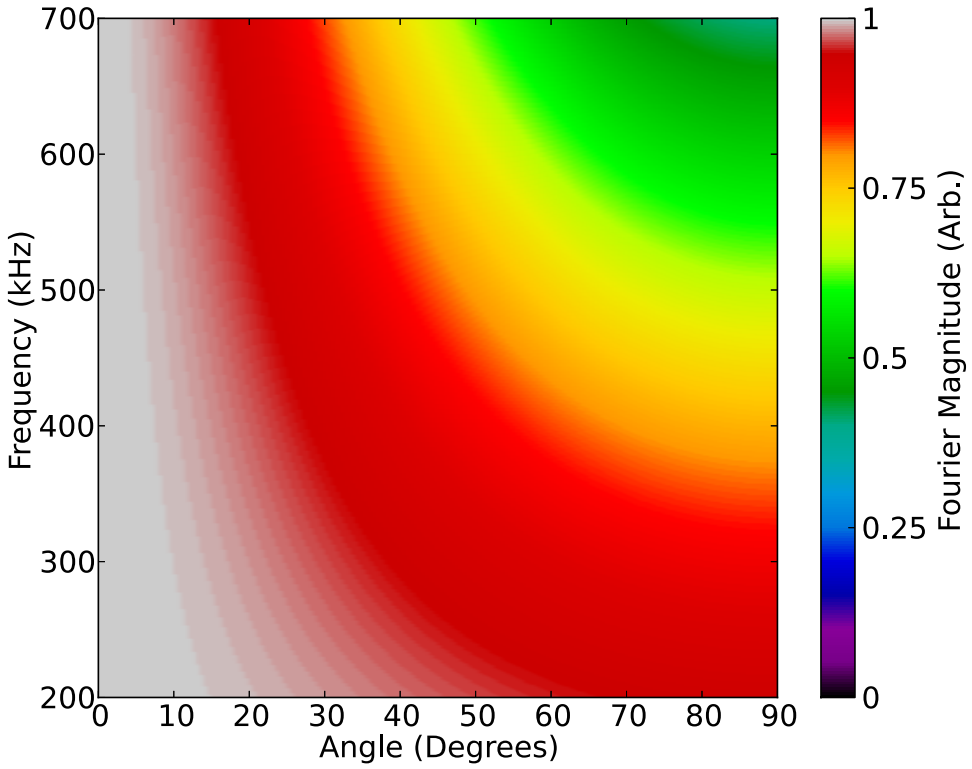

Figure 6.4: The far-field directivity of a 3 mm linear coil detecting SH waves operating in aluminium

generation of the pulsed wavefront, the frequency response of the detection EMAT can be considered as being a spatial filter. Assuming that the incoming signal can be approximated as a plane wave (either because the detector is far away from the source, or the detector is small, so that any phase differences are negligible), the result reduces to that obtained in equation 3.15. The spatial impulse response for a 3 mm linear coil, detecting SH waves in aluminium is shown in figure 6.4. For waves impinging normally to the detector, so that the wave is approaching at 0°, the linear coil can detect all frequencies equally. As seen for the wave emitter, the linear coil becomes less efficient at higher frequencies as the angle that the wave approaches the detector increases. Figure 6.4 shows the inherent frequency response of the detector, which can be used to simulate the effect on the measured frequency of a signal.

The recorded signal will be a convolution of the spatial impulse response of the transducer, shown in figure 6.4, and the signal that is to be measured. In the frequency domain, this convolution becomes a simple multiplication of the two spectra as a consequence of the Fourier convolution theorem [33]. For an acoustic source that is 50 mm below the surface of an aluminium bar, the signal recorded from various points along the surface can be simulated. This is demonstrated in figure 6.5, where a simulated 400 kHz shear wave is measured over a range of 150 mm on the surface of the bar, starting directly above the source and then moving away from the source in 1 mm increments. As the position along the sample, and hence the angle of the transducer relative to the source, increase, the measured frequency of the wave decreases. At 0°, when the detector is directly overhead the simulated source, the wave is correctly measured as a 400 kHz wave. However, as the angle between the transducer and the source increases, then the projected size of detector decreases and the impulse response of the detector is more frequency dependent. This leads to the frequency spectrum, as well as the peak frequency, of the recorded signal being shifted to a lower frequency. For this set up, at 150 mm, the measured peak frequency is 390 kHz. Despite the measured frequency slowly varying over a large region, care must still be taken when measuring the frequency of a wave using a transducer with a finite width. The error in determining the true frequency of the wave increases when the wavelength of the wave becomes comparable with the width of the linear coil, or when the angle between the wave source and detector is large. Ideally, the coil width should be no larger than half the wavelength as, at this point, the sensitivity of the detector has dropped to 50% of the maximum and will continue to decrease as the detector size becomes even more comparable with the wavelength [186].

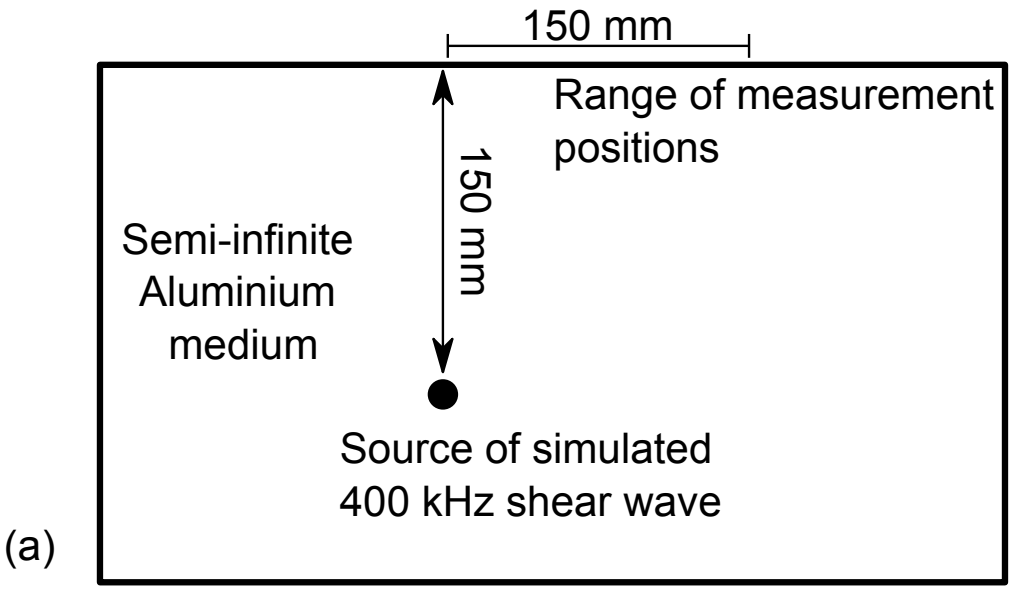

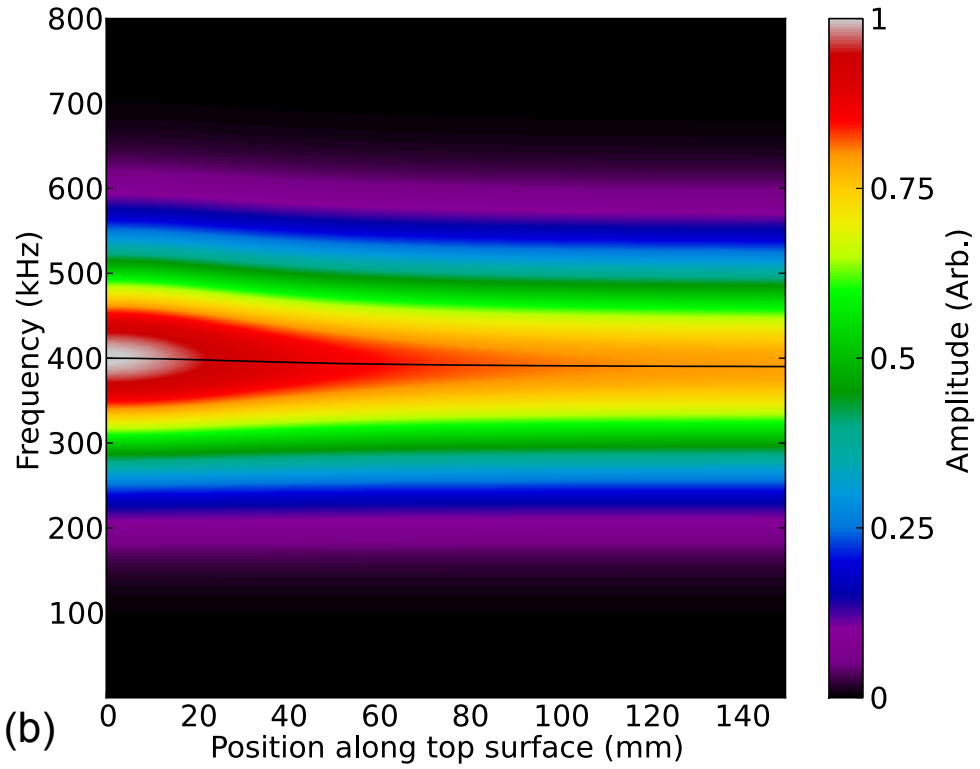

Figure 6.5: (a) Schematic diagram of the simulation that investigates the effect that a finite size reception transducer has on the measured frequency of a wave. A point source, which is generating a 5 cycle, 400 kHz shear wave, is 150 mm below the surface. This wave is 'measured' with a 3 mm wide detector, which is moved over a 150 mm range along the top surface. (b) Frequency content of recorded signal at various positions along the top position of the sample. The peak frequency of the signal is marked with a black line over the plot.

6.2 Experimental Set-up

The experiments performed in this chapter are to investigate the frequency dependence of the directivity of PPM EMATs. Consequently, the aluminium sample used in these experiments is semi-cylindrical, so that the curved surface of the sample can be used to make measurements of the wavefield over a range of angles. This is shown in figure 6.6, which shows the location of the PPM EMAT, as well as the linear coil EMAT that was used to detect the generated SH waves. The linear coil reception EMAT can be moved along the curved edge of the semi-cylindrical sample, to make a measurement at a particular angle, θ. As the coil width of the EMAT is only 3 mm, the angular resolution is optimised as there is not too much spatial averaging of the signal over a range of angles. Also, due to the curved surface of the aluminium sample, the ultrasound is always normally incident to detector, and so the directivity of the linear coil is not particularly frequency dependent. Hence, the frequency of the measured wave will not be significantly altered due to the directivity.

The array is driven by a Ritec RPR-4000 pulser receiver unit, which controls the excitation of the array, as well as the filtering and amplification of the received signal. The Ritec unit is capable of creating high powered, tone burst pulses, with the frequency and number of cycles being able to be controlled. The maximum excitation frequency that the Ritec is capable of producing - 21 MHz - is much higher than is required for these experiments. It also has a low noise, broadband (50 kHz to 20 MHz) receiver amplifier, which can be used in conjunction with a separate receiving transducer, or with the original generation transducer using an internal diplexer. For this work, the linear coil reception transducer was connected to the receiver amplifier. The receiver amplifier gain and band-pass filter gain can be selected, with a range of options available. For all of the experiments in this chapter, the amplifier setting was set with a gain of 80 dB, with the passband of the bandpass filter set to 200 kHz - 1.6 MHz. The signal, after being bandpass filtered and amplified, is then captured on a digital oscilloscope for signal processing.

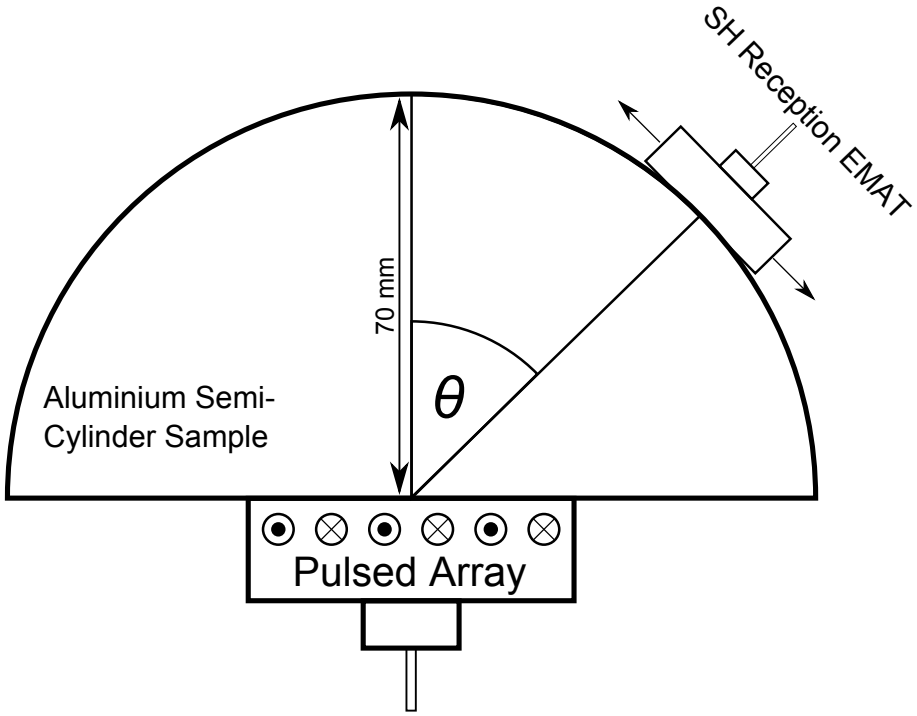

Figure 6.6: Experimental Layout, with the pulsed array on the bottom of the aluminium sample and the linear coil EMAT used to angularly resolve the wavefront after it had propagated through the sample.

Coherent averaging (32 averages) was also used to improve the signal to noise ratio of the obtained data.

However, it has been shown that EMATs are, in fact, velocity sensors [7, 187], whereas all of the models have considered the displacement field generated by the array. Hence, the signals obtained from the EMATs must be integrated in order to recover the displacement field. The distinction between a wideband signal and its derivative is important when considering the frequency content of the signal. This can be seen from the relationship between the Fourier transform of a signal and the Fourier transform of its derivative [33, 102, 186],

$$\mathcal{F}\left(v\left(t\right)\right) = \mathcal{F}\left(\dot{x}\left(t\right)\right) = i\omega X\left(\omega\right). \tag{6.1}$$

Hence, the Fourier spectrum of a derivative is shifted by a linear factor of frequency with respect to the Fourier spectrum of the original signal. This linear factor

of ω will act to increase the peak frequency of the signal. Thus, in order to directly compare the displacement models calculated in Chapters 4 and 5, the obtained EMAT signal must be integrated [102]. As the recorded signal may also contain other features, such as the generation signal or any secondary reflections, the signal of interest was isolated by windowing over the region of first arrival. The appropriate data processing could then be implemented in order to extract the desired information.

6.3 Frequency Variation of Pulsed Array Wavefield

The peak frequency predicted by the models was expected to vary in inverse proportion with the sine of the angle of propagation. In order to examine whether this predicted frequency variation is indeed accurate, it was tested by using the PPM EMAT. In order to create a pulsed array wavefront, as has been seen before, the EMAT needed to be excited with a broadband pulse. Hence, the array was excited with a single cycle sine wave, with a nominal frequency of 450 kHz, as shown in figure 6.7. A single cycle is the shortest pulse that it is possible generate with the Ritec unit, and has the desired broad bandwidth. The frequency of 450 kHz was selected as it was at the midpoint of the desired frequency range, and will thus ensure that there is significant frequency content over the desired range, as shown in figure 6.8. As the signal is restricted in time, there will also be some energy leaking to the higher frequency components. These are seen in figure 6.8 as smaller amplitude side lobes that peak at 1.1 MHz, 1.55 MHz and 2 MHz.

The data, recorded using the linear coil EMAT over a range of angles, was preprocessed as discussed in section 6.2. The processed data was then fast Fourier transformed in order to reveal the frequency content of the signal. As with the analytic and FE models, the peak frequency component was extracted from the

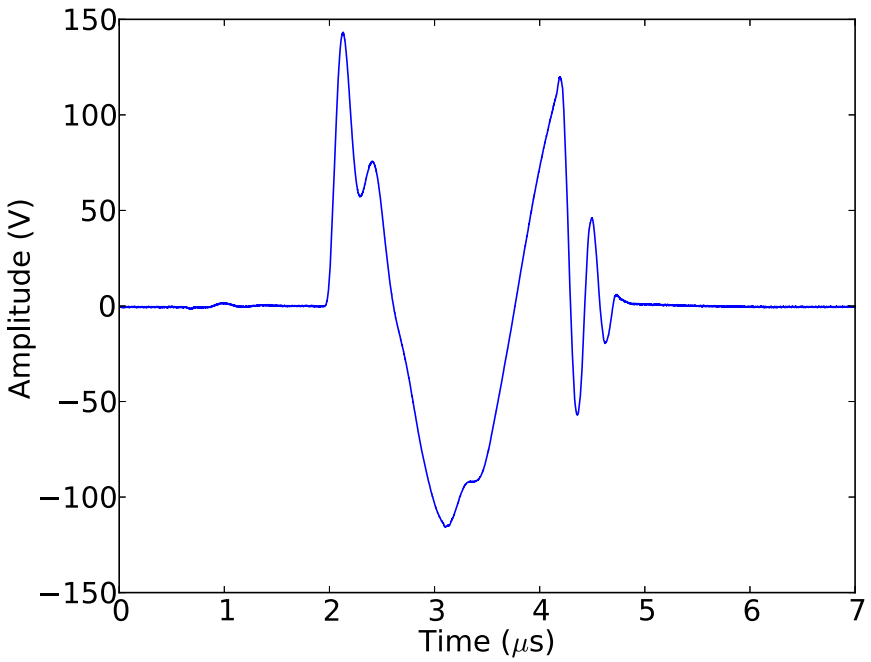

Figure 6.7: Broadband excitation signal obtained from Ritec pulser-receiver unit, selecting a single cycle 450 kHz signal. The signal was obtained across a 0.8 Ω resistor.

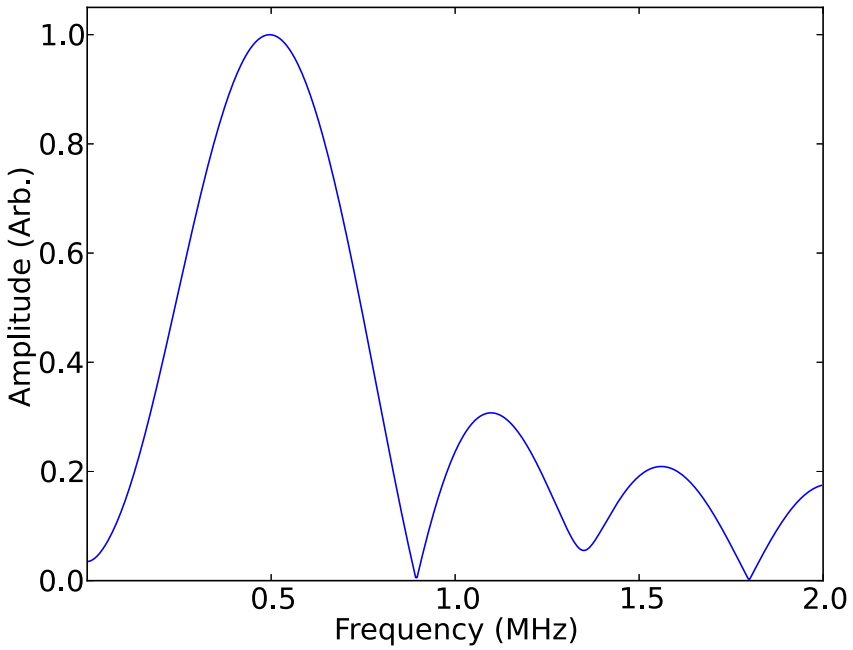

Figure 6.8: Frequency content of broadband excitation signal, shown in figure 6.7, with the spectrum peaking at 495.9 kHz. Side lobes can also be seen at higher frequencies as a consequence of the short temporal length of the signal and the resultant spectral leakage.

spectrum. The variation of peak frequency of the wavefront generated from the PPM EMAT, as a function of the angle of propagation, is shown in figure 6.9. The variation of frequency is again proportional to $1/\sin\theta$, demonstrating that the models that were constructed are representative of the physical wavefront. The variation in peak frequency is also compared with the values predicted by the diffraction grating equation.

There are, again, small differences between the behaviour expected from the diffraction grating equation and the variation of peak frequencies measured from the wavefield generated by the PPM EMAT. These differences can be explained by considering the finite size of the array elements, and the resultant directivity of these elements. The difference between the experimental peak frequency and the diffraction grating increases as θ tends towards $0°$. Due to the inverse proportionality between the peak frequency and $\sin\theta$, the frequency changes more rapidly at lower angles. Therefore, although the deviation from the diffraction grating equation at lower angles is larger, this will not lead to a significant variation in the estimation of the angle of propagation. Also, these deviations are even smaller than seen with the finite element model. The mean error between the experimental data and the expected diffraction grating relationship is 0.6% of the experimental value, with the maximum discrepancy only 1.8%. It should also be noted that the measurements were taken at 70 mm, and hence were not taken in the far field of the array, which is given by the Fraunhofer distance as 170 mm. The diffraction grating equation assumes that all of the individual contributions of each element are parallel to one another, and is therefore a far field solution. However, the agreement between the experimental measurements and the diffraction grating equation are very good, despite the measurements being taken within the Fraunhofer region, which is the limit between near- and far-field.

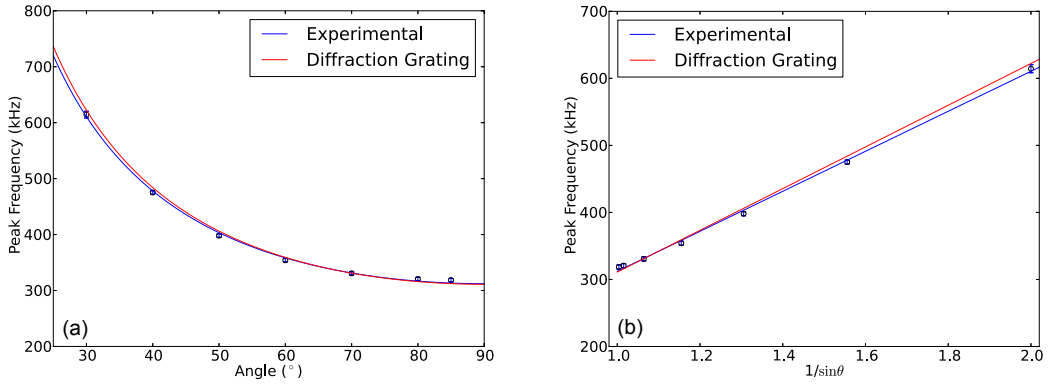

Figure 6.9: Experimental data showing the angular dependence of the centre frequency of the wavefront. It shows the deviation of the measured peak frequency compared to the diffraction grating equation.

6.4 Frequency Steered Arrays and frequency dependent directivity

In addition to demonstrating the frequency variation of the pulsed array wavefront, the frequency dependent directivity of PPM EMATs can also be confirmed by exciting the array with a narrowband signal. This time, the EMAT was excited by a 5 cycle pulse, shown in figure 6.10, so that had a much narrower frequency bandwidth, with an example spectrum shown in figure 6.11. By varying the frequency of the excitation signal, the generated ultrasonic beam is steered over a large range of angles, as described by the model in Chapter 3. A single ultrasonic beam can be generated and steered in the angular range $20° \leq \theta \leq 90°$, with higher order diffraction beams being generated if the beam is steered below 20°. For a 5 mm pitch array being used on an aluminium, the beam can be steered between an angular range of $30° - 90°$ by driving the array with a frequency between 311 kHz and 622 kHz. Therefore, the array was driven at 350 kHz to 650 kHz in steps of 100 kHz.

The linear coil EMAT was used to measure the generated wavefront at intervals of 5°, so that an acceptable angular resolution could be obtained. The data obtained was processed in the same way as described in previous sections; coherent

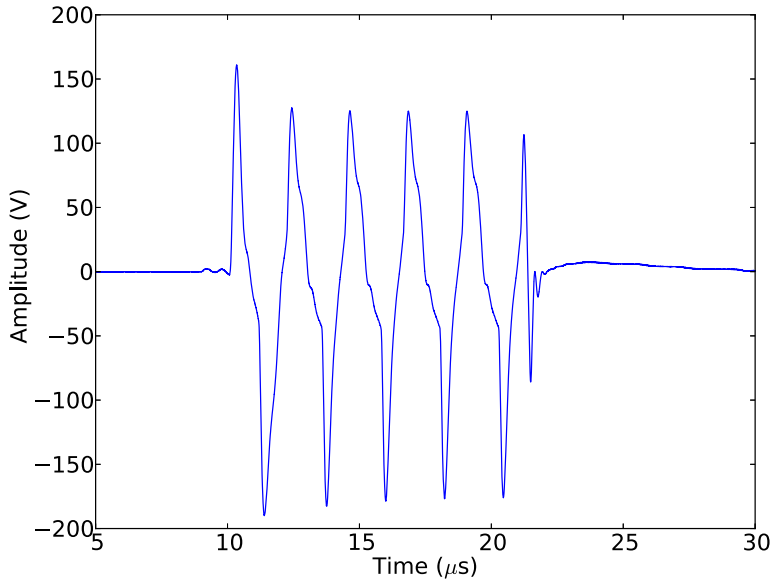

Figure 6.10: Tone-burst excitation signal obtained from Ritec pulser-receiver unit, selecting a 5 cycle 450 kHz signal. The signal was obtained across a 0.8 Ω resistor.

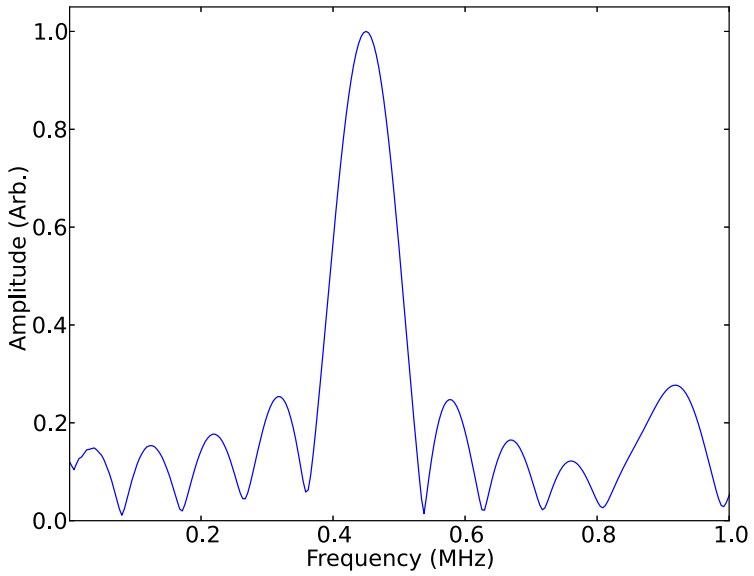

Figure 6.11: Frequency content of narrowband excitation signal shown in figure 6.10. The peak position was measured to be 450.1 kHz, and the second harmonic of the generation signal can be seen at around 900 kHz.

averaging, integration, filtering and time-windowing. For each excitation frequency, the peak-to-peak amplitude of the windowed signal was calculated, and used as a measure of the intensity of the wave at a given angle. The angular distribution of the peak-to-peak amplitude of the wavefront forms the directivity of the wavefront, and demonstrates how the directivity of the array changes with frequency. The finite element model, described in Chapter 5, was modified so that the array underwent narrowband excitation in order to directly compare the FE results with those obtained from the experiment. The amount and precision of the angular measurements that can be obtained from the FE model is much higher than can be achieved with experimental measurements. Furthermore, the directivity predicted from the frequency domain model described in Section 3 is also shown to allow for direct comparison between the model, FE results and experimental data. In each case, the results are shown in arbitrary units, having being normalised to the maximum value, to remove the effects of different amplitude excitation signals. The results are shown in figure 6.12.

The frequency dependence of the array's directivity can be clearly seen in both the finite element, shown by the green data points, and experimental results, shown in red. The radial error bars represent the uncertainty in determining peak-to-peak amplitude of the wave after repeat measurements, whilst the angular error bars are associated with the crude approach of manually placing the EMAT onto the sample to make the angular measurements. The directivity predicted by the frequency-domain model described in Chapter 3 is plotted in blue. Clearly, as well as the peak position of the steered beam changing, the width of the beam also varies. As the generation frequency is increased, not only does the ultrasound get steered to a lower angle, but the width of the beam is also greatly reduced. This means that the ultrasound is being steered much more tightly, so that the benefits of steering the beam, such as improved lateral resolution and signal-to-noise, become more pronounced. This tighter steering is a consequence the inverse proportionality

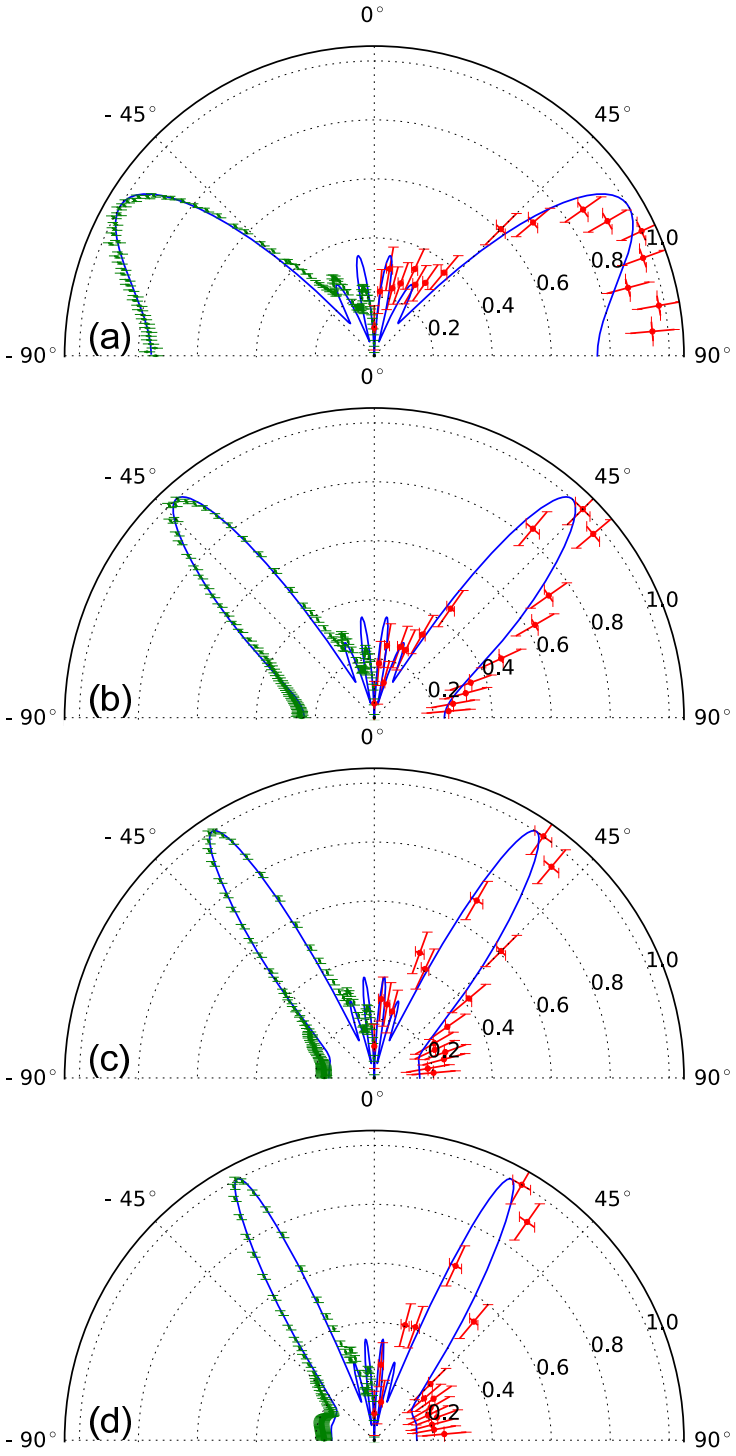

Figure 6.12: Directivity measurements for a size element, 5 mm pitch array being driven by a five cycle sine wave with frequency of (a) 350 kHz, (b) 450 kHz, (c) 550 kHz, (d) 650 kHz. The experimental data are shown on the right-hand side of each polar plot, whilst the finite element simulation results are shown on the left-hand side, and the directivity predicted by the frequency domain model is shown in blue.

between frequency and angle. In the lower angular range, the rate of change of the frequency is higher, and for a given bandwidth, the frequency is distributed in a much narrower angular band than if the beam was being steered closer to the surface, where the energy is spread out more diffusely.

Artefacts associated with the limited steering range of this approach can start to be seen in figure 6.12, when the array is being driven with a 650 kHz excitation pulse. Although the centre frequency of this pulse is below the threshold for generating a higher order diffraction mode, the bandwidth of the signal is sufficiently large that there is a significant amount of energy above the frequency threshold for the generating third order diffraction, 933 kHz. This higher order diffraction mode can be seen at around 70° as a slight deviation in the directivity plot, and is most notable in the FE data. However, this additional lobe only has a small amplitude when compared to that of the main beam. This can be partly explained by the relative amplitudes of the energy in the signal at the respective frequencies, with much more of the signal energy being at 650 kHz than at 933 kHz . Further to this, the finite size of the elements that constitute the array also act to suppress the higher order lobes. The wavelength of a 933 kHz shear wave in aluminium is 3.3 mm. This is over 80% of the size of the 4 mm elements, meaning that instead of acting as an omnidirectional source, the elements act highly directionally. Consequently, this reduces the amount of energy that is transmitted to the higher angles, further reducing the amplitude of the higher order diffraction lobe. Despite this, however, if the frequency of the excitation pulse is high enough, then higher order diffraction modes can still be generated with significant amplitude. So the angular limit of the frequency steering capability of PPM EMAT is still valid, and care must be taken not to exceed this range.

6.5 Conclusion

Experimental verification of the pulsed array phenomenon is demonstrated in this chapter. The pulsed array, realised using a PPM EMAT, exhibits the same key behaviour as predicted from the theoretical models. By electromagnetically coupling to the aluminium sample, it can generate SH waves. This EMAT was constructed so that it consisted of six rows of magnets, and therefore can be considered as a six element array. This six element array is pulsed with a broadband signal from a high powered pulser-receiver unit, and the signals from each individual elements interfere to create a wavefront that extends over a large angular region. The experimentally measured frequency variation of this wavefront is in agreement with both the analytic and finite element model. The experimental data confirms that the analytic model captures the underlying physics of this phenomenon; that it is inherently an interference effect, and the array can be thought of as a diffraction grating, but with an alternating polarity structure, that is being illuminated with a broadband signal. This can be seen from the variation of the measured peak frequency of the wavefront, as a function of the angle of propagation. As with the FE results, the measured frequencies are slightly below those predicted by the diffraction grating equation, however this discrepancy can be explained by considering the directivity of the array elements.

The narrowband directivity of the array is also examined, and it is shown that by exciting the array with a much smaller bandwidth signal, the generated ultrasound is steered in a beam to a particular angle. This steering angle can be controlled by simply varying the frequency of the narrowband signal, with the relationship between angle and frequency the same as can be seen for the pulsed approach. It should be noted that this approach eliminates the need for more complex phased array equipment with independent channel capabilities, as the steering is achieved by simultaneously exciting the array elements. The experimental directivities agree well with the models constructed in Section 3.

As the frequency dependence of the directivity is now well understood, the phenomenon can be exploited for use in locating the position of defects. The ability to steer the ultrasonic beam can lead to the opportunity to locate any discontinuity that may scatter the ultrasound, as well as the possibility of creating ultrasonic images. For example, by changing the excitation frequency and steering the ultrasound over a range of angles, it is possible to create a sector scan image; showing two dimensional information about the position of any defects that may be present. A similar principle can be utilised with the pulsed array. Using the variation of the peak frequency, the location of a discontinuity can be found with a single measurement. This is because the frequency of the scattered wave will encapsulate the angular position of the defect, whilst its radial position can be determined from the time of flight. This is discussed in more detail in Chapter 7.

Chapter 7

Localisation of defects using combined time-frequency measurements

It has been demonstrated that the pulsed array exhibits a number of interesting physical phenomena, including a frequency dependent angle of propagation. This novel feature of the wavefront can be exploited for practical purposes, in order to ultrasonically inspect a sample. Specifically, the frequency dependent directivity of the wavefront can be used to extract information about the angular position of any discontinuities that may be present in a sample. As the wavefront propagates through a sample, it will be scattered by defects due to the acoustic impedance mismatch between the two regions. The frequency of this scattered wave depends upon the angular position of the defect relative to the centre of the array, whilst the time of flight of the measured reflection can be used to calculate the radial position of the defect. Consequently, it is possible to locate the position of a defect with just a single measurement, which is not possible when just considering the time of flight information, as with traditional ultrasonic inspection methods.

Experimental measurements, supported by finite element simulations, are presen-

ted in this chapter to demonstrate and verify these principles. The localisation of a defect through a combined time and frequency measurement approach is demonstrated using a range of techniques, and on a multitude of samples. Firstly, PPM EMATs were utilised, as in Chapter 6, to generate a pulsed array wavefront, which was used to inspect several aluminium samples. Different arrangements are also used, with both pulse-echo and pitch-catch configurations being implemented. Initially, pitch-catch, with a separate SH wave reception EMAT, was used to detect and locate the presence of circular side-drilled holes. A single PPM EMAT, used in a pulse-echo configuration, is also used to create two-dimensional maps of samples, showing the locations of any defects present.

As the frequency variation of the pulsed wavefront generated by PPM EMATs is now well understood, it can be exploited to localise a defect. Whilst various methods of utilising PPM EMATs will be utilised, there are some aspects of the methodology that are universal to all of the PPM measurements. Notably, the Ritec RPR-4000 pulser receiver unit, as in Chapter 6, is used to pulse the PPM EMAT to generate the wavefront, as well as amplifying and filtering the received signals. As the Ritec parameters, including excitation frequency, will depend upon the specific EMAT used, they will be given in the relevant sections below. Aluminium samples are used in this work owing to their high conductivity, which leads to high coupling efficiency between EMAT and sample.

7.1 Aluminium Side-drilled holes

The ability of the pulsed array to use a combination of time and frequency measurements is first demonstrated on side-drilled holes in an aluminium sample. The sample geometry, including the positions of the relevant transducers, is shown in figure 7.1. In this experiment, two transducers are used in a pitch-catch configuration; a PPM EMAT is employed to generate the wavefront, whilst a separate,

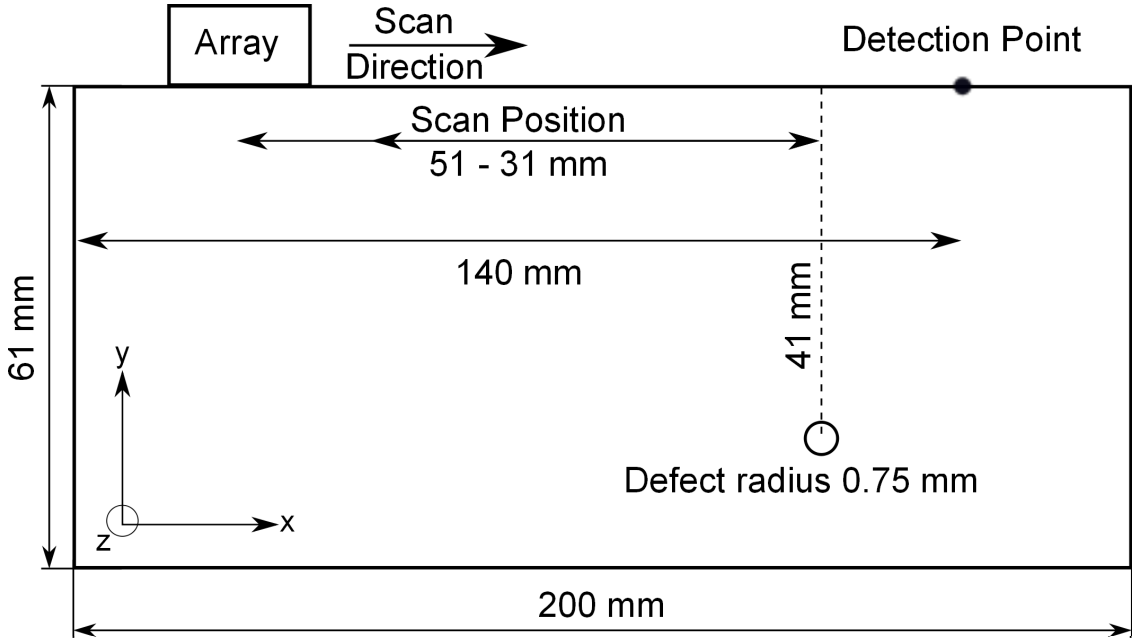

Figure 7.1: Experimental geometry for pitch-catch experiments.

linear coil EMAT is utilised to detected the reflected and scattered ultrasonic waves. The advantage of using a separate reception transducer is that it breaks the symmetry associated with just using a single transducer. Due to the symmetry of PPM transducers, two waves are generated, travelling in two opposite directions to each other. Consequently, with a pulse-echo measurement, it is not possible to ascertain from which direction the scattered signal originates. By using a second transducer, that is in a different location to the PPM EMAT, the symmetry of this situation is broken. Defects with the same radial distances from the centre of the PPM array, but opposite angular positions $\pm\theta$, will have the same frequency but different times of flight in this case. In addition, as the PPM arrays are constructed with an even number of elements, the generated wavefront is antisymmetric about $\theta = 0°$ [101]. Therefore, by considering this phase shift, another means of differentiating between defects on either side of the array can be found.

A 3 mm pitch PPM EMAT was constructed, using the same principles described in section 6.1.1. The array consisted of six elements, which had a width of 2.5 mm. These magnets were separated by ceramic spacers, with a width of 0.5 mm, in order

to create the 3 mm pitch PPM EMAT. A smaller, and therefore higher frequency, array was required due to the limited spatial extent of the test sample; it was found that the scattered signal was not resolvable if a lower frequency array was used, due to the longer temporal extent of the signals. In aluminium, the frequency of a shear wave with a wavelength of 6 mm (corresponding to the spatial periodicity of the PPM EMAT) is 518.5 kHz. Consequently, the excitation signal used with this array must have significant frequency content between 500 kHz and 1.1 MHz in order to generated a wavefront that covered the maximum possible angular range of $20° \leq \theta \leq 90°$. A single cycle pulse, with a nominal frequency of 800 kHz, was found to have sufficient bandwidth to generate the wavefront over the entire angular range.

Once the wavefront is generated, it will propagate until it is disturbed by the boundary of the sample, or it is scattered by, or reflects off, the circular side-drilled hole (SDH). The SDH will scatter a portion of the wave which encapsulates its angular position through the frequency of the scattered wave. A linear coil EMAT is used to detect the ultrasonic signals, with the width of the coil made to be as small as possible (3 mm), in order to reduce the effects of spatial averaging and the frequency dependent directivity. The detected signals are then band-pass filtered and amplified by the Ritec hardware, before the data are displayed and recorded using a digital storage oscilloscope. A hardware band-pass filter, with a passband between 400 kHz and 1.6 MHz, is used to remove all unwanted frequency components from the signal. The signal is then amplified by an internal broadband amplifier, with an adjustable gain, so that the voltage level is sufficiently high to be digitised by the oscilloscope; in this instance, it was achieved by applying 74dB of gain. Coherent averaging of 64 samples was also used to improve the signal-to-noise ratio of the measurements, which was required due to the small amplitude of the scattered signal.

As was discussed in section 6.2, EMATs are velocity sensors and the relationship

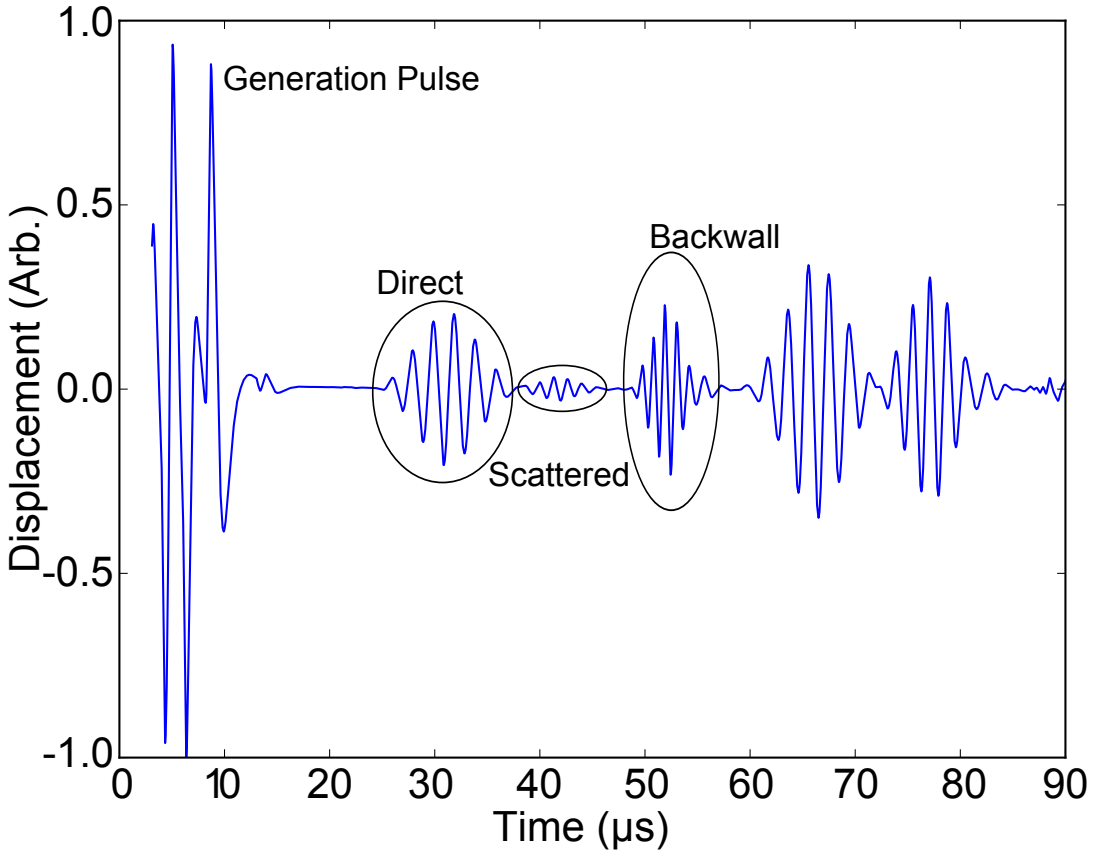

Figure 7.2: An example time domain signal, after being integrated and filtered, with the labels showing the origin of various indications.

between angle of propagation and frequency is for the displacement field. Consequently, the signal was post-processed by numerically integrating the measured velocity signal, using the composite trapezoidal rule [33], in order to recover the displacement signal. A digital bandpass filter, applied in the frequency domain, was used to remove any artefacts that may have been introduced during the integration and to refine the filtering that was previously done in hardware. The displacement signal was Fourier transformed, with a Hann-shouldered window applied to the spectrum in order to bandpass filter the signal and remove all unwanted frequencies. In this work, the passband of the FFT filter was 450 kHz $-$ 1.25 MHz, which was found to be sufficient to reduce the random noise level, whilst not weakening the coherent signal levels.

An example signal, after being post-processed, is shown in figure 7.2, in which

a number of waves can be seen. The first 10 μs of the signal represents electrical noise associated with the generation of ultrasound from the pulsed array, which is detected by the reception transducer. The first significant ultrasonic disturbance that can be seen is the portion of the wave that has travelled directly from the PPM EMAT to the detector. As this section of the wave is travelling along the surface, it will always have a frequency of 520 kHz; this a useful way to identify any direct waves. The back-wall reflection - the wave travelling downwards through the sample, before reflecting from the bottom and then being detected by the linear coil EMAT - starts at around 50 μs. It can be seen that the frequency of the back-wall reflection is significantly higher than the direct wave, and this information can be used to determine the path that the ultrasonic signal has taken through the sample. In between these two signals is a much smaller amplitude indication, and this is the scattered signal indication arising from the presence of the SDH, and is isolated using a time-domain Hann window.

Once the scattered signal has been isolated, it is possible to extract the desired information to calculate the position of the scatterer. The desired information includes the frequency and time of flight of the scattered signal, which will be related to the angular and radial position of the defect, respectively. The use of cross-correlation methods to make high precision time of flight measurements is common within the NDT community. Typically, the cross-correlation approach to time of flight determination requires a reference signal in order to calculate the time shift between the two signals [188]. As the frequency of the wave will vary, dependent upon the position of the scatterer, it is not possible to have a reference signal *a priori*. However, as the general form of the wavefront is known from the modelling performed in Chapters 4 and 5, a reference signal can be synthesised. This synthesised signal has the form:

$$f(t) = Ae^{\frac{-\nu_p^2(t-\tau)^2}{2c^2}} \sin\left(2\pi\nu_p(t-\tau)+\phi\right). \tag{7.1}$$

Here, the constant c determines the length of the signal, and is fixed as this parameter depends on the number of elements in the array. The A represents the amplitude of the scattered wave, ν_p is the peak frequency component of the scattered wave, τ is the time of flight and ϕ is an arbitrary phase shift. These parameters are not known, but they can be recovered from the experimental data with the use of least squares fitting algorithm. The Levenberg–Marquardt algorithm [189] is used to find the parameters $p = (A,\ \nu_p,\ \tau,\ \phi)$ that minimise the squared deviation between the synthesised reference signal shown in equation 7.1 and the experimental data points:

$$S\left(p\right) = \sum_{i=1}^{m} \left[s_i - f\left(t_i,\ p\right)\right]^2, \tag{7.2}$$

where s_i is the i^{th} sample of the experimental data, and t_i is the time value at which the i^{th} sample was taken. This allows for the peak frequency, ν_p, and the time of flight, τ, of the scattered signal to be measured, and used to calculate the radial and angular position of the defect. As the Levenberg–Marquardt algorithm requires some initial guesses of the parameters, estimates of frequency and time of flight of the scattered waves were obtained through other methods. Whilst the algorithm appeared to be robust enough to converge on the correct parameters, even with moderately imprecise initial estimates, the estimates were made as accurate as possible. The scattered signal was normalised, such that the amplitude of this signal was always unity. The peak frequency component was measured by finding the maximum value of the magnitude of the Fourier spectrum, which was obtained by applying an FFT algorithm, whereas the time of flight was estimated by measuring the centre of the envelope of the scattered signal. This is shown in figure 7.3. The envelope of a radio-frequency signal can be obtained by calculating the magnitude of the complex analytic signal, which can be acquired through the application of a Hilbert transform [190]. The analytic signal, $a\left(t\right)$, is the sum of the real signal, $s\left(t\right)$, and the Hilbert transform of this signal, $\hat{s}\left(t\right)$, which applies a 90° phase shift:

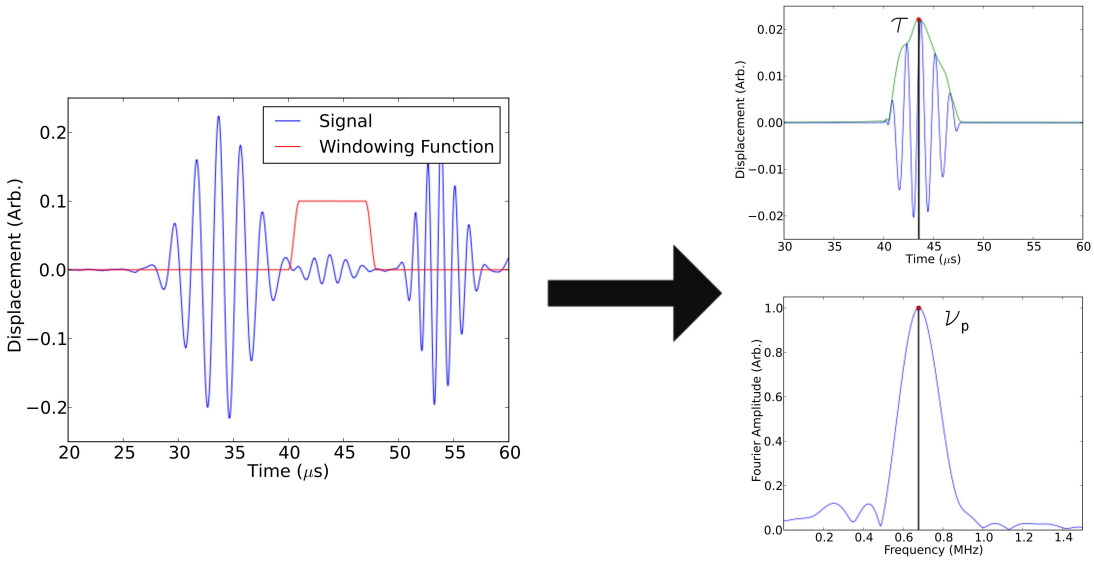

Figure 7.3: Data processing applied to a representative ultrasonic signal. First, the scattered signal is isolated using a time-domain, Hann-shouldered window function. The peak of the envelope of this scattered signal is then found to give the time of flight of the signal, τ. The peak frequency component, ν_p, is also found by applying a FFT and finding the peak in the resultant spectrum.

$$a\left(t\right) = s\left(t\right) + i \cdot \hat{s}\left(t\right). \tag{7.3}$$

From the analytic signal, the envelope signal, $e\left(t\right)$, can be calculated to be:

$$e\left(t\right) = \left|a\left(t\right)\right| = \sqrt{s^2\left(t\right) + \hat{s}^2\left(t\right)}. \tag{7.4}$$

These initial estimates can then be refined by the curve fitting algorithm, in order to accurately fit the experimental data, as shown in figure 7.4. Once accurately known, these values can be used to calculate both the radial and angular position of the defect. The peak frequency component of the scattered signal, ν_p, can be related to the angular position of the SDH that scattered the wavefront, θ, by modifying the diffraction grating equation:

$$\theta = \arcsin\left(\frac{c}{\nu_p d}\right), \tag{7.5}$$

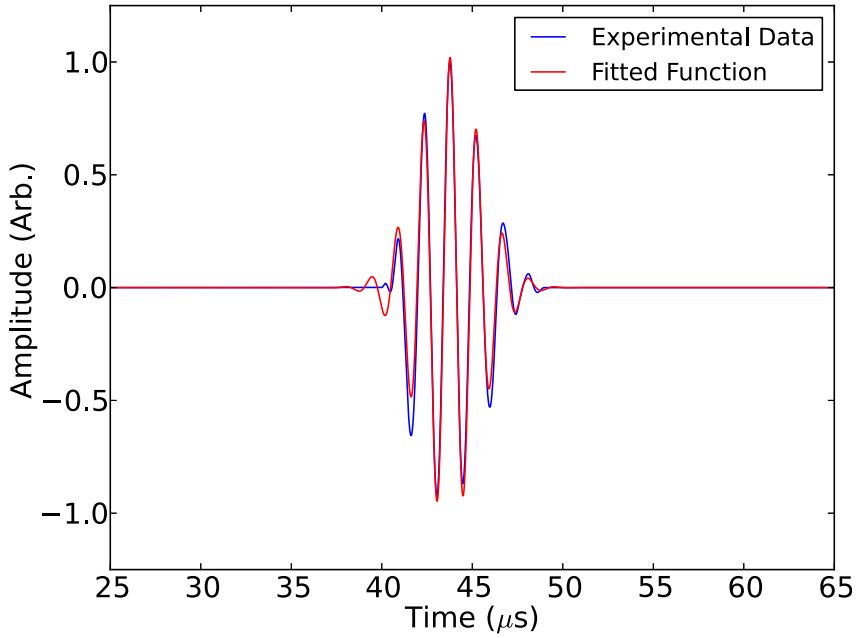

Figure 7.4: A synthesised signal, described by equation 7.1, is fitted to the experimental data. The parameters used to define the function are obtained through a non-linear least squares fit procedure. The ends of the experimental data may deviate from the expected relationship because of interference from either the direct wave or the back-wall reflection.

where d is the periodic length of the array, and c is the ultrasonic shear speed in aluminium. The radial position can be found by obtaining the time of flight of the pulse. From the geometric layout shown in figure 7.5, it can be seen that time of flight, τ, can be related to the path taken by:

$$\begin{aligned} c\tau &= \sqrt{x_i^2 + y_i^2} + \sqrt{(x_D - x_i)^2 + y_i^2} \\ &= R_i + \sqrt{(x_D - R_i \sin\theta)^2 + R_i^2 \cos^2\theta}, \end{aligned} \tag{7.6}$$

where all of the parameters can be found in figure 7.5. Equation 7.6 can be rearranged to find the radial distance between the centre of the array and the scatterer, R_i:

$$R_i = \frac{(c\tau)^2 - x_D^2}{2\,(c\tau - x_D \sin\theta)}. \tag{7.7}$$

Hence, through knowledge of the angular position of the defect, obtained by measuring the peak frequency of the scattered signal, and the time of flight, τ, the

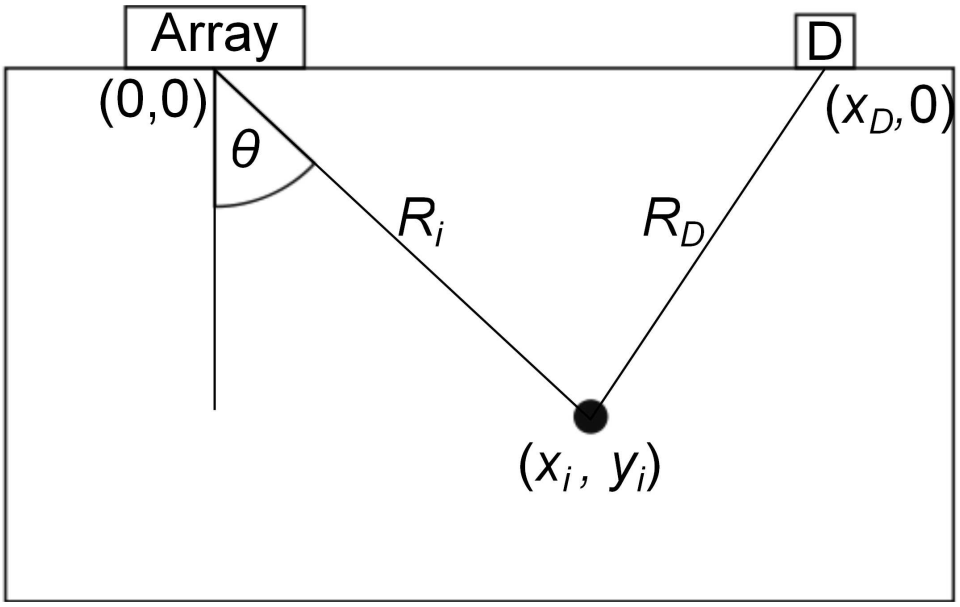

Figure 7.5: The unknown location of a defect, (x_i, y_i), can be found in terms of polar co-ordinates, (R_i, θ), using a pulsed array and a separate detector, which is marked D, and is a distance x_D from the array.

radial position of the SDH, relative to the centre of the PPM EMAT, can be found. The whole data processing procedure can be seen in figure 7.3.

It should be noted that this shows how the location of the defect can be constrained with a single measurement. Traditional ultrasonic methods only use time of flight information, meaning that the defect could be located anywhere along a path. Theoretically, the pulsed wavefield can be used to inspect a large angular range, between 20° and 90°, with a single pulse. However, with this configuration, the scattered signal is constrained between the direct wave and the back-wall reflection. Consequently, at certain angles, the scattered signal is obscured by either the surface or back-wall wave; meaning that the scatterer cannot be located at these points.

Despite this, it was possible to scan the array across the surface of the sample, which had the effect of changing the angle of the defect relative to the centre of the array. Hence, with the detection EMAT being a fixed position 140 mm away from the end of the sample edge, the array was scanned in 5 mm increments along the surface of the sample. This meant that the angular position of the defect, relative

Scan Position	Measured ToF and Frequency (τ, ν_p)	Measured Position (r, θ)	Calculated Defect Position (r, θ)
31 mm	$(36.2 \pm 0.5\ \mu\text{s}, 824 \pm 4\ \text{kHz})$	$(53.8 \pm 0.8\ \text{mm}, 39.0 \pm 0.2°)$	$(51.4\ \text{mm}, 37.1°)$
36 mm	$(35.8 \pm 0.5\ \mu\text{s}, 790 \pm 4\ \text{kHz})$	$(54.4 \pm 0.8\ \text{mm}, 41.0 \pm 0.2°)$	$(54.6\ \text{mm}, 41.3°)$
41 mm	$(38.5 \pm 0.5\ \mu s, 740 \pm 4\ \text{kHz})$	$(57.5 \pm 0.8\ \text{mm}, 44.5 \pm 0.5°)$	$(58.0\ \text{mm}, 45.0°)$
46 mm	$(42.6 \pm 0.5\ \mu\text{s}, 694 \pm 4\ \text{kHz})$	$(61.9 \pm 0.8\ \text{mm}, 48.3 \pm 0.5°)$	$(61.6\ \text{mm}, 48.3°)$
51 mm	$(41.4 \pm 0.5\ \mu\text{s}, 678 \pm 4\ \text{kHz})$	$(64.4 \pm 0.9\ \text{mm}, 49.9 \pm 0.5°)$	$(65.4\ \text{mm}, 51.2°)$

Table 7.1: Results obtained from the pitch-catch experiments. The scan position refers to the lateral separation between the defect and the array, which can be used to calculate the position of the defect relative to the array in polar co-ordinates. The table also shows the measured time of flight and frequency of the scattered wave, before converting these values into radial and angular co-ordinates.

to the centre of the array, was varied between 37° and 51°, with the exact position shown in Table 7.1. By measuring the time of flight and frequency of the scattered wave, as described in the previous section, the radial distance and angular position of the defect can be found. As the location of the SDH was known, the measured values can be compared with the known position of the defect.

The results in Table 7.1 generally indicate good agreement between the known location of the SDH, and the location obtained from measuring the time of flight and frequency of the ultrasonic scattered wave. However, whilst the results are generally in the correct range, some of the measured positions of the defect are outside of the experimental uncertainty range. Some of the reasons for this, along with limitations of this approach, are discussed below. Despite these problems, the results demonstrate how a wavefront generated by a broadband pulsed array can be utilised to localise a discontinuity which may scatter the wavefront. Unfortunately, due to the interference of the surface and back-wall signals, only a limited range of angles could be inspected. Whilst this is, in part, a consequence of the limited dimensions of the sample, it is an inherent problem with using a second transducer, as it will always detect the direct direct wave, as well as other reflections from the boundaries of the sample. However, these experimental measurements can be supplemented by FE element simulations, which can utilise absorbing boundary conditions in order to eliminate the back-wall reflection and allow a greater area to

be inspected.

Such a finite element model was constructed, with the same geometry as figure 7.1, but with absorbing boundary conditions used to remove reflections from the surfaces of the sample. The simulated array consisted of six 'elements' of pressure loads applied to the surface, in an alternating polarity arrangement with a periodic distance of 6 mm in order mimic the PPM EMAT. However, in this simulation, in contrast to the experiments, both the array and detection point remained in a fixed position so that the angular size of the defect remained constant. A circular void with a radius of 0.75 mm, simulating the side-drilled hole, was positioned with a fixed radial position of 60 mm, with the angular position varied from 20° to 80° in 1° increments. For angles less than 20°, the wavefront no longer has a smoothly varying frequency, whilst for angles greater than 80°, the direct wave interferes with the scattered wave, so that it cannot be analysed. However, within the angular range $20° \leq \theta \leq 80°$, the scattered signal could be isolated so that the frequency spectrum of the scattered wave could be analysed. This is shown in figure 7.6, which demonstrates how the peak frequency component changes with the angular position of the defect. The diffraction grating equation is also plotted on this figure, along with the experimental values from Table 7.1, which shows the good agreement between known angular position of the SDH, and the measured values obtained from the frequency of the scattered signal.

Whilst this method of localising the SDH has led to some promising results, there are a number of considerations that must be made in order to explain the small discrepancies between the measured and known locations of the defect. It should be remembered that the SDH has a radius of 0.75 mm, meaning that the defect has a finite angular size. The known positions of the defect refer to the centre of the SDH, whereas the ultrasound is obviously scattered from the surface of the defect. This can lead to misalignment between the measured and known location of the defect. For such a small defect this distance from the array, the angular

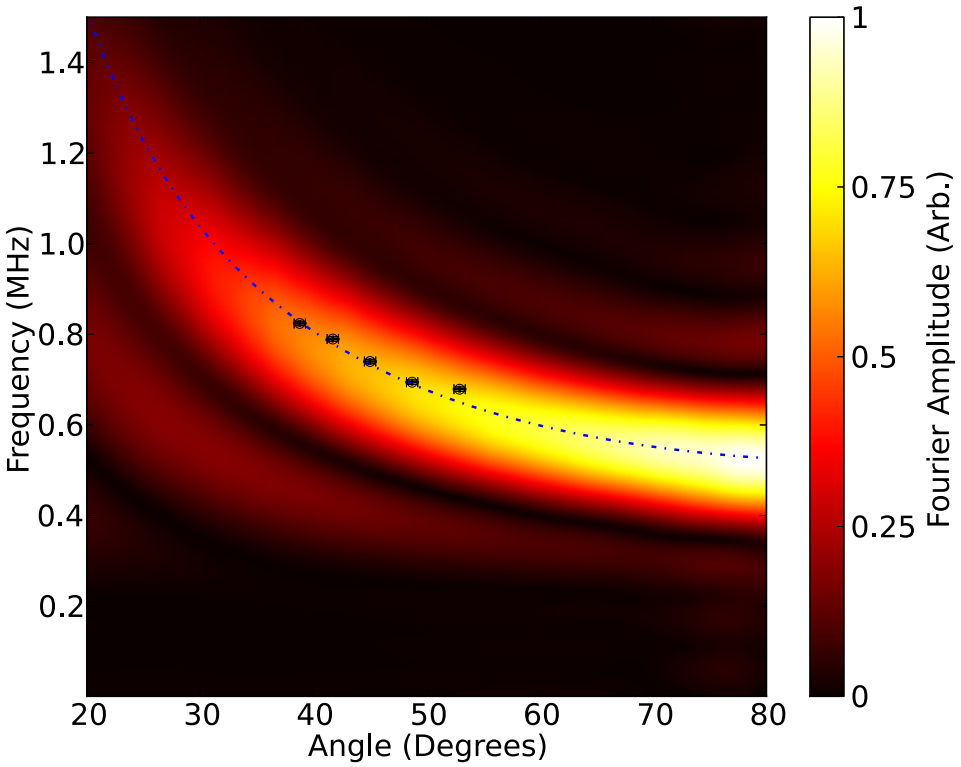

Figure 7.6: The normalised magnitude of the Fourier spectra for the scattered signals obtained from the FE simulations at each angular position. The dashed line represents the theoretical values from the diffraction grating equation, with the experimental data points, shown in Table 7.1, also plotted.

size presented to the wavefront is limited to around 1° to 2°, so that this problem is not particularly pronounced. However, the angular extent of the scatterer must be considered for larger defects, especially as the section of the defect illuminated by the wavefront will change as a function of angle. Consequently, the change in frequency of the scattered wave will not only be dependent upon the angle between the array and the defect, but also the detection EMAT and the defect. Additionally, as the calculation of the radial position of the defect relies on the measured estimate of its angular position, any uncertainty in the angular position will lead to greater uncertainties in the estimation of radial position of the defect.

Another problem occurs because of the size of the defect, and the effect that this may have on the scattering of the wavefront. The method utilised here assumes that the scattering processes are frequency independent, so that the scattered wave has the same frequency content as the incoming wave. However, this is known to be false, with the scattering cross-sections having a complex relationship with frequency [191–193]. Notwithstanding the frequency dependent scattering, it has been observed in both the experimental measurements and FE simulations that there is no significant shift in frequency of the scattered wave, as evidenced by the accuracy of the location ability of this method. These two statements can be reconciled by again considering the relatively small angular size of the defect in this case. As the angular size of the defect is only around 1°, it only scatters a small section of the generated wavefront. Consequently, the angular bandwidth of the scattered signal is sufficiently small, such that the scattering processes can be assumed to be locally frequency independent [102]. However, this is not a general result, and significant frequency shifts may be observed for larger defects.

Finally, the frequency response of the detector transducer must be considered. The effect of the finite size of the transducer on the frequency response, and how this can alter the measured frequency of a wave, has already been discussed in Section 6.1.2.1. It was seen that when the size of the transducer becomes comparable with

the wavelength of the detected wave, the transducer becomes more directional and suffers from a reduction in efficiency. Hence, a high frequency tone-burst wave can be susceptible to distortion, with the lower frequency components of the measured waves being artificially enhanced. The linear coil EMAT used as the detection EMAT has a width of 3 mm, which corresponds to shear wave in aluminium with a frequency of 1.04 MHz. As the maximum frequency of the scattered wave was 824 kHz, and the angle between the defect and the detection EMAT being fixed at 49°, there is only a limited effect on the measured frequency of the scattered wave. Again, this is not a general result, and as the frequency of the scattered wave approaches 1 MHz, the effect will become more pronounced. However, despite these problems, it can be seen that the pulsed wavefront can be used to locate the position of a circular side-drilled hole with just a single measurement.

7.2 Aluminium Notches

It has been seen how the use of a separate detection transducer in a pitch-catch configuration can locate a defect by measuring the time of flight and frequency of the scattered ultrasonic wave. However, this particular configuration has some inherent problems, due to the frequency response of the receiver and the interference of the scattered wave with other waves reflected from the sample boundaries. These problems are alleviated through the use of a single PPM transducer as both the transmitter and receiver, using the pulse-echo method to detect any backscattered signals that may occur due to the presence of a number of discontinuities in the sample. This also has the effect of simplifying the geometry for locating the defect, as the time of flight of the scattered signal can be very simply related to the radial distance between the discontinuity and the array. The frequency dependence of the directivity of the array also applies in reception. This means that directly backscattered signals will be received without any distortion, whilst non-backscattered

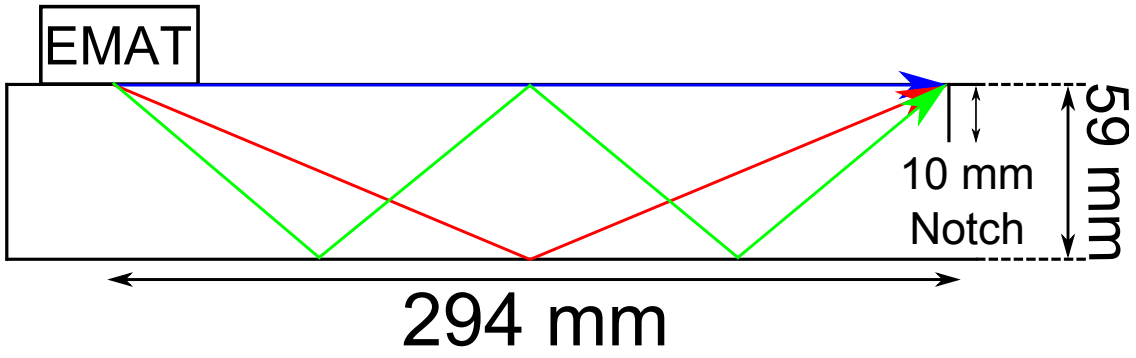

Figure 7.7: Schematic experimental diagram, illustrating the multitude of possible ultrasonic paths from the 10 mm deep notch.

signals will be partially filtered. This will reduce the complexity of the signal received, without detrimentally affecting the scattered signals that are to be analysed.

Initially, in order to examine this principle, a rectangular aluminium bar, with a cross-sectional area of 59 x 59 mm^2, was used as a test specimen. This bar was machined with notches to act as discontinuities to scatter the ultrasound. The largest and nearest of these notches was 10 mm deep, with a width of 1 mm, and it was this notch that was the primary source of the reflections visible in the experimental data. Whilst it can be seen in figure 7.7 that there is only a single notch present, due to the limited extent of the sample, there are a number of paths that the ultrasound can take to the defect by reflecting from the top and bottom surfaces of the sample. These paths will have unique time of flight and angular orientations, and consequently, can be used to test the ability of the PPM EMAT to locate defects over a wide angular range. This means that the ability for the PPM EMAT to detect and locate defects over a large angular range to be tested. Again, a six element, 3 mm pitch PPM EMAT was used to generate the ultrasound, and was placed at the end of the bar, as shown in figure 7.7. As the EMAT was again operating on an aluminium sample, with a shear speed of 3111 ms^{-1}, the frequency of the direct wave was 518 kHz.

The array was excited using the Ritec RPR-4000 pulser receiver unit, with pulse-echo mode being achieved using the internal diplexer to switch between transmit

and receive mode. However, the echoes received are obscured by an electrical ringing signal, caused by the interference between the amplifier and the transducer itself. As this electrical ringing is coherent and is independent of the received ultrasonic signal, the backscattered signals can be recovered by using a simple background subtraction. The background signals were obtained by rotating the EMAT by 45°, which ensured that there were no reflected signals in the time window of interest of the background signal. Whilst this was found to be effective at removing the ringing signal, and revealing the ultrasonic data, it is inconvenient, as a background signal is needed for each different configuration; a new background signal is needed if sample, EMAT or excitation signal changes. After the background subtraction, a digital, frequency domain band-pass filter was applied, with a passband of 400 kHz − 1.5 MHz, so that only the frequencies of interest remain within the signal.

7.2.1 Narrowband Frequency Steering

The pulse-echo arrangement also allows for the use of the PPM EMATs frequency steering abilities; with the ultrasound being steered to a particular angle when it is excited by a specific frequency tone-burst signal. Hence, by varying the input frequency during the measurement, it is possible to sweep the ultrasonic beam over a range of angles. As with phased array sector scans, the echo caused by the defect will reach a maximum amplitude when the steering angle of the array coincides with the angular position of the defect [140,194]. For this simple pulse-echo configuration, the radial position of the notch is simply dependent upon the time of flight and speed of the echo.

As was seen from Chapter 3, the PPM EMAT can steer a single ultrasonic beam in the angular region of $20° \leq \theta \leq 90°$ by simply varying the excitation signal. Hence, the array was excited with a tone-burst five cycle sine wave, with the excitation frequency varying from 520 kHz up to a maximum frequency of 1.07 MHz. This ensured that the inspection had a good angular coverage, whilst the frequency

was increased in increments of 10 kHz to ensure good angular resolution. The A-scan time-domain data from each frequency can be stacked together to form a B-scan image, with the time and frequency axes representing radial and angular position, respectively. Such an image is shown in figure 7.8, where many large amplitude reflections can be seen, and their amplitude changing as the excitation signal varies. The first signals to arrive, for the lower frequencies, correspond to the wave travelling along the surface, before being reflected by the notch and travelling back to the EMAT. This analysis agrees with intuition; it is the shortest path, and being along the surface, the angle corresponds to the lowest steering frequency. Subsequent signals that arrive later in time are also scattered by the 10 mm notch, but have taken multi-skip paths to the defect, with the high excitation frequencies steering the ultrasound to steeper angles through the sample.

As the location of the defect and dimensions of the aluminium bar are known, the length and angle of propagation of the expected paths taken by the ultrasound can be calculated, from simple geometry, using figure 7.7. The expected path lengths are converted into times of arrival, and are plotted on figure 7.8 as vertical lines to act as a comparison between measured and expected time of flight values. This shows good agreement between the two values, demonstrating that the radial positions of the echoes can be ascertained with a good degree of accuracy. Smaller amplitude signals can be seen between the expected, and marked, indications from the 10 mm notch, and these arise from other, smaller notches further along the bar. A larger amplitude signal, at 375 μs, is seen in the lower frequency data; this corresponds to a multiple reflection of the surface echo originally seen at 189 μs.

In addition to determining the radial position of the defect signal paths, it is possible to calculate their angular positions as well. It can be seen from figure 7.8 that the amplitude of the reflected echoes vary with frequency. By time windowing the data in order to isolate each individual echo, it is possible to identify how the amplitudes of these echoes change as a function of frequency. It would be expected

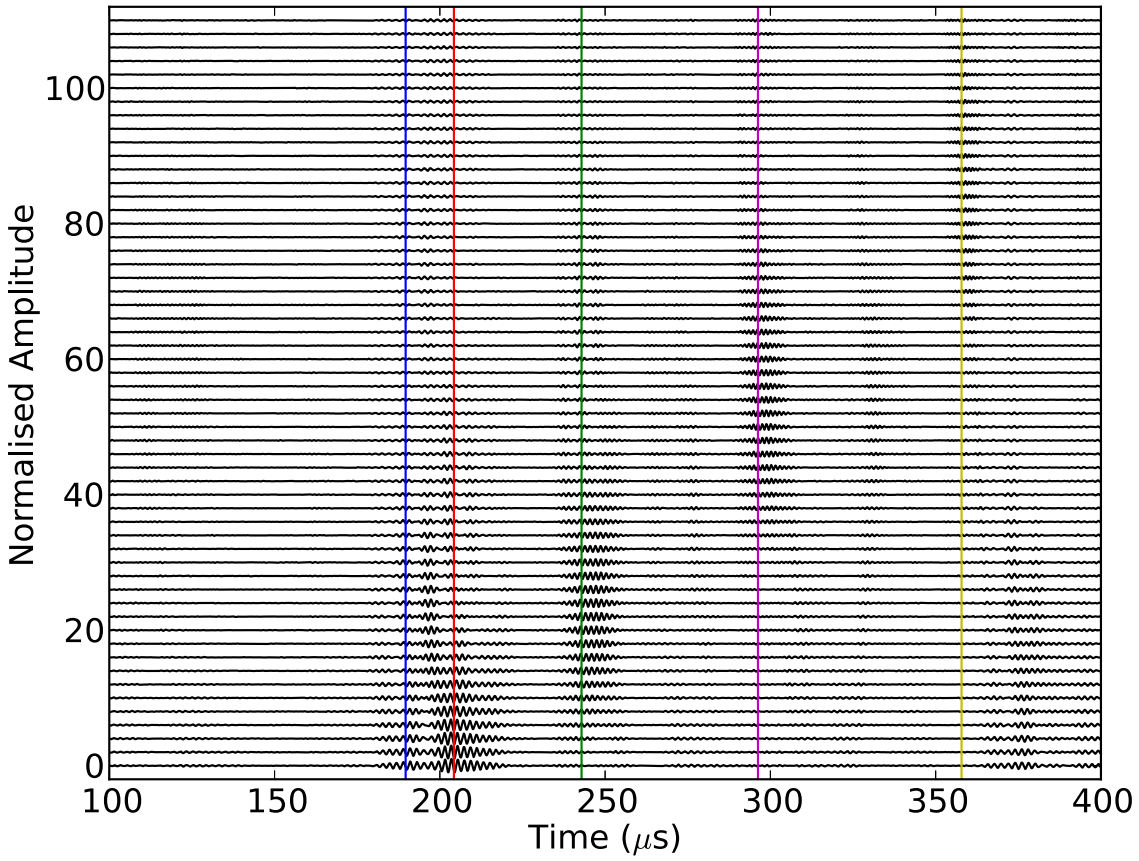

Figure 7.8: Experimental backscatter signals obtained at different frequencies, starting at 520 kHz and rising in 10 kHz increments until reaching 1.07 MHz. Also shown on the figure are the expected times of flight, calculated from geometry, which are plotted as vertical lines upon the data.

Number of Skips	Measured ToF and Frequency (τ, ν)	Measured co-ordinates (r, θ)	Calculated co-ordinates (r, θ)
0	$(190.2 \pm 0.5\ \mu\text{s}, \text{n/a})$	$(295.8 \pm 0.8\ \text{mm}, \text{n/a})$	$(294.0\ \text{mm}, 90.0°)$
1	$(203.5 \pm 0.5\ \mu\text{s}, \text{n/a})$	$(316.5 \pm 0.8\ \text{mm}, \text{n/a})$	$(316.8\ \text{mm}, 68.1°)$
2	$(246.4 \pm 0.5\ \mu\text{s}, 638 \pm 5\ \text{kHz})$	$(383.3 \pm 0.8\ \text{mm}, 54.3 \pm 3.0°)$	$(377.0\ \text{mm}, 51.2°)$
3	$(297.3 \pm 0.5\ \mu\text{s}, 789 \pm 5\ \text{kHz})$	$(462.5 \pm 0.8\ \text{mm}, 41.1 \pm 1.6°)$	$(460.2\ \text{mm}, 39.7°)$
4	$(358.1 \pm 0.5\ \mu\text{s}, 957 \pm 5\ \text{kHz})$	$(557.1 \pm 0.8\ \text{mm}, 32.8 \pm 1.0°)$	$(556.1\ \text{mm}, 31.9°)$

Table 7.2: Comparison between the calculated co-ordinates of the five observed echoes, and those obtained through the frequency sweep measurements. Some of the results are not consistent with the calculated co-ordinates, although this can be explained by the extended size of the notch.

that the amplitude of the echo will be at a maximum for a frequency that corresponds to a steering angle that matches the angular position of the defect. The root mean square (RMS) of the time windowed echo data was calculated at each excitation frequency, which can be related to the steering angle by using the diffraction grating equation. Whilst the first two signals could not be isolated in time, the last three echoes are clearly resolved and can be analysed in this way. The frequency variation of the RMS amplitudes of each of these signals can be seen in figure 7.9, with clear peaks visible at different angles for the various echoes. The measured time of flight and frequency values, are converted into radial and angular co-ordinates, can be seen in Table 7.2, along with the geometrically calculated polar co-ordinates of the multi-skip paths of the defect. It becomes apparent that there is generally good agreement between measured path length and angle and the geometrically calculated values. The relatively large length of the notch may be the source of some discrepancies, as the geometric calculation assumes a point reflection from the surface of the sample. The finite length of the notch means that, in fact, a range of paths are valid as reflections from the face of the notch, rather than simply at the intersection of the notch with the surface of the sample.

From figure 7.8, it is also apparent that the resolution of the angular measurement changes with frequency; with the amplitudes of the echoes being very highly peaked at the lower angles, whilst spreading out over a large range for the larger angles

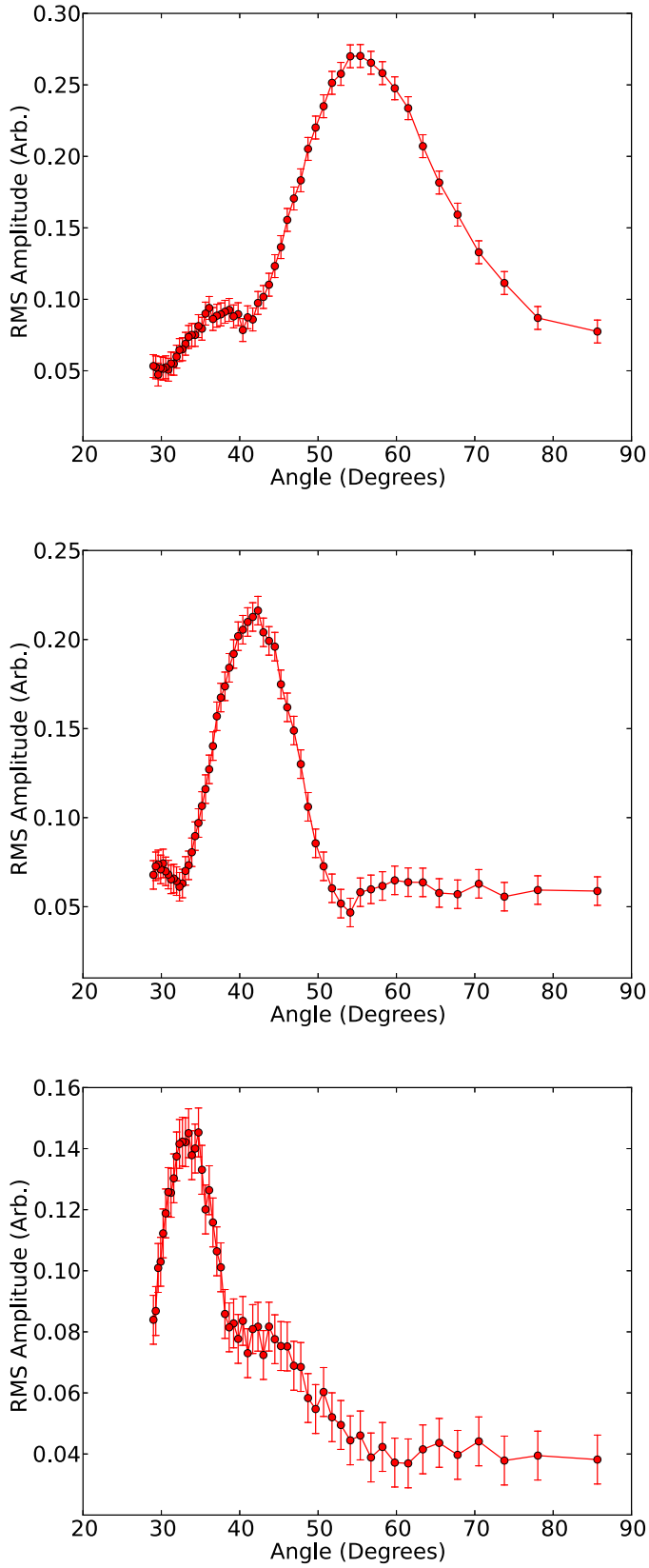

Figure 7.9: Angular dependence of the scattered wave amplitude for the defects at 51°, 40° and 32°, respectively.

towards the surface. This is a consequence of the inverse proportionality between frequency and angle that can be seen from the diffraction grating equation, and can also be seen in the directivity modelling shown in Chapter 3. For higher excitation frequencies, the ultrasonic beam is steered much more tightly, so that a smaller beam width at the lower angles (higher frequencies) leads to a better resolution than at higher angles (lower frequencies), where the ultrasound is steered over a much larger range of angles.

The driving signal obviously also has an effect on the beam width achieved by frequency steering. By driving the array with a narrow bandwidth signal, the ultrasonic beam will be steered over a narrower range of angles, as there are only few frequencies present, and so there is only a limited range of angles for the signal to constructively interfere. However, a narrow bandwidth signal necessarily implies a large temporal range, leading to poor axial resolution. Therefore, there is an explicit compromise between angular and axial resolution caused by time-frequency duality: increased angular resolution directly causes a reduction in the axial resolution that could be achieved, and vice versa [195]. Nevertheless, a 5 cycle tone-burst appears to be a good compromise, with reasonable axial and angular resolution being achieved in this case.

7.2.2 Broadband Pulsed Approach

The same sample can be inspected using the pulsed properties of the array, which will generate a wavefront that spreads out and covers a large angular range. Consequently, this region can be inspected with a single measurement, which is in contrast with the frequency steering method, which requires 56 measurements at different frequencies. Whilst the number of measurements required for each method is doubled due to the necessity for background data for the baseline subtraction, the pulsed approach still has a much faster acquisition time when compared to the frequency steering approach. The pulsed experiment configuration is the same as

in previous sections, as shown in figure 7.7, with the same EMAT being used to perform the measurements. However, in order to generate the pulsed wavefront, a higher bandwidth signal is required. Consequently, the array is pulsed with an 800 kHz single cycle sine wave, as this was shown to have sufficient frequency content over the required frequency range.

As the pulsed wavefront will cover all of the multi-skip paths to the defect simultaneously, the signal received will contain all of these echoes. Therefore, a form of time-frequency analysis is required in order to localise the individual reflections in both time of flight and frequency, which will make it possible to calculate the radial distance and angular position of the defect paths. A spectrogram, calculated as the squared magnitude of a short-time Fourier transform (STFT), is used to this end [196, 197]. STFT can be used to study the frequency content of non-stationary signals by applying a sliding window function to the data, to split the signal into a number of segments of equal size. Each of these segments can then be Fourier transformed to reveal their frequency content, which can be compared to other sections of the signal to see how the frequency content of the signal changes with time. Hence, it can be said that the spectrogram expands the time domain signal to show the time-localised frequency content, allowing the signals to be clearly resolved in both the time and frequency domains. As a consequence of time-frequency duality, frequency resolution and time resolution are inversely proportional to each other; an improvement in the frequency resolution necessarily comes at the expense of the time resolution [198]. Hence, both the time and frequency resolution of the STFT are decided by the choice of windowing function used to calculate the STFT. If the time domain signal obtained is given by $s(t)$, and the windowing function, centred on time, τ, is described by the function $w(t-\tau)$, then the STFT function, $S(\tau, \omega)$ is given by:

$$S(\tau, \omega) = \frac{1}{2\pi} \int_{-\infty}^{\infty} s(t)\, w(t-\tau)\, e^{-i\omega t}\, \mathrm{d}t. \tag{7.8}$$

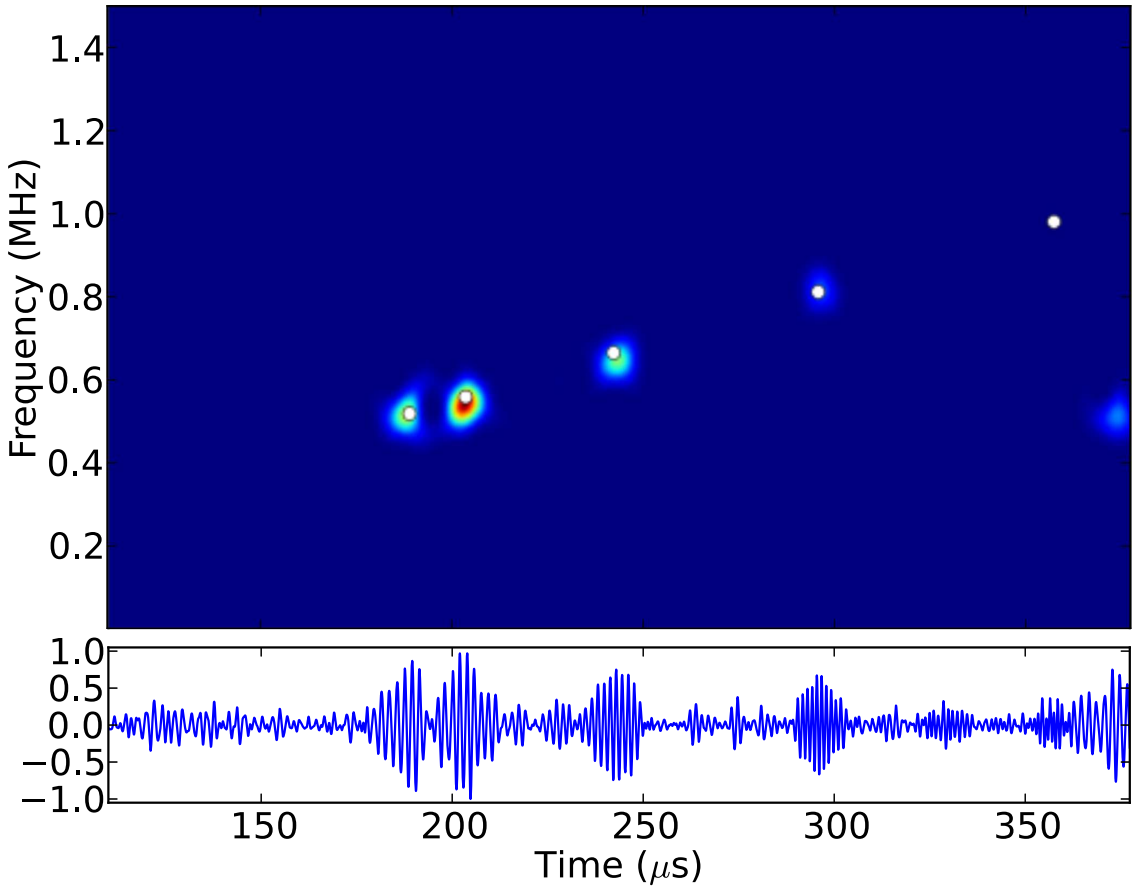

Figure 7.10: Time domain signal and spectrogram data showing the time localised frequency of the signal. The circles also plotted correspond to the expected time of flight and frequency of the reflections, which are calculated from geometry.

The energy density spectrum is expressed through a spectrogram, which is simply the squared magnitude of the STFT:

$$|S(\tau, \omega)|^2 = \left| \frac{1}{2\pi} \int_{-\infty}^{\infty} s(t)\, w(t-\tau)\, e^{-i\omega t}\, \mathrm{d}t \right|. \tag{7.9}$$

In this work, the particular windowing function that was used was the Hann function, as this significantly reduces the effects of side-lobes within the frequency distribution, although this comes at the expense of slightly widening the main peak [196, 198]. The spectrogram can also be calculated with an overlap between neighbouring time segments, which acts to smooth the appearance of the time-frequency distribution, although this does not improve its resolution.

Number of Skips	Measured ToF and Frequency (τ, ν)	Measured co-ordinates (r, θ)	Calculated co-ordinates (r, θ)
0	$(189.2 \pm 0.3\ \mu s, 519 \pm 5\ kHz)$	$(294.3 \pm 0.5\ mm, 87.8 \pm 7.2°)$	$(294.0\ mm, 90.0°)$
1	$(203.3 \pm 0.3\ \mu s, 544 \pm 5\ kHz)$	$(316.5 \pm 0.5\ mm, 72.5 \pm 0.9°)$	$(316.8\ mm, 68.1°)$
2	$(243.2 \pm 0.3\ \mu s, 653 \pm 5\ kHz)$	$(378.3 \pm 0.5\ mm, 52.6 \pm 0.5°)$	$(377.0\ mm, 51.2°)$
3	$(295.7 \pm 0.3\ \mu s, 812 \pm 5\ kHz)$	$(459.9 \pm 0.5\ mm, 39.7 \pm 0.2°)$	$(460.2\ mm, 39.7°)$
4	$(357.3 \pm 0.3\ \mu s, 984 \pm 5\ kHz)$	$(555.8 \pm 0.5\ mm, 31.8 \pm 0.5°)$	$(556.1\ mm, 31.9°)$

Table 7.3: Comparison between the estimated radial and angular position, obtained by measuring the time of flight and frequency of the echoes, and the known co-ordinates, obtained through geometry.

The spectrogram of the time domain data obtained, after being integrated to recover the wave displacement, can be seen in figure 7.10. The spectrogram expands the A-scan to show the time-localised frequency of the many echoes, allowing the signals to be clearly resolved in both time and frequency. The location of the peaks in the spectrogram is related to the length and angle of the ultrasonic path to the defect, with the white circles overlaid on the figure indicating the calculated time of flight and frequency from the expected path length and angle of propagation [199]. Again, it can be seen that there is very good agreement, and that the pulsed method can localise defects very well, with the results shown in Table 7.3.

From comparing Tables 7.2 and 7.3, it can be seen that, both methods can be used to locate defects over a wide range of angles. However, it should be noted that the pulsed array results offer improved accuracy and precision. This can be explained by the fact that the pulsed wavefront is continuous over the entire angular range of interest, whereas the frequency steering method is effectively sampling the structure at discrete angles. This increased amount of information is reflected in improved resolution of the results obtained using the pulsed method. As observed with the frequency sweep approach, the resolution of the pulsed approach also vit can cover the same angular region with a single scanaries with angle, which is a consequence of the inverse proportionality between angle and frequency. Therefore, the same uncertainty in frequency leads to a much greater angular uncertainty at higher angles than it does for the lower angles.

Despite spreading the ultrasonic energy over a large angular range, the pulsed method is also able to achieve a good signal-to-noise ratio, with most of the echoes being clearly identifiable. Whilst the notch is deep (10 mm), and therefore allows for a range of ultrasonic paths to be detected, it should also be noted that some of the echoes are travelling a round trip of over 1 m. This shows that the transducer is sufficiently efficient to generate a useful wavefront over a large range of angles.

7.2.3 Real Defect in Aluminium Billet

The pulsed array system has been shown to work well on artificially cut notches, with the path length and angle of propagation of the echoes being able to be ascertained by measuring the time of flight and frequency of any scattered waves. However, for this to be a useful ultrasonic technique, it must be demonstrated to work on industrially relevant defects, which have a much more complex structure than machined notches. The pulsed approach was proven to be superior, in terms of both scan speed and result accuracy, and so only the pulsed method is shown here. Hence, in this section, an aluminium billet, which has rough, surface breaking casting defect, is used. This defect, shown in figure 7.11, was created in the manufacturing process and has a depth that varies between 2 mm and 20 mm [51].

Rough defects have a number of properties that could make their detection and localisation difficult. Firstly, the roughness of the crack will diffusely scatter the incident ultrasound energy, leading to reduced echo amplitudes [64, 200, 201]. This is in contrast to the specular reflections that were obtained from the artificial cut notches, which resulted in higher amplitude indications. Hence, it is important to determine whether the scattered waves can be detected, so that they can be analysed to locate the defect. Secondly, the roughness of the defect may introduce frequency dependent scattering events, which could cause an angular mis-location of a defect. Whilst most of the roughness associated with the defect shown in figure 7.11 will be on a scale much smaller than the wavelength of the ultrasound, it will still not

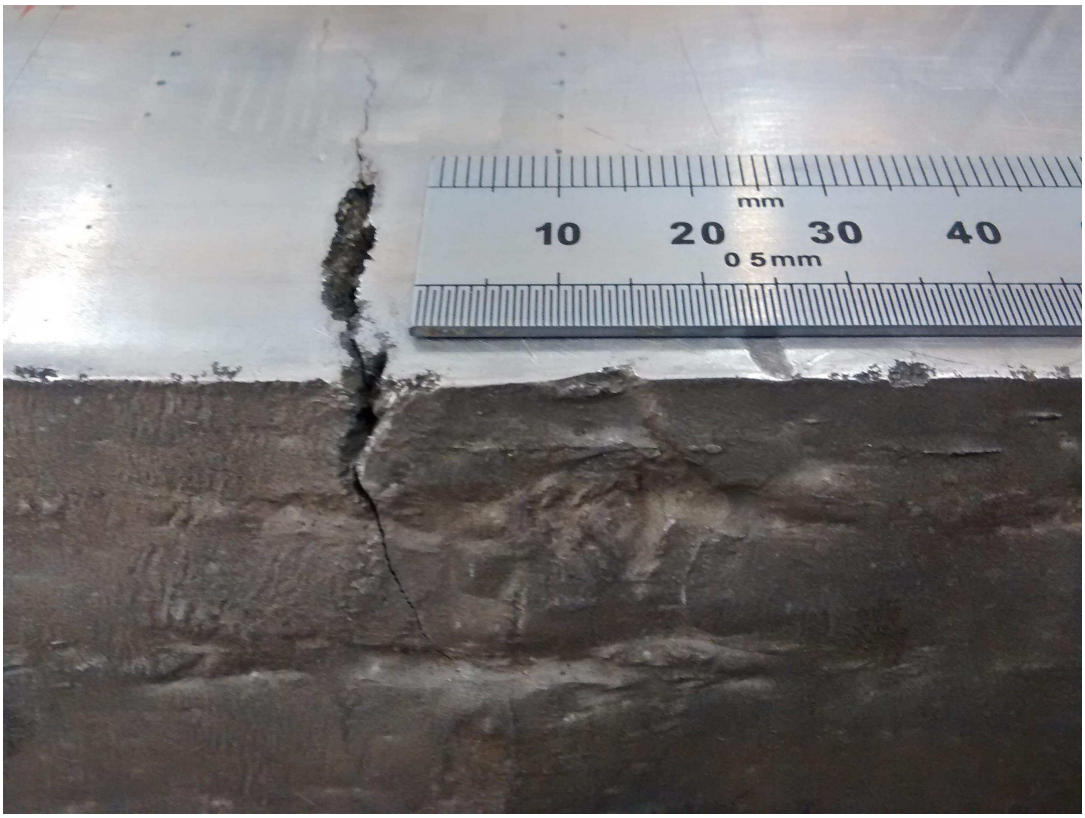

Figure 7.11: An image of the rough crack, showing its surface and depth profile.

act as a planar scatterer. As seen from the previous experimental data in Section 7.2.2, there appears to be no indication that scattering events significantly alter the frequency content of the pulse. However, this must still be investigated to ensure scattering interactions with rough defects are also frequency independent.

The experimental geometry is shown in figure 7.12, which indicates the position of the defect on the top surface, as well as demonstrating the location of the PPM EMAT, which was placed on the bottom surface of the billet. Placing the EMAT on the opposite side to the defect will separate in time any scattered signals arising from the crack from any reflections from the edge of the sample. The latter will be of much larger amplitude, and could obscure the scattered signal. The frequency of the scattered wave will also be distinct from the direct wave reflections, which will possess a frequency equal to the fundamental frequency of the array, ν_0. As the rough nature of the crack did affect the scattering amplitudes, a lower frequency

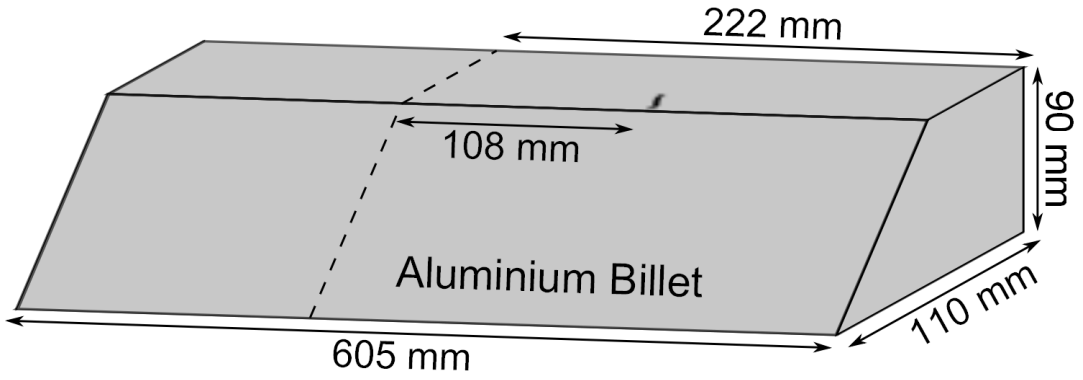

Figure 7.12: Schematic diagram of sample. The centre of the PPM EMAT, which is located on the underside of the sample, is indicated by the dashed line. The defect is also indicated on the diagram, shown 108 mm from the centre of the array.

PPM EMAT had to be used. The 5 mm pitch EMAT, previously used in Chapter 6, was utilised in this experiment. This is because it has an element size of 4 mm, which increases the generation area, which, in turn, enhances the amplitude of the generated wavefront. Also, as the generated wavefront has a lower frequency than the one generated using the 3 mm, the crack acts more like a planar defect, meaning less of the energy is diffusely scattered.

As before, the ultrasonic data were obtained using the EMAT in pulse-echo mode, with background subtraction. However, because of the different EMAT dimensions, a different excitation signal is required. As has already been demonstrated, a single cycle 450 kHz signal (figure 6.7) possesses the necessary frequency content and so is used to excite the pulsed array. Again, after the baseline subtraction, the resultant signal was integrated and band-pass filtered to remove all unwanted frequency components. The time domain signal was then analysed using a spectrogram to obtain a time-frequency map of the sample, as demonstrated in figure 7.13.

In figure 7.13, a number of indications are visible. The indications that can be seen between 140 μs and 160 μs are consistent, in terms of both arrival time and frequency, with reflections from the end of the sample. The signal that first starts to arrive is the direct wave, being reflected from the end of the billet. The signal that arrives slightly later, and has a somewhat higher frequency, arises from

the wave that travels through the bulk of the sample, having been reflected from bottom end of the sample, before travelling back and being detected by the EMAT. For clarity, the calculated travel times and frequencies of these waves are shown on the spectrogram for comparison. However, this still leaves a single indication that can not be accounted for by the geometry of the sample. This is the indication that peaks at 91.1 ± 0.3 μs in the time domain, with a frequency of 400 ± 5 kHz. Once these are transformed into spatial co-ordinates using the known wave speed, for the radial position, and the diffraction grating equation, for the angular position, it is found that the position of the defect was $(r, \theta) = (141.7 \pm 0.5 \text{ mm}, 51.0 \pm 1.0°)$. As the defect was surface breaking, the distance from the EMAT to the defect could easily be measured, and was found to be $(r, \theta) = (140.9 \pm 1.0 \text{ mm}, 50.2 \pm 0.2°)$. The pulsed array method agrees well with the known position of the defect, with both the radial and angular position being calculated within experimental error.

From the accuracy of the angular measurement, it is apparent that there is no strong frequency dependence in the scattering processes in the bandwidth of the scattered signal. This is not to say that the scattering event does not have any frequency dependence; it simply implies that the variation in scattering is small enough over the bandwidth of the signal that the peak frequency of the signal has not been significantly altered by the scattering event. Also, by utilising the larger pitch PPM EMAT array, the generated ultrasound amplitudes were large enough to detect scattered signals from a rough defect. This adds confidence that the pulsed array system can be utilised in a wide range of non-destructive testing scenarios.

7.3 Scattering Considerations and Limitations

Whilst it has been seen that the pulsed array system of locating defects, through the measurement of the time-frequency characteristics of scattered waves, can be used in a range of scenarios, the method has a number of limitations that restrict

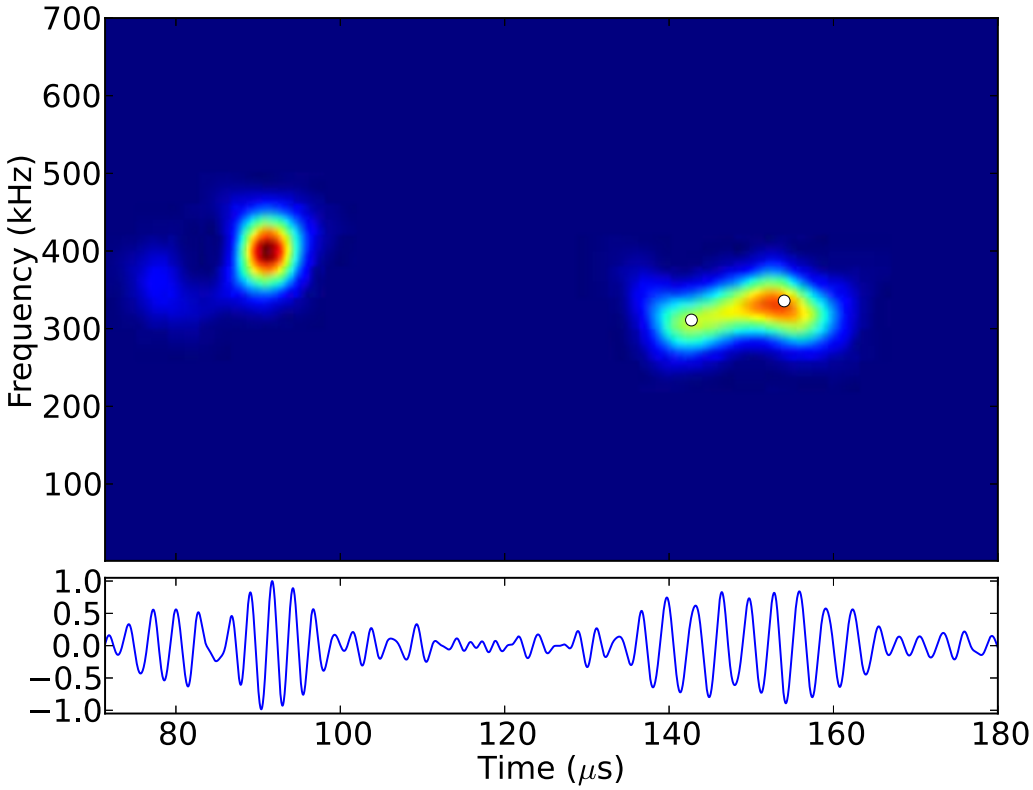

Figure 7.13: The measured displacement signal and the spectrogram showing the time localised frequency of the reflections from the sample containing a rough crack. The reflections from the end of the sample, at times of approximately 140 μs and 155 μs, are marked with circles to indicate they are not scattered signals from defects. The scattered signal indication can be seen at 90 μs, and has a frequency of around 400 kHz.

its usage. Firstly, the simultaneous excitation of the array necessarily generates a wavefront with symmetry, such that the wavefront propagates with equal magnitude in the $\pm\theta$ direction. As the frequency variation is also symmetric about $\theta = 0°$, by using pulse-echo measurements it is not possible to determine on which side of the array the defect is located. The symmetry of the situation can be broken by using a separate reception transducer, although this reduces the area of inspection due to the obscuration of the scattered signal by the direct wave and other waves reflected from the boundary of the sample.

The method of localising the angular position of the defect, through measuring the peak frequency component of the scattered signal, relies on the assumption that the scattering processes do not significantly affect the frequency content of the incoming signal. Despite the fact that it is known that ultrasonic scattering has a strong dependence upon both the frequency of the interrogating wave and the size of the scatterer, no shift in the frequency of the scattered wave has been observed. For the SDH, no frequency variation was observed due to the small angular size of the defect. If the SDH is modelled as an infinite cylinder, then the scattering processes can be calculated using Mie scattering algorithms [202–204]. This allows for the scattering intensity to be calculated for an arbitrarily sized cylinder. From the cylindrical symmetry of the scatterer, the scattered wave will be described by Bessel functions, with the scattering intensity being described by satisfying the boundary condition of the scatterer surface, which requires continuity of the stress and particle displacement vectors at the surface of the cylinder [191]. For shear horizontal waves, which do not mode-convert into other wave polarisations, the scattering cross-section of an infinitely long cylinder will only depend upon the ratio between the wavelength of the interrogating ultrasound and the radius of the cylinder [202]. This ratio is often expressed in terms of the dimensionless size parameter, $\alpha = ka$, where k is the SH wavenumber and a is the radius of the cylinder. Following analysis from the literature [191, 202], the scattering cross-section, normalised to the geometric

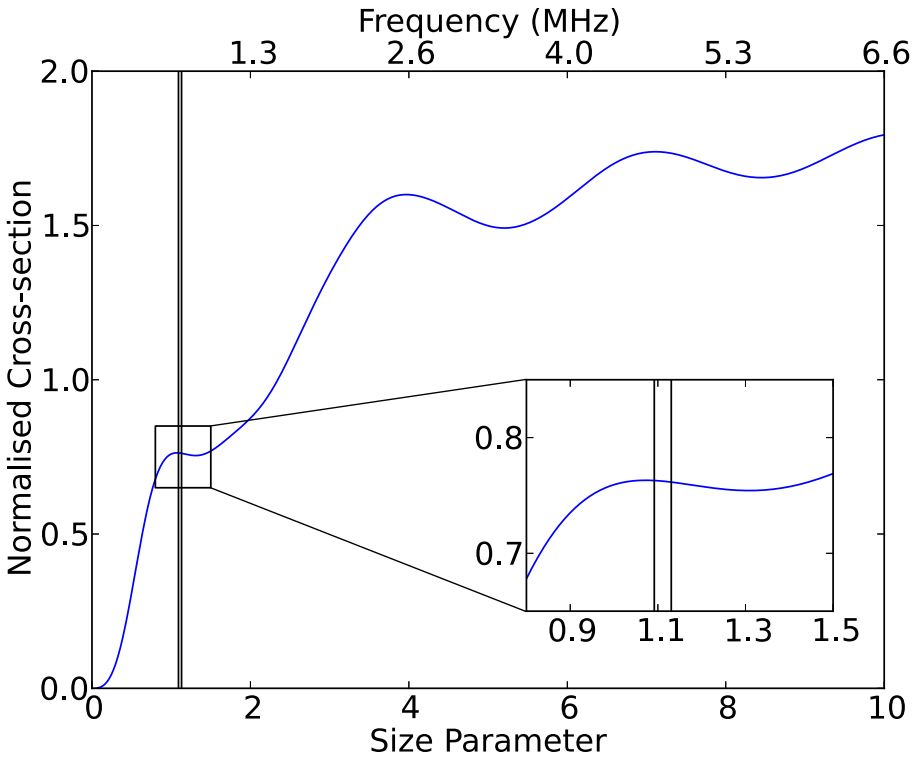

Figure 7.14: The normalised SH scattering cross-section has very complex relationship with the size parameter, α, and therefore frequency, ν. The range of possible size parameters for a small (0.75 mm radius, with an angular size of 2°) SDH, centred at $\theta = 45°$, is marked by two vertical lines. The inset shows that for such a defect, being inspected by a wavefront generated by a 3 mm pitch PPM EMAT, the scattering processes can be assumed to be frequency independent.

cross-section of the cylinder, of a 0.75 mm SDH for SH waves can be calculated.

This is shown in figure 7.14, which shows a very complex relationship between the size parameter, and therefore frequency, and normalised scattering cross-section. Also, shown in figure 7.14 is the range of size parameter for a SDH with a radius of 0.75 mm, that is centred at 45° relative to the centre of the pulsed array and has an angular size of 2°. Due to this angular size and the angularly varying frequency, the SDH will have a range of frequencies incident upon it; this angular bandwidth leads to a range of size parameters, which must be considered in order to accurately predict the scattering behaviour. The two vertical lines at $\alpha = 1.09$ and $\alpha = 1.13$ correspond to the size parameter for a 0.75 mm radius cylinder, given the peak frequency component of the wave at 46° and 44°, respectively. Of course, the signal

at a single point has an inherent bandwidth due to its finite temporal extent, and this will act to blur the limits shown in figure 7.14, but they still act as a good approximation. From inspecting figure 7.14, it is clear that the assumption of local frequency-independence can be assumed, as the cross-section does not significantly vary over the limits shown. However, it is equally clear that this is only locally true; if the angular size of the SDH is increased, then so does the range of size parameters that must be considered, leading to the frequency dependence of the scattering cross-section becoming more significant.

The resolution of the measurements should also be mentioned. As the frequency of the wave does not vary linearly with the angle of propagation, there will be an angularly dependent resolution associated with the location of the angular position of the defect. This is seen within the obtained results, with the error associated with the angular position of the defects being much larger when it is located near the surface, when compared to lower angles. This can be seen by differentiating the diffraction grating equation:

$$|\mathrm{d}\theta| = \left|\frac{\partial\theta}{\partial\nu}\right| \mathrm{d}\nu = \frac{d\sin^2\theta}{c\cos\theta}\mathrm{d}\nu. \tag{7.10}$$

From figure 7.15, the variation in angular uncertainty can be seen. Despite varying greatly, it should be noticed that the angular uncertainty in the estimated defect position, for a 3 mm pitch array, is less than a degree all angular positions $\theta \leq 75°$, before increasing rapidly due to the singularity in equation 7.10 at $\theta = 90°$. The predicted uncertainties seem to be particularly pessimistic for direct waves, as the measured angle of propagation for waves near the surface appears to much more precise than those shown in figure 7.15.

Ultimately, the uncertainty in the angular position of the defect is limited by the resolution that can be obtained in measuring the frequency of the scattered wave. Therefore, whilst the STFT approach has given sufficient time-frequency resolution for the measurements undertaken in this chapter, more advanced techniques

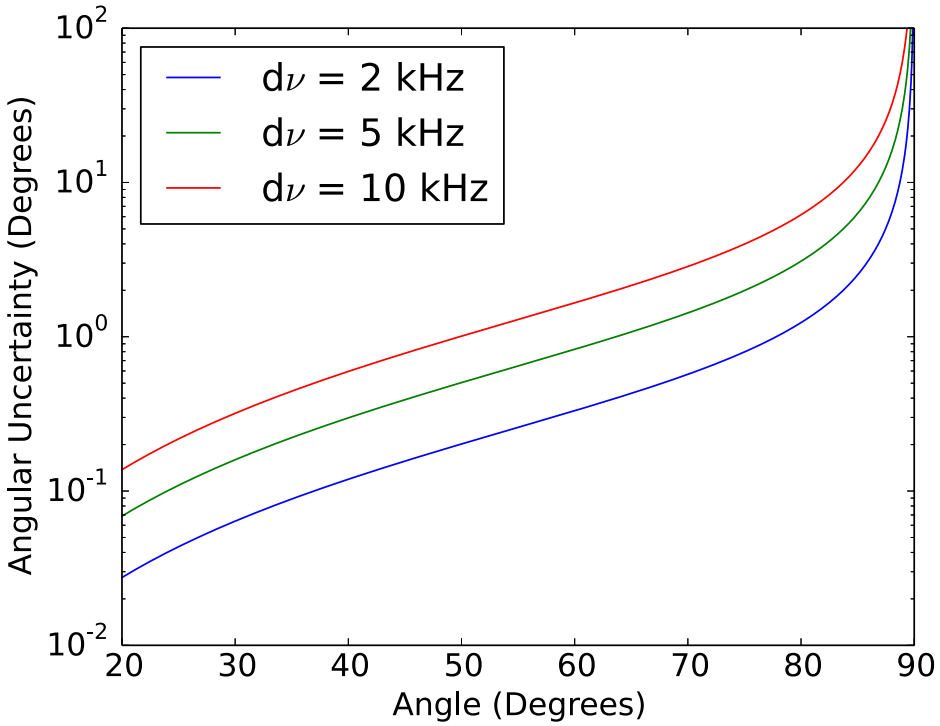

Figure 7.15: The angular uncertainty for a 3 mm pitch array over a range angular positions for a given frequency uncertainty, dν.

of time-frequency analysis can be applied in order to improve this resolution. Other methods of time-frequency analysis, such as discrete wavelet analysis, benefit from the advantage of multi-resolution analysis, which offers improved temporal resolution of the high frequency components, and frequency resolution of the low frequency components [195, 196, 205].

7.4 Conclusions

This chapter has highlighted how the interesting physical phenomenon of the wavefront with a continuously varying frequency can be applied for practical NDT applications. As the pulsed array wavefront propagates through the sample, it will be scattered by any defects that may be present. The frequency of this scattered wave will depend upon the angular position of the defect, relative to the centre of the array, whilst the time of flight measurements indicate the radial distance of the defect.

This was experimentally verified using a range of measurements and configurations, and on a variety of different samples. By using this approach, a discontinuity can be localised, in terms of its polar co-ordinates, with a single measurement.

For example, a pitch-catch experiment was constructed, with a PPM EMAT array used to generate the wavefront, with a separate linear coil EMAT that is sensitive to SH waves, used to detect the scattered wave. By using a separate transducer, it is possible to ascertain which side of the array the defect is on, as the transducer breaks the inherent symmetry of the array and generated wavefront. However, this does lead to a limited range of inspection, as the direct wave and reflections of the sample boundary can obscure the scattered wave, making analysis impossible. Despite this, it was demonstrated that a defect could be located with a single measurement of the time-frequency characteristics of the scattered wave, over a range of angles.

In order to solve the problems associated with the obscuration of the scattered wave, a single array is used to both generate the wavefront and detect the scattered wave. For this pulse-echo configuration, both the narrowband frequency sweep sector scan and the broadband pulsed method were used to inspect an aluminium sample, with a 10 mm deep notch acting as a defect. Whilst only one defect was present, there were are a number of multiple skip paths the ultrasound could take to the notch, due to the limited depth of the sample. This provides the ability to detect and locate defects over a range of angles.

The pulsed method has various advantages over the frequency sweep approach. Firstly, a single scan can cover a large angular range ($20° \leq \theta \leq 90°$), whereas the frequency sweep approach requires multiple measurements over a range of different frequencies. The pulsed measurements also appear to have superior accuracy and resolution, with the resolution of the pulsed approach limited by frequency resolution of the spectrogram, rather than the beam width, as is the case for the frequency steering. The pulsed wavefront is also continuous over the entire angular range of

interest, meaning more information is available than the frequency steering case, which effectively samples at discrete angles. Perhaps surprisingly, the drop in peak wave amplitude, associated with spreading the ultrasonic energy over a large range of angles, does not result in a dramatic reduction of the signal to noise ratio, mainly because the noise is distributed over a large range of frequencies, whereas the signal is obviously fairly narrowband in comparison.

As the pulsed array performance was shown to be superior to the frequency steering approach, it was used to inspect another sample with a real defect. It was shown that the combination of time of flight and frequency could still be used to locate this rough defect, despite the reduction in the amplitude of any reflections. The rough defect also appeared to have no strong frequency dependence in its scattering processes, implying that the frequency of the scattered wave can still be used to infer the angular position of a defect, even if it is not smooth. This demonstrates that the pulsed array method has the potential for use on industrial samples.

Whilst this approach has many advantages, especially given its simplicity of operation, there are a number of limitations that must be considered. The results obtained here indicate that there are no processes that strongly affect the frequency content of the scattered wave. For instance, it was shown that the position of the peak in the frequency spectrum of signal was not significantly altered, as it was scattered by the 0.75 mm radius SDH. Due to the small size of the defect, it acted similar to a point scatterer. Consequently, the angular bandwidth of the scattered signal remained small, and the scattering process could be assumed to be locally independent. However, as the defect gets larger, the range of frequencies incident on the defect increases, which allows for an increased possibility of frequency dependent scattering events, and these scattering events must be modelled in order to correctly locate defects through this method. The available resolution of this approach was also discussed, as well as the possibility of the resolution being improved through the use of more sophisticated time-frequency representations.

Chapter 8

Conclusions

8.1 Summary

The interest in phased array methods, and the extension of the approach to a range of applications, has been growing in recent years. As discussed in Section 2.3.3, the ultrasonic beam generated by the array can be controlled in a multitude of ways by adjusting the timing associated with the firing of the individual elements that make up the array. By applying appropriate delays, the ultrasonic energy can be electronically steered and focused to a desired position, which leads to improved resolution, sensitivity and versatility of the ultrasonic inspection. However, the requirement to be able to independently control individual elements adds significant hardware and software complexity to the operation of the array. Hence, it is desirable to retain some of the steering capabilities of the phased array, whilst removing the associated complexity. This can be achieved by utilising the periodic structure of the ultrasonic array along with simultaneous excitation of the array elements. As shown in Chapter 3, the ultrasonic beam can be steered by driving the array with a narrowband signal as the waves produced by each element interfere with each other. This leads to constructive interference at a particular angle, which is determined by the periodicity of the array and the frequency of the narrowband

signal. As the condition for constructive interference occurs when the path length difference between two waves generated from elements of the same polarity is equal to an integer number of wavelengths, the angle of constructive interference can be controlled by simply varying the excitation frequency. Consequently, it is possible to steer the ultrasonic beam without having the complications associated with phased array techniques. This principle has been demonstrated in a range of experimental configurations [69,70,98,101,160,161], showing how a whole host of ultrasonic waves can be steered by simultaneous excitation of an array.

Yet, this thesis is concerned with the another way of utilising the spatial periodicity of ultrasonic arrays. By simultaneously driving the array elements with a broadband signal of the appropriate frequency content, a wavefront is generated over a large range of solid angles. The frequency of the wavefront was also found to vary smoothly as a function of propagation angle. Initially, the attention of this work was on understanding and modelling the generated wavefront. It was found that many parallels could be drawn between the pulsed array and diffraction gratings, but with the polarity of the array elements having an alternating structure. Thus, by simultaneously actuating the array with a broadband signal containing specific frequency content, the waves from the individual elements interfere to form the wavefront with a frequency that continuously varies with angle. The use of finite element models and experimental measurements confirmed the frequency dependence of pulsed arrays, as predicted by the analytic models.

Using the wavefront, a defect can be localised in terms of polar co-ordinates by measuring the frequency and time of flight of the scattered wave. Hence, a defect can be positioned with just a single measurement. This is not true for traditional ultrasonic measurements, which normally only utilise time of flight information, as it is only possible to locate the position of the scatterer upon the surface on an ellipse. Consequently, several measurements are required to fully localise any defect through the intersection of many of these ellipsoidal loci. The principle of time-frequency

localisation is experimentally verified in Chapter 7, with measurements on a range of samples illustrating the method's validity. Experimental pulse-echo scattering data obtained from the pulsed array, along with a form of time-frequency analysis, can be used to create two-dimensional map of the sample.

8.2 Suggested further work

This thesis has developed the idea of using the spatial periodicity of ultrasonic arrays in order to generate a wavefront with many interesting features, and has shown how these features can be utilised in order to locate a defect. However, still more work is required in order to make this new approach a widely applicable method. In particular, it was shown in section 7.3 how, even though the scattering cross-section is highly dependent upon both the relative size of the defect and the interrogating wavelength, the scattering processes can be assumed to be locally frequency independent. However, this restricts the use of the pulsed array measurements to small defects, so that the frequency of the scattered wave accurately portrays the angular position of the defect. In order to reliably localise an arbitrarily sized defect, the scattering processes must be fully modelled. Whilst it is possible to analytically model broadband scattering events for many representative shapes, such as cylinders [204], the angular bandwidth is assumed to be constant in these models. In the case of the pulsed array wavefront, this is obviously not true as the frequency content of the signal incident upon the scatterer changes with angle.

Consequently, it is desirable to construct a scattering model that takes into account the angular variation in the bandwidth of the incoming signal. By doing so, not only would it allow for accurate angular positioning of the defect, but it could also be used to size the defect as well. Currently, only the peak frequency component is utilised in order to locate the angular position of the scatterer; all of the other information about the spectrum of the scattered wave is discarded. *A*

priori, it might be thought that the backscattered signal from large defect would have a greater bandwidth than from a smaller defect, and hence the bandwidth of the scattered signal might be directly related to size of the defect. Whilst this will not be entirely correct, the frequency spectrum will contain some valuable information about the size of the defect. Further work could be conducted in order to ascertain methods of obtaining size information from these scattered signals.

A relatively simple avenue of research to explore would to be investigate the various forms of time-frequency analysis that could be used to identify the time localised frequency of the scattered signals. In Chapter 7, short-time Fourier transforms were used to decompose the acquired signals into time-frequency maps. These could be converted into polar co-ordinates and used to identify the location of scatterers. However, whilst all of the echoes in the experimental data could be clearly resolved in both time and frequency, the STFT suffers from a fixed resolution. This means that there is an implicit compromise between the obtainable frequency resolution and time resolution. Other methods of time-frequency analysis, such as discrete wavelet analysis, benefit from the advantage of multi-resolution analysis, which offers improved temporal resolution of the high frequency components, and frequency resolution of the low frequency components [205]. There have been extensive studies in this area [195, 206, 207], which will aid the investigation to find the appropriate tool for time-frequency analysis.

Finally, whilst the work in this thesis has been focused on the generation of the pulsed wavefront with shear horizontal waves, the physics that describes the pulsed array system can be seen as a general wave phenomenon. Indeed, the analytic model constructed in Chapter 4 made no assumptions about the nature of the array elements, considering them simply as point sources being driven by a particular impulse. Consequently, it should be possible to create similar wavefront, with the same frequency variation properties, using other wave modes, such as longitudinal ultrasonic waves or electromagnetic waves. Future work could include experimental

verification that such a wavefront could be generated using radar, sonar, or longitudinal ultrasonic systems.

References

[1] B. Drinkwater and P. Wilcox., "Ultrasonic arrays for non-destructive evaluation: A review," *NDT&E International*, vol. 39, pp. 525 – 541, 2006.

[2] A. McNab and M. Campbell, "Ultrasonic phased arrays for nondestructive testing," *NDT International*, vol. 20, no. 6, pp. 333 – 337, 1987.

[3] L. Azar, Y. Shi, and S.-C. Wooh, "Beam focusing behavior of linear phased arrays," *NDT&E International*, vol. 33, no. 3, pp. 189 – 198, 2000.

[4] D. E. Bray and D. McBride, *Nondestructive Testing Techniques*. John Wiley & Sons, 1992.

[5] B. Hull and V. John, *Non-Destructive Testing*. MacMillan Education, 1988.

[6] W. J. McGonnagle, *Nondestructive Testing*. Gordon and Breach Science Publishers, 1982.

[7] S. Dixon, C. Edwards, and S. Palmer, "High accuracy non-contact ultrasonic thickness gauging of aluminium sheet using electromagnetic acoustic transducers," *Ultrasonics*, vol. 39, no. 6, pp. 445 – 453, 2001.

[8] S. Dixon, P. A. Petcher, Y. Fan, D. Maisey, and P. Nickolds, "Ultrasonic metal sheet thickness measurement without prior wave speed calibration," *Journal of Physics D: Applied Physics*, vol. 46, no. 44, p. 445502, 2013.

[9] R. Ghaedian, J. N. Coupland, E. A. Decker, and D. J. McClements, "Ultrasonic determination of fish composition," *Journal of Food Engineering*, vol. 35, no. 3, pp. 323 – 337, 1998.

[10] C. M. Avesani, S. A. Draibe, M. A. Kamimura, M. Cendoroglo, A. Pedrosa, M. L. Castro, and L. Cuppari, "Assessment of body composition by dual energy X-ray absorptiometry, skinfold thickness and creatinine kinetics in chronic kidney disease patients," *Nephrology Dialysis Transplantation*, vol. 19, no. 9, pp. 2289 – 2295, 2004.

[11] R. Halmshaw, *Non-Destructive Testing.* Edward Arnold, 1991.

[12] J. E. Lenz, "A review of magnetic sensors," *Proceedings of the IEEE*, vol. 78, no. 6, pp. 973 – 989, Jun 1990.

[13] K. Bainton, "Characterizing defects by determining magnetic leakage fields," *NDT International*, vol. 10, no. 5, pp. 253 – 257, 1977.

[14] D. H. Michael, A. M. Lewis, M. McIver, and R. Collins, "Thin-skin electromagnetic fields in the neighbourhood of surface-breaking cracks in metals," *Proceedings of the Royal Society of London. Series A: Mathematical and Physical Sciences*, vol. 434, no. 1892, pp. 587 – 603, 1991.

[15] D. Mukherjee, S. Saha, and S. Mukhopadhyay, "Inverse mapping of magnetic flux leakage signal for defect characterization," *NDT&E International*, vol. 54, pp. 198 – 208, 2013.

[16] D. E. Bray and R. K. Stanley, *Nondestructive Evaluation. A tool in design, manufacturing and service.* CRC Press, 1997.

[17] H. Wheeler, "Formulas for the skin effect," *Proceedings of the IRE*, vol. 30, no. 9, pp. 412 – 424, 1942.

[18] B. Lebrun, Y. Jayet, and J.-C. Baboux, "Pulsed eddy current signal analysis: application to the experimental detection and characterization of deep flaws in highly conductive materials," *NDT& E International*, vol. 30, no. 3, pp. 163 – 170, 1997.

[19] R. Grimberg, L. Udpa, A. Savin, R. Steigmann, V. Palihovici, and S. S. Udpa, "2D eddy current sensor array," *NDT&E International*, vol. 39, no. 4, pp. 264 – 271, 2006.

[20] D. P. Almond and S. K. Lau, "Defect sizing by transient thermography. I. An analytical treatment," *Journal of Physics D: Applied Physics*, vol. 27, no. 5, pp. 1063 – 1069, 1994.

[21] D. Titman, "Applications of thermography in non-destructive testing of structures," *NDT&E International*, vol. 34, no. 2, pp. 149 – 154, 2001.

[22] W. J. Parker, R. J. Jenkins, C. P. Butler, and G. L. Abbott, "Flash method of determining thermal diffusivity, heat capacity, and thermal conductivity," *Journal of Applied Physics*, vol. 32, no. 9, pp. 1679 – 1684, 1961.

[23] S. Burrows, S. Dixon, S. Pickering, T. Li, and D. Almond, "Thermographic detection of surface breaking defects using a scanning laser source," *NDT&E International*, vol. 44, no. 7, pp. 589 – 596, 2011.

[24] R. Hanke, T. Fuchs, and N. Uhlmann, "X-ray based methods for non-destructive testing and material characterization," *Nuclear Instruments and Methods in Physics Research Section A: Accelerators, Spectrometers, Detectors and Associated Equipment*, vol. 591, no. 1, pp. 14 – 18, 2008, radiation Imaging Detectors 2007 Proceedings of the 9th International Workshop on Radiation Imaging Detectors.

[25] J. Blitz and G. Simpson, *Ultrasonic methods of non-destructive testing.* Chapman & Hall, 1996.

[26] J. D. N. Cheeke, *Fundamentals and Applications of Ultrasonic Waves*. CRC Press, 2002.

[27] J. L. Rose, *Ultrasonic Waves in Solid Media*. Cambridge University Press, 1999.

[28] J. Achenbach, *Wave Propagation in elastic solids*, H. A. Lauwerier and W. Koiter, Eds. North-Holland Publishing Company, 1973.

[29] B. A. Auld, *Acoustic fields and waves in solids*. Krieger Publishing, 1990, vol. 1.

[30] F. S. Crawford, *Waves: Berkeley physics course*. McGraw-Hill, London, 1968.

[31] P. M. Morse, *Vibrations and Sound*. McGraw-Hill, London, 1948.

[32] A. P. French, *Vibrations and waves*. Chapman and Hall, 1991.

[33] K. Riley, M. Hobson, and S. Bence, *Mathematical Methods for Physics and Engineering*. Cambridge University Press, 2006.

[34] J. Achenbach, "Quantitative nondestructive evaluation," *International Journal of Solids and Structures*, vol. 37, no. 1, pp. 13 – 27, 2000.

[35] J. P. Charlesworth and J. A. G. Temple, *Engineering Applications of Ultrasonic Time-of-Flight Diffraction*, 2nd ed., ser. Ultrasonic Inspection In Engineering, M. J. Whittle, Ed. Baldock, UK: Research Studies Press, 2001.

[36] B. A. Auld, *Acoustic fields and waves in solids*. Krieger Publishing, 1990, vol. 2.

[37] M. Fukuhara and Y. Kuwano, "Propagation characteristics of SH ultrasonic waves through the surface depth of an isotropic medium," *NDT&E International*, vol. 31, no. 3, pp. 201 – 210, 1998.

[38] C. F. Vasile and R. B. Thompson, "Excitation of horizontally polarized shear elastic waves by electromagnetic transducers with periodic permanent magnets," *Journal of Applied Physics*, vol. 50, no. 4, pp. 2583 – 2588, 1979.

[39] M. Born, *Principles of Optics: Electromagnetic Theory of Propagation, Interference and diffraction of light.* Cambridge University Press, Cambridge, 1999.

[40] S. Hirsekorn, "The scattering of ultrasonic waves by polycrystals," *The Journal of the Acoustical Society of America*, vol. 72, no. 3, pp. 1021 –1031, 1982.

[41] W. N. Reynolds and R. L. Smith, "Ultrasonic wave attenuation spectra in steels," *Journal of Physics D: Applied Physics*, vol. 17, no. 1, pp. 109 –116, 1984.

[42] E. P. Papadakis, "Ultrasonic attenuation caused by scattering in polycrystalline metals," *The Journal of the Acoustical Society of America*, vol. 37, no. 4, pp. 711 – 717, 1965.

[43] Q. Liu, D. J. Jensen, and N. Hansen, "Effect of grain orientation on deformation structure in cold-rolled polycrystalline aluminium," *Acta Materialia*, vol. 46, no. 16, pp. 5819 – 5838, 1998.

[44] E. P. Papadakis, "Revised grain-scattering formulas and tables," *The Journal of the Acoustical Society of America*, vol. 37, no. 4, pp. 703 – 710, 1965.

[45] K. Lücke, "Ultrasonic attenuation caused by thermoelastic heat flow," *Journal of Applied Physics*, vol. 27, no. 12, pp. 1433 – 1438, 1956.

[46] I. A. Viktorov, *Rayleigh and Lamb waves: Physical theory and applications.* Plenum Press, 1967.

[47] R. S. Edwards, B. Dutton, A. R. Clough, and M. H. Rosli, "Enhancement of ultrasonic surface waves at wedge tips and angled defects," *Applied Physics Letters*, vol. 99, no. 9, pp. 094 104–1 – 094 104–3, 2011.

[48] B. Dutton, A. Clough, M. Rosli, and R. Edwards, "Non-contact ultrasonic detection of angled surface defects," *NDT&E International*, vol. 44, no. 4, pp. 353 – 360, 2011.

[49] M. Rosli, R. Edwards, and Y. Fan, "In-plane and out-of-plane measurements of Rayleigh waves using EMATs for characterising surface cracks," *NDT&E International*, vol. 49, pp. 1 – 9, 2012.

[50] R. Edwards, S. Dixon, and X. Jian, "Characterisation of defects in the railhead using ultrasonic surface waves," *NDT&E International*, vol. 39, no. 6, pp. 468 – 475, 2006.

[51] R. S. Edwards, S. Dixon, and X. Jian, "Enhancement of the Rayleigh wave signal at surface defects," *Journal of Physics D: Applied Physics*, vol. 37, no. 16, pp. 2291 – 2297, 2004.

[52] F. Cegla, A. Jarvis, and J. Davies, "High temperature ultrasonic crack monitoring using SH waves," *NDT&E International*, vol. 44, no. 8, pp. 669 – 679, 2011.

[53] F. Cegla, P. Cawley, J. Allin, and J. Davies, "High-temperature (>500°C) wall thickness monitoring using dry-coupled ultrasonic waveguide transducers," *IEEE Transactions on Ultrasonics, Ferroelectrics and Frequency Control*, vol. 58, no. 1, pp. 156 – 167, 2011.

[54] R. B. King and C. M. Fortunko, "Determination of in-plane residual stress states in plates using horizontally polarized shear waves," *Journal of Applied Physics*, vol. 54, no. 6, pp. 3027 – 3035, 1983.

[55] Nurmalia, N. Nakamura, H. Ogi, M. Hirao, and K. Nakahata, "Mode conversion behavior of SH guided wave in a tapered plate," *NDT&E International*, vol. 45, no. 1, pp. 156 – 161, 2012.

[56] Nurmalia, N. Nakamura, H. Ogi, and M. Hirao, "Detection of shear horizontal guided waves propagating in aluminum plate with thinning region," *Japanese Journal of Applied Physics*, vol. 50, no. 7, pp. 07HC17–1 – 07HC17–5, 2011.

[57] A. Demma, P. Cawley, and M. Lowe, "Scattering of the fundamental shear horizontal mode from steps and notches in plates," *The Journal of the Acoustical Society of America*, vol. 113, no. 4, pp. 1880–1891, 2003.

[58] J. J. Ditri, "Some results on the scattering of guided elastic SH waves from material and geometric waveguide discontinuities," *The Journal of the Acoustical Society of America*, vol. 100, no. 5, pp. 3078–3087, 1996.

[59] P. Rajagopal and M. J. S. Lowe, "Scattering of the fundamental shear horizontal guided wave by a part-thickness crack in an isotropic plate," *The Journal of the Acoustical Society of America*, vol. 124, no. 5, pp. 2895 – 2904, 2008.

[60] M. Castaings and B. Hosten, "Lamb and SH waves generated and detected by air-coupled ultrasonic transducers in composite material plates," *NDT&E International*, vol. 34, no. 4, pp. 249 – 258, 2001.

[61] P. Petcher, S. Burrows, and S. Dixon, "Shear horizontal (SH) ultrasound wave propagation around smooth corners," *Ultrasonics*, vol. 0, no. 0, pp. –, 2013.

[62] C. M. Fortunko, R. B. King, and M. Tan, "Nondestructive evaluation of planar defects in plates using low-frequency shear horizontal waves," *Journal of Applied Physics*, vol. 53, no. 5, pp. 3450 – 3458, 1982.

[63] J. Ogilvy, "Computerized ultrasonic ray tracing in austenitic steel," *NDT International*, vol. 18, no. 2, pp. 67 – 77, 1985.

[64] J. Ogilvy, "Ultrasonic beam profiles and beam propagation in an austenitic weld using a theoretical ray tracing model," *Ultrasonics*, vol. 24, no. 6, pp. 337 – 347, 1986.

[65] K. Sawaragi, H. Salzburger, G. Habschen, K. Enami, A. Kirihigashi, and N. Tachibana, "Improvement of SH-wave EMAT phased array inspection by new eight segment probes," *Nuclear Engineering and Design*, vol. 198, pp. 153 – 163, 2000.

[66] C. Fortunko and J. Moulder, "Ultrasonic inspection of stainless steel butt welds using horizontally polarized shear waves," *Ultrasonics*, vol. 20, no. 3, pp. 113 – 117, 1982.

[67] J. Ogilvy, "Ultrasonic reflection properties of planar defects within austenitic welds," *Ultrasonics*, vol. 26, no. 6, pp. 318 – 327, 1988.

[68] M. Hirao and H. Ogi, "An SH-wave EMAT technique for gas pipeline inspection," *NDT&E International*, vol. 32, no. 3, pp. 127 – 132, 1999.

[69] Y. Ohtsuka, M. Higashi, and M. Nishikawa, "Fundamental experiment for inspection of cooling pipes in operation by using ultrasonic technique," *Fusion Engineering and Design*, vol. 81, no. 8-14, pp. 1583 – 1587, 2006.

[70] W. J. Pardee and R. Thompson, "Half-space radiation by EMATs," *Journal of Nondestructive Evaluation*, vol. 1, no. 3, pp. 157 – 181, 1980.

[71] M. Hirao and H. Ogi, *EMATS for science and industry : Noncontacting ultrasonic measurements*. Kluwer Academic Publishers, 2003.

[72] H. Ogi, "Field dependence of coupling efficiency between electromagnetic field and ultrasonic bulk waves," *Journal of Applied Physics*, vol. 82, no. 8, pp. 3940 – 3949, 1997.

[73] R. M. Hornreich, H. Rubinstein, and R. J. Spain, "Magnetostrictive phenomena in metallic materials and some of their device applications," *IEEE Transactions on Magnetics*, vol. 7, no. 1, pp. 29 – 48, 1971.

[74] H. Young and R. A. Freedman, *University physics: with modern physics*. Pearson / Addison-Wesley, 2008.

[75] I. Grant and W. Phillips, *Electromagnetism*. John Wiley & Sons, 1991.

[76] S. Dixon and X. Jian, "Eddy current generation enhancement using ferrite for electromagnetic acoustic transduction," *Applied Physics Letters*, vol. 89, no. 19, pp. –, 2006.

[77] X. Jian and S. Dixon, "Enhancement of EMAT and eddy current using a ferrite back-plate," *Sensors and Actuators A: Physical*, vol. 136, no. 1, pp. 132 – 136, 2007.

[78] K. Kawashima, O. B. Wright, and T. Hyoguchi, "High frequency resonant electromagnetic generation and detection of ultrasonic waves," *Japanese Journal of Applied Physics*, vol. 33, no. Part 1, No. 5B, pp. 2837 – 2845, 1994.

[79] E. Dobbs and J. Llewellyn, "Generation of ultrasonic waves without using a transducer," *Non-Destructive Testing*, vol. 4, no. 1, pp. 49 – 56, 1971.

[80] K. Kawashima, "Quantitative calculation and measurement of longitudinal and transverse ultrasonic wave pulses in solid," *IEEE Transactions on Sonics and Ultrasonics*, vol. 31, no. 2, pp. 83 – 93, 1984.

[81] R. B. Thompson, "Generation of horizontally polarized shear waves in ferromagnetic materials using magnetostrictively coupled meander-coil

electromagnetic transducers," *Applied Physics Letters*, vol. 34, no. 2, pp. 175 – 177, 1979.

[82] C. Rouge, A. Lhémery, and D. Ségur, "Modal solutions for SH guided waves radiated by an EMAT in a ferromagnetic plate," *Journal of Physics: Conference Series*, vol. 353, no. 1, p. 012014, 2012.

[83] R. Ribichini, F. Cegla, P. Nagy, and P. Cawley, "Study and comparison of different EMAT configurations for SH wave inspection," *IEEE Transactions on Ultrasonics, Ferroelectrics and Frequency Control*, vol. 58, no. 12, pp. 2571 – 2581, 2011.

[84] R. Ribichini, F. Cegla, P. Nagy, and P. Cawley, "Experimental and numerical evaluation of electromagnetic acoustic transducer performance on steel materials," *NDT&E International*, vol. 45, no. 1, pp. 32 – 38, 2012.

[85] H. Ogi, E. Goda, and M. Hirao, "Increase of efficiency of magnetostriction SH-Wave electromagnetic acoustic transducer by angled bias field: Piezomagnetic theory and measurement," *Japanese Journal of Applied Physics*, vol. 42, no. Part 1, No. 5B, pp. 3020 – 3024, 2003.

[86] R. Thompson, "A model for the electromagnetic generation of ultrasonic guided waves in ferromagnetic metal polycrystals," *IEEE Transactions on Sonics and Ultrasonics*, vol. 25, no. 1, pp. 7 – 15, 1978.

[87] R. B. Thompson, "Mechanisms of electromagnetic generation and detection of ultrasonic Lamb waves in iron-nickel alloy polycrystals," *Journal of Applied Physics*, vol. 48, no. 12, pp. 4942 – 4950, 1977.

[88] E. W. Lee, "Magnetostriction and magnetomechanical effects," *Reports on Progress in Physics*, vol. 18, no. 1, pp. 184 –229, 1955.

[89] R. Thompson, "A model for the electromagnetic generation and detection of Rayleigh and Lamb waves," *IEEE Transactions on Sonics and Ultrasonics*, vol. 20, no. 4, pp. 340 – 346, 1973.

[90] S. Huang, W. Zhao, Y. Zhang, and S. Wang, "Study on the lift-off effect of EMAT," *Sensors and Actuators A: Physical*, vol. 153, no. 2, pp. 218 – 221, 2009.

[91] M. G. Silk, *Ultrasonic Transducers for Nondestructive Testing*. Adam Hilger Ltd, 1984.

[92] F. Hernandez-Valle and S. Dixon, "Initial tests for designing a high temperature EMAT with pulsed electromagnet," *NDT&E International*, vol. 43, no. 2, pp. 171 – 175, 2010.

[93] H. Gao and B. Lopez, "Development of single-channel and phased array electromagnetic acoustic transducers for austenitic weld testing," *Materials Evaluation*, vol. 68, pp. 821 – 827, 2010.

[94] D. K. Hsu, K.-H. Im, and I.-Y. Yang, "Applications of electromagnetic acoustic transducers in the NDE of non-conducting composite materials," *KSME International Journal*, vol. 13, no. 5, pp. 403 – 413, 1999.

[95] X. Jian, S. Dixon, R. Edwards, and J. Morrison, "Coupling mechanism of an EMAT," *Ultrasonics*, vol. 44, Supplement, pp. e653 – e656, 2006, proceedings of Ultrasonics International (UI05) and World Congress on Ultrasonics (WCU).

[96] C. B. Scruby, *Laser Ultrasonics: Techniques and Applications*. Adam Hilger Ltd, 1990.

[97] R. B. Thompson, *Ultrasonic Measurement Methods*, ser. Physical Acoustics. Academic Press Inc., 1990, vol. XIX, ch. Physical Principles of Measurements with EMAT Transducers, pp. 157 – 200.

[98] T. J. Moran and R. M. Panos, "Electromagnetic generation of electronically steered ultrasonic bulk waves," *Journal of Applied Physics*, vol. 47, no. 5, pp. 2225 – 2227, 1976.

[99] X. Jian, S. Dixon, K. Grattan, and R. Edwards, "A model for pulsed Rayleigh wave and optimal EMAT design," *Sensors and Actuators A: Physical*, vol. 128, no. 2, pp. 296 – 304, 2006.

[100] R. Dhayalan and K. Balasubramaniam, "A hybrid finite element model for simulation of electromagnetic acoustic transducer (EMAT) based plate waves," *NDT&E International*, vol. 43, no. 6, pp. 519 – 526, 2010.

[101] S. Hill and S. Dixon, "Frequency dependent directivity of periodic permanent magnet electromagnetic acoustic transducers," *NDT&E International*, vol. 62, pp. 137 – 143, 2014.

[102] S. Dixon, S. Hill, Y. Fan, and G. Rowlands, "The wave-field from an array of periodic emitters driven simultaneously by a broadband pulse," *The Journal of the Acoustical Society of America*, vol. 133, no. 6, pp. 3692 – 3699, 2013.

[103] T. Meeker, "Thickness mode piezoelectric transducers," *Ultrasonics*, vol. 10, pp. 26 – 36, 1972.

[104] G. Hayward, "Using a block diagram approach for the evaluation of electrical loading effects on piezoelectric reception," *Ultrasonics*, vol. 24, no. 3, pp. 156 – 163, 1986.

[105] Y. Estanbouli, G. Hayward, N. Ramadas, and J. Barbenel, "A block diagram model of the thickness mode piezoelectric transducer containing dual

oppositely polarized piezoelectric zones," *IEEE Transactions on Ultrasonics, Ferroelectrics and Frequency Control*, vol. 53, no. 5, pp. 1028 – 1036, 2006.

[106] R. Lerch, "Finite element analysis of piezoelectric transducers," in *Ultrasonics Symposium, 1988. Proceedings., IEEE 1988*, 1988, pp. 643 – 654.

[107] C. Desilets, J. Fraser, and G. S. Kino, "The design of efficient broad-band piezoelectric transducers," *IEEE Transactions on Sonics and Ultrasonics*, vol. 25, no. 3, pp. 115 – 125, 1978.

[108] G. Hayward and J. Hossack, "Unidimensional modeling of 1-3 composite transducers," *The Journal of the Acoustical Society of America*, vol. 88, pp. 599 – 608, 1990.

[109] J. A. Hossack and G. Hayward, "Finite-element analysis of 1-3 composite transducers," *IEEE Transactions on Ultrasonics, Ferroelectrics and Frequency Control*, vol. 38, pp. 618 – 629, 1991.

[110] G. Kossoff, "The effects of backing and matching on the performance of piezoelectric ceramic transducers," *IEEE Transactions on Sonics and Ultrasonics*, vol. SU-13, pp. 20 – 30, 1966.

[111] A. J. Mulholland, N. Ramadas, R. L. O'Leary, A. C. S. Parr, G. Hayward, A. Troge, and R. A. Pethrick, "Enhancing the performance of piezoelectric ultrasound transducers by the use of multiple matching layers," *IMA Journal of Applied Mathematics*, vol. 73, no. 6, pp. 936 – 949, 2008.

[112] D. Hutchins, C. Saleh, M. Moles, and B. Farahbahkhsh, "Ultrasonic NDE using a concentric laser/EMAT system," *Journal of Nondestructive Evaluation*, vol. 9, no. 4, pp. 247 – 261, 1990.

[113] D. A. Hutchins, "Mechanisms of pulsed photoacoustic generation," *Canadian Journal of Physics*, vol. 64, no. 9, pp. 1247 – 1264, 1986.

[114] J. Ogilvy and J. Temple, "Diffraction of elastic waves by cracks: Application to time-of-flight inspection," *Ultrasonics*, vol. 21, no. 6, pp. 259 – 269, 1983.

[115] P. Petcher and S. Dixon, "Parabola detection using matched filtering for ultrasound B-scans," *Ultrasonics*, vol. 52, no. 1, pp. 138 – 144, 2012.

[116] M. Spies, H. Rieder, A. Dillhöfer, V. Schmitz, and W. Müller, "Synthetic aperture focusing and time-of-flight diffraction ultrasonic imaging - past and present," *Journal of Nondestructive Evaluation*, vol. 31, no. 4, pp. 310 – 323, 2012.

[117] Y.-F. Chang and C.-I. Hsieh, "Time of flight diffraction imaging for double-probe technique," *IEEE Transactions on Ultrasonics, Ferroelectrics and Frequency Control*, vol. 49, no. 6, pp. 776 – 783, 2002.

[118] G. Baskaran, K. Balasubramaniam, and C. L. Rao, "Shear-wave time of flight diffraction (S-TOFD) technique," *NDT&E International*, vol. 39, no. 6, pp. 458 – 467, 2006.

[119] P. Petcher and S. Dixon, "A modified Hough transform for removal of direct and reflected surface waves from B-scans," *NDT&E International*, vol. 44, no. 2, pp. 139 – 144, 2011.

[120] F. Cegla, "Ultrasonic crack monitoring using SH waves in extreme and inaccessible environments," in *17th World Conference on Nondestructive Testing*. Citeseer, 2008.

[121] S. Doctor, T. Hall, and L. Reid, "SAFT - the evolution of a signal processing technology for ultrasonic testing," *NDT International*, vol. 19, no. 3, pp. 163 – 167, 1986.

[122] Y. Ozaki, H. Sumitani, T. Tomoda, and M. Tanaka, "A new system for real-time synthetic aperture ultrasonic imaging," *IEEE Transactions on Ultrason-*

ics, Ferroelectrics and Frequency Control, vol. 35, no. 6, pp. 828 – 838, nov 1988.

[123] K. Langenberg, M. Berger, T. Kreutter, K. Mayer, and V. Schmitz, "Synthetic aperture focusing technique signal processing," *NDT International*, vol. 19, no. 3, pp. 177 – 189, 1986.

[124] A. Velichko and P. D. Wilcox, "An analytical comparison of ultrasonic array imaging algorithms," *The Journal of the Acoustical Society of America*, vol. 127, no. 4, pp. 2377 – 2384, 2010.

[125] A. Blouin, D. Levesque, C. Neron, D. Drolet, and J.-P. Monchalin, "Improved resolution and signal-to-noise ratio in laser-ultrasonics by SAFT processing," *Opt. Express*, vol. 2, no. 13, pp. 531 – 539, Jun 1998.

[126] M. Karaman, P.-C. Li, and M. O'Donnell, "Synthetic aperture imaging for small scale systems," *IEEE Transactions on Ultrasonics, Ferroelectrics and Frequency Control*, vol. 42, no. 3, pp. 429 – 442, May 1995.

[127] J. Davies, F. Simonetti, M. Lowe, and P. Cawley, "Review of synthetically focused guided wave imaging techniques with application to defect sizing," *AIP Conference Proceedings*, vol. 820, no. 1, pp. 142 – 149, 2006.

[128] O. Martinez, M. Parrilla, M. Izquierdo, and L. Ullate, "Application of digital signal processing techniques to synthetic aperture focusing technique images," *Sensors and Actuators A: Physical*, vol. 76, no. 1-3, pp. 448 – 456, 1999.

[129] J. Opretzka, M. Vogt, and H. Ermert, "A synthetic aperture focusing technique with optimized beamforming for high-frequency ultrasound," in *Ultrasonics Symposium (IUS), 2010 IEEE*, Oct 2010, pp. 2303 – 2306.

[130] S. Burch, "Comparison of SAFT and two-dimensional deconvolution methods for the improvement of resolution in ultrasonic B-scan images," *Ultrasonics*, vol. 25, no. 5, pp. 259 – 266, 1987.

[131] C. Frazier and W. O'Brien, "Synthetic aperture techniques with a virtual source element," *IEEE Transactions on Ultrasonics, Ferroelectrics and Frequency Control*, vol. 45, no. 1, pp. 196 – 207, Jan 1998.

[132] K. Nagai, "A new synthetic-aperture focusing method for ultrasonic B-scan imaging by the Fourier transform," *IEEE Transactions on Sonics and Ultrasonics*, vol. 32, no. 4, pp. 531 – 536, July 1985.

[133] F. Lingvall, T. Olofsson, and T. Stepinski, "Synthetic aperture imaging using sources with finite aperture: Deconvolution of the spatial impulse response," *The Journal of the Acoustical Society of America*, vol. 114, no. 1, pp. 225 – 234, 2003.

[134] L. Busse, "Three-dimensional imaging using a frequency-domain synthetic aperture focusing technique," *IEEE Transactions on Ultrasonics, Ferroelectrics and Frequency Control*, vol. 39, no. 2, pp. 174 – 179, March 1992.

[135] J.-H. Lee and S.-W. Choi, "A parametric study of ultrasonic beam profiles for a linear phased array transducer," *IEEE Transactions on Ultrasonics, Ferroelectrics and Frequency Control*, vol. 47, no. 3, pp. 644 – 650, 2000.

[136] O. V. Ramm and S. Smith, "Beam steering with linear arrays," *IEEE Transactions on Biomedical Engineering*, vol. BME-30, pp. 438 – 452, 1983.

[137] J.-Y. Lu, H. Zou, and J. F. Greenleaf, "Biomedical ultrasound beam forming," *Ultrasound in Medicine & Biology*, vol. 20, no. 5, pp. 403 – 428, 1994.

[138] D. H. Turnbull and F. S. Foster, "Beam steering with pulsed two-dimensional transducer arrays," *IEEE Transactions on Ultrasonics, Ferroelectrics and Frequency Control*, vol. 38, no. 4, pp. 320 – 333, July 1991.

[139] S.-C. Wooh and Y. Shi, "Optimum beam steering of linear phased arrays," *Wave Motion*, vol. 29, no. 3, pp. 245 – 265, 1999.

[140] C. Holmes, B. Drinkwater, and P. Wilcox., "Post-processing of the full matrix of ultrasonic transmit-receive array data for non-destructive evaluation," *NDT&E International*, vol. 38, pp. 701 – 711, 2005.

[141] J. A. Johnson, M. Karaman, and B. T. Khuri-Yakub, "Coherent-array imaging using phased subarrays. Part I: Basic principles," *IEEE Transactions on Ultrasonics, Ferroelectrics and Frequency Control*, vol. 52, pp. 37 – 50, 2005.

[142] W. Smith and B. Auld, "Modeling 1-3 composite piezoelectrics: thickness-mode oscillations," *IEEE Transactions on Ultrasonics, Ferroelectrics and Frequency Control*, vol. 38, no. 1, pp. 40 – 47, 1991.

[143] R. Farlow, W. Galbraith, M. Knowles, and G. Hayward, "Micromachining of a piezocomposite transducer using a copper vapor laser," *IEEE Transactions on Ultrasonics, Ferroelectrics and Frequency Control*, vol. 48, pp. 639 – 640, 2001.

[144] R. Newnham, L. Bowen, K. Klicker, and L. Cross, "Composite piezoelectric transducers," *Materials & Design*, vol. 2, no. 2, pp. 93 – 106, 1980.

[145] E. Hecht, *Optics*. Addison-Wesley, 1997.

[146] S.-J. Song, H. Shin, and Y. Jang, "Development of an ultra sonic phased array system for nondestructive tests of nuclear power plant components," *Nuclear Engineering and Design*, vol. 214, pp. 151 – 161, 2002.

[147] J. W. Goodman, *Introduction to Fourier Optics*. Roberts & Company, 2005, vol. 3rd.

[148] S.-C. Wooh and Y. Shi, "Three-dimensional beam directivity of phase-steered ultrasound," *The Journal of the Acoustical Society of America*, vol. 105, no. 6, pp. 3275 – 3282, 1999.

[149] F. J. Pompei and S.-C. Wooh, "Phased array element shapes for suppressing grating lobes," *The Journal of the Acoustical Society of America*, vol. 111, no. 5, pp. 2040 – 2048, 2002.

[150] G. F. Miller and H. Pursey, "The field and radiation impedance of mechanical radiators on the free surface of a semi-infinite isotropic solid," *Proceedings of the Royal Society of London. Series A. Mathematical and Physical Sciences*, vol. 223, no. 1155, pp. 521 – 541, 1954.

[151] F. C. Laing and A. B. Kurtz, "The importance of ultrasonic side-lobe artifacts," *Radiology*, vol. 145, no. 3, pp. 763 – 768, 1982.

[152] S.-C. Wooh and Y. Shi, "Influence of phased array element size on beam steering behavior," *Ultrasonics*, vol. 36, no. 6, pp. 737 – 749, 1998.

[153] B. Steinberg, "Comparison between the peak sidelobe of the random array and algorithmically designed aperiodic arrays," *IEEE Transactions on Antennas and Propagation*, vol. 21, no. 3, pp. 366 – 370, May 1973.

[154] S. I. Nikolov and J. A. Jensen, "Application of different spatial sampling patterns for sparse array transducer design," *Ultrasonics*, vol. 37, no. 10, pp. 667 – 671, 2000.

[155] C. Holmes, B. Drinkwater, and P. Wilcox, "The post-processing of ultrasonic array data using the total focusing method," *Insight - Non-Destructive Testing and Condition Monitoring*, vol. 46, no. 11, pp. 677 – 680, 2004.

[156] Y.-F. Chang and S.-C. Chen, "Imaging Hilbert-transformed ultrasonic data," *Research in Nondestructive Evaluation*, vol. 13, no. 2, pp. 97 – 103, 2001.

[157] A. Hunter, B. Drinkwater, and P. Wilcox, "The wavenumber algorithm for full-matrix imaging using an ultrasonic array," *IEEE Transactions on Ultrasonics, Ferroelectrics and Frequency Control*, vol. 55, no. 11, pp. 2450 – 2462, november 2008.

[158] J. Lambert, A. Pedron, G. Gens, F. Bimbard, L. Lacassagne, and E. Iakovleva, "Performance evaluation of total focusing method on GPP and GPU," in *Conference on Design and Architectures for Signal and Image Processing (DASIP)*, Oct 2012, pp. 1 – 8.

[159] B. Xu, M. Senesi, and M. Ruzzene, "Frequency-steered acoustic arrays: Application to structural health monitoring of composite plates," *Journal of Engineering Materials and Technology*, vol. 133, no. 1, pp. 011 003–1 – 011 003–6, 2011.

[160] M. Senesi, B. Xu, and M. Ruzzene, "Experimental characterization of periodic frequency-steerable arrays for structural health monitoring," *Smart Materials and Structures*, vol. 19, no. 5, pp. 055 026–1 – 055 026–11, 2010.

[161] M. Senesi and M. Ruzzene, "A frequency selective acoustic transducer for directional Lamb wave sensing," *The Journal of the Acoustical Society of America*, vol. 130, no. 4, pp. 1899 –1907, 2011.

[162] M. Romanoni, S. Gonella, N. Apetre, and M. Ruzzene, "Two-dimensional periodic actuators for frequency-based beam steering," *Smart Materials and Structures*, vol. 18, no. 12, pp. 125 023–1 – 125 023–19, 2009.

[163] P. P. Ewald, "Introduction to the dynamical theory of X-ray diffraction," *Acta Crystallographica Section A*, vol. 25, no. 1, pp. 103 – 108, 1969.

[164] L. V. Azároff, *Elements of X-ray crystallography.* McGraw-Hill, London, 1968.

[165] A. Authier, *Dynamical theory of X-ray diffraction.* Oxford University Press, 2001.

[166] C. Sayers and G. Proudfoot, "Angular dependence of the ultrasonic SH wave velocity in rolled metal sheets," *Journal of the Mechanics and Physics of Solids*, vol. 34, no. 6, pp. 579 – 592, 1986.

[167] D. Allen, R. Langman, and C. Sayers, "Ultrasonic SH wave velocity in textured aluminium plates," *Ultrasonics*, vol. 23, no. 5, pp. 215 – 222, 1985.

[168] E. Baravelli, M. Senesi, M. Ruzzene, and L. De Marchi, "Fabrication and characterization of a wavenumber-spiral frequency-steerable acoustic transducer for source localization in plate structures," *IEEE Transactions on Instrumentation and Measurement*, vol. 62, no. 8, pp. 2197 – 2204, 2013.

[169] D. Duxbury, J. Russell, and M. Lowe, "The effect of variation in phased array element performance for non-destructive evaluation (NDE)," *Ultrasonics*, vol. 53, no. 6, pp. 1065 – 1078, 2013.

[170] S. Ramadas, J. C. Jackson, A. Tweedie, R. O'Leary, and A. Gachagan, "Conformally mapped 2D ultrasonic array structure for NDT imaging application," in *Ultrasonics Symposium (IUS), 2010 IEEE*, 2010, pp. 33 – 36.

[171] M. Abramowitz and I. A. Stegun, *Handbook of mathematical functions, with formulas, graphs and mathematical tables.* Dover Press, 1965.

[172] J. W. Cooley and J. W. Tukey, "An algorithm for the machine calculation of complex Fourier series," *Mathematics of Computation*, vol. 19, pp. 297 – 301, 1965.

[173] A. Ng and J. Swanevelder, "Resolution in ultrasound imaging," *Continuing Education in Anaesthesia, Critical Care & Pain*, vol. 11, no. 5, pp. 186 – 192, 2011.

[174] R. H. Geschke, R. Ferrari, D. Davidson, and P. Meyer, "Application of extended Huygens' principle to scattering discontinuities in waveguide," in *Africon Conference in Africa, 2002. IEEE AFRICON. 6th*, vol. 2, 2002, pp. 555 – 558.

[175] R. L. Ferrari, "An extended Huygens' principle for modelling scattering from general discontinuities within hollow waveguides," *International Journal of Numerical Modelling: Electronic Networks, Devices and Fields*, vol. 14, no. 5, pp. 411 – 422, 2001.

[176] Z. Chen, *The Finite Element Method: Its fundamentals and applications in Engineering*. World Scientific Publishing, 2011.

[177] G. S. Warren and W. R. Scott, "Numerical dispersion in the finite-element method using triangular edge elements," *Microwave and Optical Technology Letters*, vol. 9, no. 6, pp. 315 – 319, 1995.

[178] W. Scott, "Errors due to spatial discretization and numerical precision in the finite-element method," *IEEE Transactions on Antennas and Propagation*, vol. 42, no. 11, pp. 1565 – 1570, 1994.

[179] O. C. Zienkiewicz, *The Finite Element Method: Its Basis and Fundamentals*, 6th ed. Elsevier Butterworth-Heinemann, 2005.

[180] C. Ross, *Finite Element Methods in Structural Mechanics*. Ellis Horwood Limited, 1985.

[181] N. N. Abboud, G. L. Wojcik, D. K. Vaughan, J. Mould, Jr., D. J. Powell, and L. Nikodym, "Finite element modeling for ultrasonic transducers," in *Proc. SPIE Int. Symp. Medical Imaging*, vol. 3341. SPIE, 1998, pp. 19 – 42.

[182] I. S. Sandler, "A new computational procedure for wave propagation problems and a new procedure for non-reflecting boundaries," *Computer Methods in Applied Mechanics and Engineering*, vol. 164, no. 1-2, pp. 223 – 233, 1998.

[183] J.-M. Jin and D. J. Riley, *Finite Element Analysis of Antennas and Arrays*. John Wiley & Sons, 2009.

[184] G. W. C. Kaye, *Tables of physical and chemical constants*. Longman Publishing, 1995.

[185] X. Jian, S. Dixon, R. S. Edwards, and J. Reed, "Coupling mechanism of electromagnetic acoustical transducers for ultrasonic generation," *The Journal of the Acoustical Society of America*, vol. 119, no. 5, pp. 2693 – 2701, 2006.

[186] S. Dixon, S. Burrows, B. Dutton, and Y. Fan, "Detection of cracks in metal sheets using pulsed laser generated ultrasound and EMAT detection," *Ultrasonics*, vol. 51, no. 1, pp. 7 – 16, 2011.

[187] S. Dixon, C. Edwards, and S. B. Palmer, "Texture measurements of metal sheets using wideband electromagnetic acoustic transducers," *Journal of Physics D: Applied Physics*, vol. 35, no. 8, pp. 816 – 824, 2002.

[188] D. Marioli, C. Narduzzi, C. Offelli, D. Petri, E. Sardini, and A. Taroni, "Digital time-of-flight measurement for ultrasonic sensors," *IEEE Transactions on Instrumentation and Measurement*, vol. 41, no. 1, pp. 93 – 97, Feb 1992.

[189] D. Marquardt, "An algorithm for least-squares estimation of nonlinear parameters," *Journal of the Society for Industrial and Applied Mathematics*, vol. 11, no. 2, pp. 431 – 441, 1963.

[190] R. Drai, F. Sellidj, M. Khelil, and A. Benchaala, "Elaboration of some signal processing algorithms in ultrasonic techniques: application to materials NDT," *Ultrasonics*, vol. 38, no. 1 - 8, pp. 503 – 507, 2000.

[191] R. M. White, "Elastic wave scattering at a cylindrical discontinuity in a solid," *The Journal of the Acoustical Society of America*, vol. 30, no. 8, pp. 771 – 785, 1958.

[192] T.-B. Li and M. Ueda, "Sound scattering of a spherical wave incident on a cylinder," *The Journal of the Acoustical Society of America*, vol. 87, no. 5, pp. 1871 – 1879, 1990.

[193] K. Ferrara, V. Algazi, and J. Liu, "The effect of frequency dependent scattering and attenuation on the estimation of blood velocity using ultrasound," *IEEE Transactions on Ultrasonics, Ferroelectrics and Frequency Control*, vol. 39, no. 6, pp. 754 – 767, nov. 1992.

[194] J. Somer, "Electronic sector scanning for ultrasonic diagnosis," *Ultrasonics*, vol. 6, no. 3, pp. 153 – 159, 1968.

[195] L. Cohen, "Time-frequency distributions - A review," *Proceedings of the IEEE*, vol. 77, no. 7, pp. 941 – 981, 1989.

[196] D. Jones and T. Parks, "A resolution comparison of several time-frequency representations," *IEEE Transactions on Signal Processing*, vol. 40, no. 2, pp. 413 – 420, 1992.

[197] M. Niethammer, L. J. Jacobs, J. Qu, and J. Jarzynski, "Time-frequency representations of Lamb waves," *The Journal of the Acoustical Society of America*, vol. 109, no. 5, pp. 1841 – 1847, 2001.

[198] D. E. Newland, *An introduction to random vibrations, spectral and wavelet analysis*. Longman Scientific & Technical, 1993.

[199] S. Hill and S. Dixon, "Localisation of defects with time and frequency measurements using pulsed arrays," *NDT&E International*, vol. 67, pp. 24 – 30, 2014.

[200] J. Ogilvy and I. Culverwell, "Elastic model for simulating ultrasonic inspection of smooth and rough defects," *Ultrasonics*, vol. 29, no. 6, pp. 490 – 496, 1991.

[201] J. Zhang, B. Drinkwater, and P. Wilcox, "Effect of roughness on imaging and sizing rough crack-like defects using ultrasonic arrays," *IEEE Transactions on Ultrasonics, Ferroelectrics and Frequency Control*, vol. 59, no. 5, pp. 939 – 948, 2012.

[202] T. S. Lewis, D. W. Kraft, and N. Hom, "Scattering of elastic waves by a cylindrical cavity in a solid," *Journal of Applied Physics*, vol. 47, no. 5, pp. 1795 – 1798, 1976.

[203] V. K. Varadan, V. V. Varadan, and Y.-H. Pao, "Multiple scattering of elastic waves by cylinders of arbitrary cross section. I. SH waves," *The Journal of the Acoustical Society of America*, vol. 63, no. 5, pp. 1310 – 1319, 1978.

[204] J. C. Aldrin, M. P. Blodgett, E. A. Lindgren, G. J. Steffes, and J. S. Knopp, "Scattering of obliquely incident shear waves from a cylindrical cavity," *The Journal of the Acoustical Society of America*, vol. 129, no. 6, pp. 3661 – 3675, 2011.

[205] I. Daubechies, "The wavelet transform, time-frequency localization and signal analysis," *IEEE Transactions on Information Theory*, vol. 36, no. 5, pp. 961 – 1005, 1990.

[206] B. Boashash, "Estimating and interpreting the instantaneous frequency of a signal. I. Fundamentals," *Proceedings of the IEEE*, vol. 80, no. 4, pp. 520 – 538, 1992.

[207] B. Boashash, *Time frequency signal analysis and processing: A comprehensive reference*. Elsevier, 2003.